COMPUTATIONAL MODELING OF THE TIME-DEPENDENT BEHAVIOR OF CEMENTITIOUS MATERIALS

A Dissertation

by

XIAODAN LI

Submitted to the Office of Graduate and Professional Studies of
Texas A&M University
in partial fulfillment of the requirements for the degree of

DOCTOR OF PHILOSOPHY.

Chair of Committee,	Zachary C. Grasley
Committee Members,	Robert L. Lytton
	Anastasia Muliana
	Patrick Shamberger
Head of Department,	Robin Autenrieth

May 2017

Major Subject: Civil Engineering

ABSTRACT

Finite element procedures combined with microstructure development modeling are integrated to quantitatively predict the viscoelastic/viscoplastic relaxation of cement paste due to intrinsic calcium silicate hydrate viscoelasticity/viscoplasticity and microstructure evolution. The combined models are implemented in a computational routine to predict time-dependent stress and strain fields in cement paste. Besides predicting the time-dependent viscoelastic/viscoplastic properties of cement paste, the early-age desiccation shrinkage of cement paste is also computationally simulated utilizing this modeling approach. The model simulations suggest that inherent viscoelastic deformation caused by calcium silicate hydrate might not necessarily be the primary mechanism leading to the overall early-age time-dependent behavior of cement paste. The effect of time-dependent dissolution of load-bearing phases due to either the hydration reaction or the application of stress/strain can be substantial and should be considered as a significant mechanism for the apparent viscoelasticity/viscoplasticity of cement paste.

DEDICATION

To my parents

ACKNOWLEDGEMENTS

First, I would like to thank my committee chair, Dr. Grasley, and my committee members, Dr. Lytton, Dr. Muliana, and Dr. Shamberger for their guidance throughout the course of this research. Meanwhile, I would like to thank Dr. Bullard, Dr. Garboczi, Dr. Feng and Dr. Rahman for their technical support throughout this research project. This research topic could never be accomplished without their help.

Thanks also go to my friends and colleagues and the department faculty and staff for making my time at Texas A&M University a great experience. I also want to extend my gratitude to the National Science Foundation, which provided the funding support for this research topic.

Finally, thanks to my families, especially my parents, for their encouragement and love.

CONTRIBUTORS AND FUNDING SOURCES

Contributors

This work was supervised by a dissertation committee consisting of Professor Grasley and Professor Lytton of the Zachry Department of Civil Engineering, Professor Muliana of the Department of Mechanical Engineering and Professor Shamberger of the Department of Material Science and Engineering.

All work for this dissertation was completed by the student, under the advisement of Zachary C. Grasley of the Zachry Department of Civil Engineering

Funding sources

This research was supported by the National Science Foundation under grant numbers 0843979, 1327314 and 1463926. Any opinions, findings, and conclusions or recommendations expressed in this material are those of the author and do not necessarily reflect the views of the National Science Foundation.

TABLE OF CONTENTS

Page

LIST OF FIGURES

1. BACKGROUND AND OBJECTIVES

1.1 Motivation and problem statement

Cement paste exhibits viscoelastic/viscoplastic (VE/VP) behavior under mechanical loadings in addition to the instantaneous elastic response, and such time-dependent VE/VP effects have a significant impact on the stress and strain fields inside cementitious materials [1]. Decades of determined research efforts have been dedicated to studying the mechanisms leading to the VE/VP behavior of cementitious materials, yet the primary mechanism is still debatable. As portland cement concrete by far is the most used construction material worldwide because of its many advantages [2], understanding the mechanical properties of cementitious materials, as well as the mechanisms behind these behaviors, is necessary and important for predicting stress and strain in infrastructure.

Currently, three major mechanisms have been proposed as the major sources leading to the VE/VP behavior of cement paste: 1) inherent viscoelasticity/viscoplasticity of the calcium silicate hydrate (C-S-H) phase, 2) dissolution of load bearing phases and 3) poromechanical effects. C-S-H viscoelasticity/viscoplasticity has been historically accepted as dominating the long-term, time-dependent deformation of cement paste. Based on this understanding, many theories towards C-S-H viscoelasticity/viscoplasticity have been proposed, such as the seepage theory [3, 4] and the viscous shear theory [3, 5]. Besides inherent C-S-H VE/VP effects, another major mechanism suggested by researchers is the dissolution of load bearing phases [6, 7], which manifests as a time-dependent redistribution of stress prompted by the dissolution of load bearing solid phases [8, 9], leading to apparent VE/VP effects in cement paste. Poromechanical effects [8, 10-14] are only substantial when the material is fully saturated (at least over time-scales of hours to days or greater). It results in the VE/VP effects of cement paste in a similar way as the mechanism of dissolution of loading bearing phases, where stresses gradually transfer from the pore fluid phase to the solid skeleton inside saturated cementitious materials [15-17]. In this project, because all the cement paste specimens are analyzed under partially saturated condition, the main VE/VP mechanisms focused in the dissertation are the intrinsic VE/VP properties of C-S-H and the time-dependent dissolution of solid load bearing phases.

To experimentally determine the VE/VP relaxation moduli of cement paste is challenging. First, creep or relaxation tests can last months or even years, which involves enormous cost, as well as time. Second, some of mechanical properties of cement paste are extremely difficult to measure, e.g., the VE/VP Poisson's ratio. Generally, due to experimental difficulties in accurately measuring relatively small displacements normal to the loaded direction [18], Poisson's ratio is agreed to be the most difficult of the elastic constants to experimentally determine [19]. For example, in a normal weight concrete cylinder with a 150 mm (6 in.) diameter, under a 1D longitudinal compressive failure strain of 0.003, the radial displacement for the specimen would be of order 10^{-2} mm, leading to significant measurement difficulties. The challenges of measuring the time-dependent VE/VP Poisson's ratio of cement paste [20, 21] are further compounded in creep or relaxation tests which lasts for long periods. Third, as the relaxation/creep of cement paste can occur under the effects of multiple mechanisms, it is impossible to experimentally evaluate each single mechanism separately because these mechanisms occur simultaneously over the same time scale. These measurement challenges motivate the development of computational methods to complement experimental measurements in investigating cement paste VE/VP properties.

To theoretically predict the VE/VP relaxation moduli of cement paste, one should overcome many difficulties. In addition to its complex, random, composite matrix arrangement at the micrometer scale, the microstructure evolution of cement paste during the hydration process is an additional important complexity, as its response to load critically depends on loading histories relative to the time the new components are formed. Previously, a model implementing the finite element method (FEM) was used to successfully predict the elastic properties of cement paste based on the elastic properties of the microscopic phases and their evolving spatial structure [22]. In combination with a microstructure evolution model, a next generation finite element model can be developed to give predictions of the VE/VP properties of cement paste using similar computational methods [8, 23].

With the completion of the development of this viscoelasticity/viscoplasticity prediction model, this model can be applied to broader applications besides the prediction of the time-dependent behavior of cement pastes. Many natural and man-made materials are multiphasic composite materials, such as polymers, alloys, porous media, etc., and most of these materials also exhibit notable time-dependent VE/VP behavior under long-term external mechanical loading. Currently, many computational algorithms and numerical simulation techniques have been developed attempting to study the creep/relaxation behavior of composite materials, such as mesoscale finite element simulations of concrete [24], micromechanical modeling approaches of polymers [25], constitutive derivations of nanocomposite melts [26], etc. Research has also been conducted to study the mechanisms behind the VE/VP behavior of these materials, and it has been proposed that dissolution of load-bearing phases occurring during the microstructure evolution also plays an important role in inducing time-dependent deformation behavior of the macroscopic materials. Utilizing the newly developed computational model in this project, with the input of different time-evolving microstructures, the dissolution-induced creep/relaxation of these composite materials could also be studied and analyzed.

1.2 Objectives

The major objective of this research is to develop a computationally implemented model to predict the evolution of VE/VP properties of cement paste based on the aforementioned mechanisms. To achieve this major target, a holistic kinematic framework linking the microstructure evolution to the evolution of stress and strain fields has to be established first to better understand the evolution of composite constitutive properties and deformation mechanisms. The evolution of different VE/VP mechanical properties of cement paste, including VE/VP Young's modulus, Poisson's ratio, Bulk modulus and Shear modulus, will be predicted utilizing the computational scheme. The second objective is to evaluate the contribution of each aforementioned mechanism towards the overall VE/VP behavior of cementitious materials. Virtual experiments were carried out on cement paste specimens under different circumstances as well as under the separate or combined effects of different mechanisms. The predicted results from different virtual experiments will be analyzed and compared with each other. The last objective of this project is to demonstrate the utility and robustness of the modeling approach via prediction of the shrinkage behavior of hydrating cement paste under drying conditions, such that the broad utility of the computationally implemented model can be demonstrated.

1.3 Disposition

This report consists of eight chapters. Chapter 2 introduces the theoretical conceptualization, as well as the logic flow of the computational scheme. A kinematic framework is established to quantify the effect of dissolution of load-bearing phases on the overall stress and strain fields in evolving composite materials. Meanwhile, simple validation of the model is ensured in this chapter though comparing the simulation results from this newly developed model with the simulation results from other commercial softwares. Chapter 3 evaluates the role of the mechanism of C-S-H viscoelasticity/viscoplasticity as well as C-S-H aging towards the overall relaxation/creep behavior of cement paste. In comparison, Chapter 4 evaluates the mechanism of cement grain dissolution during the early age hydration reaction towards the overall VE/VP behavior of cement paste. Combining the effects of both mechanisms introduced in Chapter 3 and Chapter 4, Chapter 5 focuses on the calculation and discussion of the apparent VE/VP Poisson’s ratio of cement paste, which is the most difficult mechanical property to experimentally measure, and Chapter 6 extends the utility of the computational scheme to simulate the shrinkage behavior of early age cement paste. New insights are developed in Chapter 6 to explain the mechanisms behind the irreversibility of desiccation shrinkage. Based on the discussions included in Chapter 4, Chapter 7 further extends the importance of dissolution of solid constituents in leading to VE/VP behavior of cement paste by introducing the mechanism of stress-induced dissolution of hydrates. The computational scheme is further modified in this chapter to account for the stress-induced dissolution effect. Chapter 8 summarizes the whole manuscript and proposes future work. References are listed at the end of the document.

2. COMPUTATIONALLY IMPLEMENTED MODEL*

The computational scheme integrates two different models: a time-evolving microstructure model and a finite element based mechanical model. The microstructure models generate time-evolving microstructures for different composite materials, which are then utilized in the finite element calculation model to predict the time-evolving creep/relaxation responses of these composites. In this chapter, the conceptualization of the microstructure model as well as the microstructure-based finite element calculation model is first introduced. A kinematical framework is also established in this chapter to quantify the dissolution process of solid phases inside material composites. Based on the thorough understanding of the microstructure evolution process inside cementitious materials, a microstructure evolution model of cement paste and the finite element calculation routine is computationally implemented into a computer program utilizing the programming language C++.

2.1 Conceptualization and kinematic framework

To account for the time dependence (as well as the strain and stress history dependence) of the elastic and viscoelastic properties, the computational scheme is discretized in time. At each time step in the computational scheme, the microstructure models provide a 3D snapshot of the composite materials for the corresponding age of

---

* Reprinted with permission from "Computationally implemented modeling of creep of composite materials caused by phase dissolution" by X. Li, S. Rahman and Z. C. Grasley, 2016. Computational materials science, 125, 61-71. 2017 by Elsevier. And reprinted with permission from "Modeling the apparent and intrinsic viscoelastic relaxation of hydrating cement paste" by X. Li, Z.C. Grasley, E.J. Garboczi and J.W. Bullard, 2015. Cement and concrete composites, 55, 322-330. 2017 by Elsevier.

the time step. All the 3D snapshots of the materials are meshed into voxels utilizing a spatially aligned numerical discretization [27]. Thus, each voxel is an eight node cubic finite element comprised of a single homogenous material. Therefore, in the computational-implemented model, the evolution of the microstructure with time occurs at the scale of the voxels. Then, finite element calculations are carried out on these meshed 3D time-evolving microstructures to predict the time-evolving mechanical responses of these composites under periodic strain-controlled boundary conditions. The evolving mechanical properties are subsequently calculated via the spatially averaged stress and strain fields. At each time step, phase change may occur in any of the voxels as prescribed by the evolution of the microstructure from one time step to the next– including both solid, load-bearing phases and phases that may not transmit stress (e.g., gases). Regarding conservation of linear momentum, it is assumed that once phase change occurs in one voxel, the stress being transmitted by this voxel would be transferred into surrounding voxels. Meanwhile, the newly formed phase in this voxel is assumed to be infinitely compliant such that it would not carry any stress at the time of formation, but meanwhile its configuration conforms to the preexisting deformed voxel, neglecting all the memories of historical responses. This procedure supposes that the process of stress redistribution takes much less time than microstructure evolution itself. This time-dependent stress redistribution is elaborated conceptually in Figure 1 under a stress-controlled boundary condition.

The concept of evolving natural configurations [28-30] can be utilized to develop a consistent kinematical framework to quantify the effect of dissolution of load bearing phases on the equilibrium state of composite materials. When a material is subjected to an external stimuli (or multiple stimuli) such as an external traction, temperature change, or moisture change, the material body will deform from the reference configuration to the current configuration. If the external stimuli are removed from the

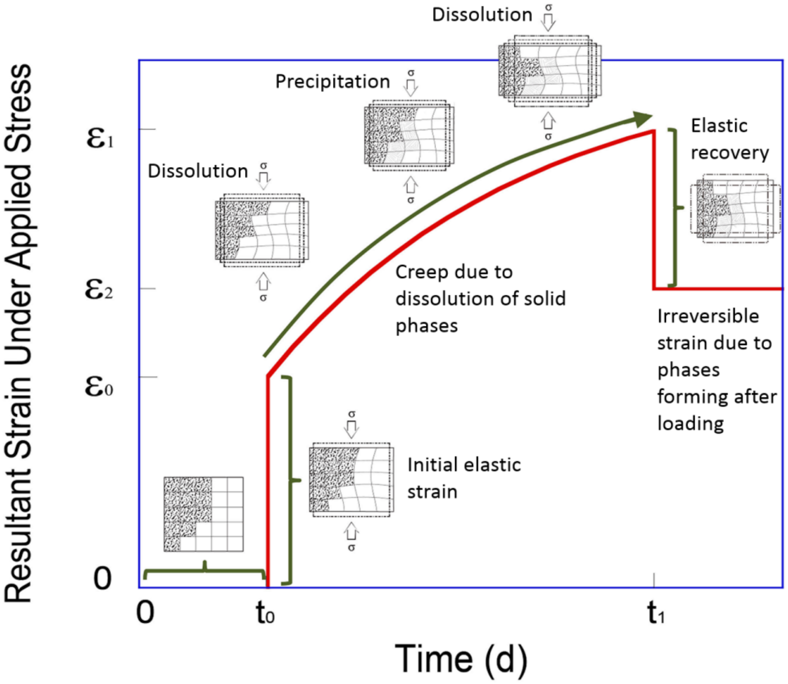

Figure 1 *Conceptual diagram of the computational scheme. The creep behavior of an evolving microstructure is shown in the figure, with* σ *denoting a controlled external macroscale load. (a) Initially, load-bearing phases exist inside the composite before load is applied. (b) When an external load is applied at time* t_0*, the body deforms elastically immediately. (c) As load-bearing phases dissolve in certain voxels, the stress transmitted by the surrounding solid voxels increases, increasing the deformation in these surrounding voxels, leading to an increase in the macroscopic deformation of the whole composite. Since the rate of stress transfer depends on dissolution rate, this results in creep. (d) New phases form with their configurations conforming to the deformed voxels while carrying no stress. (e)This process repeats as more material dissolves and the whole composite deforms again. (f) When the external load is removed at time* t_1*, the body deforms again, but it will not recover back to its initial configuration, leaving a permanent irreversible strain.*

material body, it will deform back to its natural configuration; for the simplest, purely elastic bodies, the natural configuration may coincide with the reference configuration. In the case of the material with dissolving solids, as dissolution processes progress, under any external or internal stimuli (e.g. applied tractions/displacements), the composite body – as well as every voxel comprising the composite – deform from the initial, reference configuration to the current configuration. As the dissolution-formation process occurs over the same time scale as the motion, with the removal of external stimuli the composite will *not* return back to the reference configuration, but rather to the composite natural configuration, which may evolve with time. It has been demonstrated that the evolution of natural configurations could lead to creep in purely elastic bodies [31], and this is the basis of the hypothesized expectation that dissolution effects would lead to creep of composites. The same evolution of configurations that happens with the composite as a whole can be presumed to likewise occur with any voxel. Since the natural configuration for the composite can be different from the natural configuration for any given voxel at a given time[1], this difference in motion yields "apparent strain" in the composite natural configuration, as shown in Figure 2.

Figure 2 shows the overview of the kinematical framework of the dissolution-formation process utilizing the concept of time-evolving natural configurations. Note that conceptually, this framework is analogous to that utilized in the analysis of mixtures or other materials with multiple natural configurations [32-38]. In Figure 2, the

---

[1] The natural configuration of an individual voxel should be interpreted as the configuration that voxel would return to if any stimuli applied to that individual voxel were removed (e.g., if applied stress were removed from the voxel).

framework at each step corresponds to one time step shown in Figure 1. The motions χ_{κ} show the paths of a material point between different configurations. The motions χ_{κ_p} and $\chi_{\kappa_{p(t)}}$ denote the path of a point in the composite body from the initial, reference configuration to the natural configuration of the composite, and then to the current configuration. The motions $\chi_{\kappa_p^v}$ and $\chi_{\kappa_{p(t)}^v}$ denote the motion of a given voxel (occupying the same location in the composite as the point referred to above) from the initial reference configuration to the natural configuration, and then to the current configuration. In Figure 2(a), all the motions (both the composite and voxel) start from the initial reference configuration. At $t = t_1$, as shown in Figure 2(b), external or internal stimuli are applied on the material, deforming the composite body from the reference configuration to the current configuration, and removal of the stimuli will not necessarily make the composite return back to the initial reference configuration. If the inherent phases that comprise the composite are VE/VP themselves, the natural configuration of the whole composite may evolve with time, and with the removal of the stimuli, the body will return to the evolved natural configuration instead of the reference configuration; likewise for the individual voxels inside the microstructure. Once phase dissolution occurs in a voxel at $t = t_2$, as shown in Figure 2(c), any stress carried by this voxel is forced to be zero and the current configuration becomes the voxel's new natural configuration. At this time, before the formation of new phases, the natural configuration of the composite stays the same as the configuration shown in Figure 2(b),

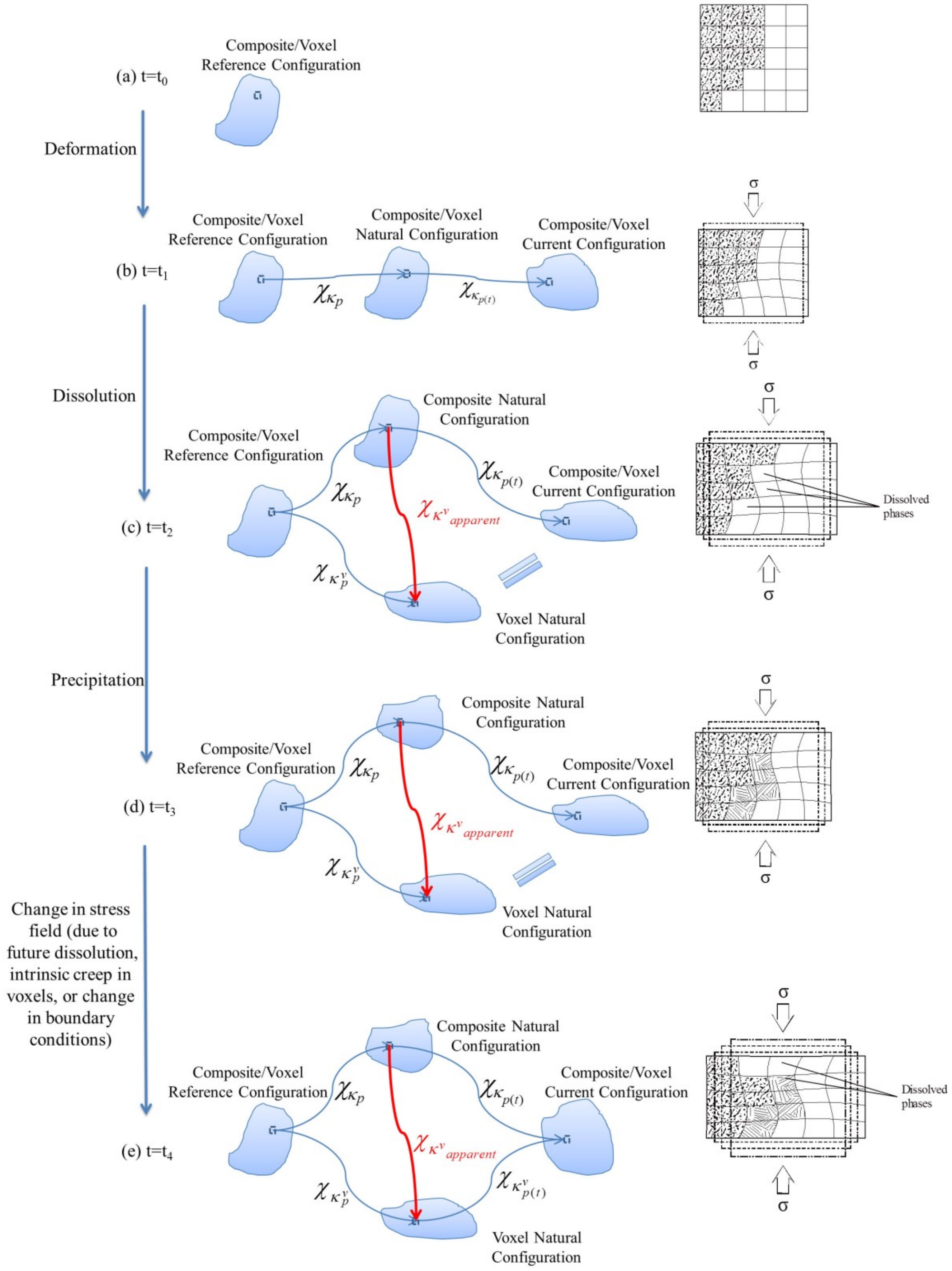

Figure 2 *Overview of the kinematical framework of the dissolution-formation process.*

leading to a difference between the composite natural configuration and the voxel natural configuration. This difference in deformation is a mapping $\chi_{\kappa^{v}_{apparent}}$ that leads to "apparent strain" in the composite body. From the perspective of continuum mechanics, apparent strain is defined here as the strain that exists independent of any applied stimuli (the state of stress specifically in this project). At $t = t_3$ in Figure 2(d), the natural configuration of the composite changes again with the formation or precipitation of new solid phases. At the last time step in Figure 2(e), with any future change in the stress field within the composite (which may occur due to further dissolution, intrinsic creep in the voxels, and/or change in boundary conditions), voxels filled with newly formed phases deform from the individual voxel natural configuration to the new current configuration; likewise, the whole composite body deforms to the new current configuration.

From Figure 2, it can be seen that the existence of apparent strain is a key reason behind the dissolution-induced VE/VP behavior and the irreversible nature of much of the dissolution induced creep. To computationally predict the overall deformation behavior of the composite material, the effect of apparent strain on the inherent stress and strain fields inside the composite must be quantified. Figure 3 shows a more complete version of the framework demonstrated in Figure 2 (e), and in this figure, the motion of a material point inside continuous body is defined as

$$\mathbf{x} = \chi_{\kappa}(\mathbf{X}, t), \tag{1}$$

where $\mathbf{x}$ is the position vector in the current configuration of the motion, $\mathbf{X}$ is the position vector in the reference configuration of the motion, and the boldface indicates a vector (or, in general, a higher order tensor). The deformation gradient of the body is defined according to

$$\mathbf{F} = \frac{\partial \mathbf{x}}{\partial \mathbf{X}}. \tag{2}$$

As stated previously, a primary goal here is to quantify the stress relaxation or creep that occurs due to phase dissolution in a composite microstructure. Such stress relaxation or creep is determined by quantifying the time evolution of the spatially averaged strain field and the spatially averaged stress field under a particular boundary condition. For a composite material body input into the computational scheme, spatially averaged strain is calculated according to the deformation from the reference configuration to the current configuration (i.e., motion χ_{κ}). The spatially averaged stress field is calculated according to the difference between the composite natural configuration and the composite current configuration, which is mapped through the motion $\chi_{\kappa_{p(t)}}$. Unfortunately, when stress relaxation or creep is induced by dissolution

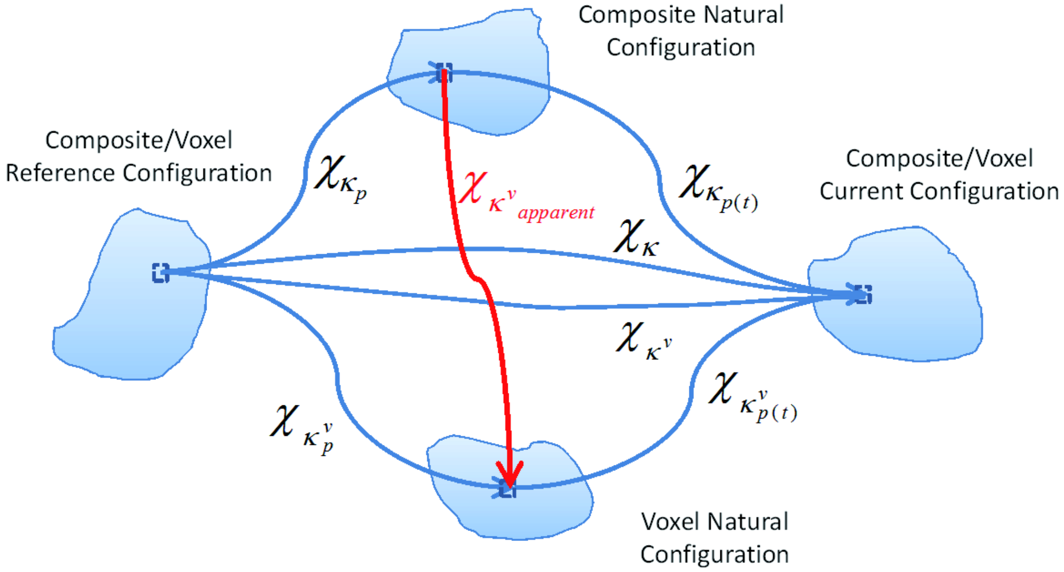

Figure 3 *A complete view of the kinematic framework shown in Figure 2(e)***.**

of load-bearing phases, one cannot directly determine the deformation gradient (and thus the strain and stress) associated with the motion $\chi_{\kappa_{p(t)}}$. However, the motion $\chi_{\kappa_{p(t)}}$ can be decomposed into two different computable motions: one from the composite natural configuration to the voxel natural configuration $\chi_{\kappa^v_{apparent}}$, and one from the voxel natural configuration to the current configuration $\chi_{\kappa^v_{p(t)}}$. For these three motions, according to eq. (2), the deformation gradients are

$$\text{motion } \chi_{\kappa_{p(t)}} : \mathbf{F}_{\kappa_{p(t)}} = \frac{\partial \mathbf{x}_{\kappa}}{\partial \mathbf{x}_{\kappa_p}}$$

$$\text{motion } \chi_{\kappa^v_{apparent}} : \mathbf{F}_{\kappa^v_{apparent}} = \frac{\partial \mathbf{x}_{\kappa^v_p}}{\partial \mathbf{x}_{\kappa_p}} \quad , \tag{3}$$

$$\text{motion } \chi_{\kappa^v_{p(t)}} : \mathbf{F}_{\kappa^v_{p(t)}} = \frac{\partial \mathbf{x}_{\kappa^v}}{\partial \mathbf{x}_{\kappa^v_p}} = \frac{\partial \mathbf{x}_{\kappa}}{\partial \mathbf{x}_{\kappa^v_p}}$$

where $\mathbf{x}_{\kappa}$ and $\mathbf{x}_{\kappa^v}$ are the position vectors of a point in the composite body and the corresponding voxel in the current configuration, $\mathbf{x}_{\kappa^v_p}$ is the position vector of the voxel in the voxel natural configuration, and $\mathbf{x}_{\kappa_p}$ is the position vector of the point corresponding to the location of the voxel in the composite natural configuration. From eq. (3), one can derive that

$$\mathbf{F}_{\kappa_{p(t)}} = \mathbf{F}_{\kappa^v_{apparent}} \mathbf{F}_{\kappa^v_{p(t)}} \,. \tag{4}$$

Combining eq. (4) with the Green-Lagrangian strain expression

$$\mathbf{E} = \frac{1}{2}(\mathbf{F}^T \mathbf{F} - \mathbf{I}) \,, \tag{5}$$

where $\mathbf{I}$ is the identity tensor, one finds that for the motion $\chi_{\kappa_{p(t)}}$,

$$\mathbf{E}_{\kappa_{p(t)}} = \frac{1}{2}((\mathbf{F}_{\kappa^v_{apparent}} \mathbf{F}_{\kappa^v_{p(t)}})^T (\mathbf{F}_{\kappa^v_{apparent}} \mathbf{F}_{\kappa^v_{p(t)}}) - \mathbf{I}) = \frac{1}{2}(\mathbf{F}_{\kappa^v_{p(t)}}{}^T \mathbf{F}_{\kappa^v_{apparent}}{}^T \mathbf{F}_{\kappa^v_{apparent}} \mathbf{F}_{\kappa^v_{p(t)}} - \mathbf{I}) \,, \tag{6}$$

where $\mathbf{E}_{\kappa_{p(t)}}$ is the strain tensor of a particular point in the composite body generated during the motion $\chi_{\kappa_{p(t)}}$ from the composite natural configuration to the current configuration. Similarly, according to eq. (5), for motion $\chi_{\kappa^v_{apparent}}$ and $\chi_{\kappa^v_{p(t)}}$,

$$\mathbf{E}_{\kappa^v_{apparent}} = \frac{1}{2}(\mathbf{F}_{\kappa^v_{apparent}}{}^T \mathbf{F}_{\kappa^v_{apparent}} - \mathbf{I}) \text{ and } \mathbf{E}_{\kappa^v_{p(t)}} = \frac{1}{2}(\mathbf{F}_{\kappa^v_{p(t)}}{}^T \mathbf{F}_{\kappa^v_{p(t)}} - \mathbf{I}), \tag{7}$$

where $\mathbf{E}_{\kappa^v_{apparent}}$ is the strain tensor for the voxel that exists at the same, particular point in the composite, generated during the motion $\chi_{\kappa^v_{apparent}}$, and $\mathbf{E}_{\kappa^v_{p(t)}}$ is the strain tensor of the particular voxel generated during the motion $\chi_{\kappa_{p(t)}}$.

Combining (6) and (7) results in

$$\mathbf{E}_{\kappa_{p(t)}} = \mathbf{F}_{\kappa^v_{p(t)}}{}^T \mathbf{E}_{\kappa^v_{apparent}} \mathbf{F}_{\kappa^v_{p(t)}} + \mathbf{E}_{\kappa^v_{p(t)}} . \tag{8}$$

We now recognize that the displacement

$$\mathbf{u}_{\kappa^v_p} = \mathbf{x}_\kappa - \mathbf{x}_{\kappa^v_p} \tag{9}$$

is the displacement of a given voxel from the natural configuration of the voxel to the current configuration. Since

$$\mathbf{F}_{\kappa^v_{p(t)}} = \frac{\partial \mathbf{x}_\kappa}{\partial \mathbf{x}_{\kappa^v_p}} = \mathrm{Grad}_{\kappa^v_p} \mathbf{u}_{\kappa^v_p} + \mathbf{I} , \tag{10}$$

where one should carefully note that $\mathrm{Grad}_{\kappa^v_p}$ is the gradient operation in reference to the position in the voxel natural configuration, we find that (8) becomes

$$\mathbf{E}_{\kappa_{p(t)}} = \left(\mathrm{Grad}_{\kappa^v_p} \mathbf{u}^T_{\kappa^v_p} + \mathbf{I} \right) \mathbf{E}_{\kappa^v_{apparent}} \left(\mathrm{Grad}_{\kappa^v_p} \mathbf{u}_{\kappa^v_p} + \mathbf{I} \right) + \mathbf{E}_{\kappa^v_{p(t)}} . \tag{11}$$

If the strains are small in magnitude (as in the simulations considered in this work), then (11) becomes

$$\boldsymbol{\varepsilon}_{\kappa_{p(t)}} = \boldsymbol{\varepsilon}_{\kappa^v_{apparent}} + \boldsymbol{\varepsilon}_{\kappa^v_{p(t)}} \tag{12}$$

where $\boldsymbol{\varepsilon}$ is the infinitesimal, linearized strain. eq. (12) may also be written as

$$\boldsymbol{\varepsilon} = \boldsymbol{\varepsilon}_{apparent} + \boldsymbol{\varepsilon}_{mechanical} , \tag{13}$$

where $\boldsymbol{\varepsilon}_{apparent}$ is the apparent strain of a particular voxel generated during the dissolution-formation process (and associated with the mapping of a point from the composite natural configuration to the corresponding voxel natural configuration), and $\boldsymbol{\varepsilon}_{mechanical}$ is the mechanical strain of the voxel as a result of the stress state within that voxel. Note that the specific requirement for the use of the linearized strain here is that the individual voxel strain between the natural and current configurations must be small along with the product of that strain and the apparent strain that occurs between the composite body as a whole and the individual voxels. It is important to be aware that one might have a composite exhibiting small strain at the macroscopic length scale while yet exhibiting locally large strains at the voxel level (depending on choice of length scale for the voxel); in such a case, the linearization in (12) is inappropriate.

From eq. (13), it can be seen that, from a book-keeping perspective, apparent strain can be treated in the same fashion as free strains or eigenstrains [39], except that the apparent strain does not involve a change in the atomic or molecular spacing from the reference configuration, but a change from the natural configuration of the composite body to the natural configuration of a specific voxel. Other free strains that are induced by temperature change or internal relative humidity change are produced as a result of the configuration change from the reference configuration to the natural configuration of the composite. In the computational scheme, when calculating the stress in a particular voxel, only the mechanical strain is involved in the calculation while the stress associated with the apparent strain is strictly zero.

To implement the above conceptualization and kinematic framework of the dissolution process into the computational scheme, the phases inside each voxel at all time steps should be tracked and all the voxels that participate in the dissolution process should be recorded. In the model, under the applied periodic boundary condition over the entire time scale, different microstructures of composites are input into the scheme. Microstructures from two neighboring time steps would be compared first at the beginning of each time step, so that once the phases in one single voxel changes between the two time steps, the location and the configuration of this voxel would be noted for further calculation, while its historical mechanical responses would be expunged. The newly formed phases would be assigned with new constitutive properties for the subsequent time steps. Finite element analysis is carried out on the new microstructure to calculate the new internal stress and strain fields inside the material, and this procedure repeats for all time steps. Apparent VE/VP relaxation moduli are determined by quantifying the volume averaged stress at each time step (recall that the volume averaged strain is fixed as zero to simulate a relaxation experiment).

2.2 Computational implementation

2.2.1 Microstructural modeling

The previously referenced prediction of cement paste elastic moduli involved utilizing the microstructure model CEMHYD3D (CEMent HYDration in 3D) [40], which generated lattice-based 3D digital microstructure images of specific cement pastes at specific degrees of hydration. Each voxel in the 3D microstructure was treated as an eight-node tri-linear cubic element in a finite element solver at the micrometer scale. By assigning individual phase elastic moduli to each voxel (depending on which individual phase occupied each voxel) and applying periodic displacement boundary conditions, the finite element program predicted the full 3D stress and strain fields [22, 41, 42]. These fields were spatially averaged over the microstructure to determine the composite elastic moduli at a given degree of hydration and then compared to experiments where both elastic moduli and degree of hydration were measured [43].

In the computational approach undertaken in this research, a next-generation hydration model called THAMES (Thermodynamic Hydration And Microstructure Evolution) [44, 45] was utilized to simulate the microstructure evolution during the hydration process at the micrometer level. THAMES is capable of producing 3D snapshots of hydrating cement paste microstructure at different ages based in part on thermodynamic equilibrium calculations and phenomenological dissolution kinetics [44]. The input provided to THAMES was the phase makeup (mass fractions of constituents) of the cement considered at the particle level, the particle size distribution of the cement, and the water to cement ratio (*w/c*). THAMES randomly placed the digital cement grains within a specified domain, and the grains began to dissolve at the surface according to phenomenological dissolution kinetics functions. At each time step, the pore fluid speciation from the previous time step was combined with the change in speciation induced from dissolution since the previous step. Based on the new speciation at the present time step, the thermodynamic engine GEMS (Gibbs Energy Minimization) [46, 47] was utilized to find the equilibrium solution speciation and the mass of each solid constituent in equilibrium with the solution. It was assumed that near-equilibrium conditions were present between the hydration products and pore solution, which is a reasonable approximation after about 12-24 hrs of hydration for typical portland cement pastes. The new hydration products formed at a particular time step were spatially located based on local geometric information regarding interfaces. This information included restrictions on where a particular constituent can grow and empirical information regarding the growth habit of the constituent (i.e. random, acicular, isotropic). The output from THAMES at each time step is a representative microstructure of constituents, in which each cubic voxel consists of a single phase. One thing to note here is that, when cement composites are subjected to external or internal stresses/strains, large local stresses/strains can be generated inside cement pastes. According to the second law of thermodynamics, these stresses/strains can potentially change the microstructure evolution of cement composites. At current stage, the microstructure model THAMES can predict the microstructure evolution of cement paste during hydration process, it is not capable of accounting for the microstructure change that occurs due to applied stress/strain. THAMES will be modified later in the dissertation to account for this stress-induced microstructure evolution effect. But unless stated clearly, for the simulation results generated in this first part of this dissertation, it only considers the relaxation/creep behavior of cement composites as a result of cement grain dissolution during the hydration process, while the stress-induced microstructure change inside cement paste was disregarded.

2.2.2 Finite element calculation

Finite element procedures were rewritten in C++, based on the existing Fortran codes [41, 42], to match THAMES, since it is also written in C++. The finite element codes were combined with the THAMES microstructure model to develop an elastic moduli prediction model as well as a VE/VP relaxation moduli prediction model. In each case, the THAMES microstructure was meshed using a spatially aligned numerical discretization [48] such that each voxel (consisting of a unique phase) became an eight node tri-linear cubic finite element. In the elastic properties prediction model, each voxel was assigned isotropic elastic moduli. For anisotropic crystalline phases, the effective average isotropic moduli were calculated as the arithmetic average of the Voigt and Reuss polycrystalline bounds [49]. This procedure was deemed an accurate approximation owing to the probable random orientation of these phases within a given microstructure. The microstructure was subjected to strain-controlled periodic displacement boundary conditions and the total mechanical energy stored inside the whole microstructure was minimized to solve the boundary value problem [22, 42]. The composite elastic moduli were calculated by solving the elastic equations on a regular finite element mesh [43], based on the volume averaged stress of the composite under the specific boundary condition. A similar approach has yielded elastic moduli that agree well with the experimental results obtained from general porous materials and also cement paste specimens fabricated using the same cement and *w/c* considered in the simulations [22, 50].

To predict the time-dependent VE/VP behavior of cement paste, the elastic microstructure model was discretized in time to account for the time and (stress or strain) history dependent mechanical properties. At each time step in the finite element calculations, the microstructure model THAMES provided a snapshot of the 3D time-evolving microstructure, and similarly to the elastic moduli prediction model, the VE/VP finite element model solved the strain-controlled viscoelastic problem by minimizing the total energy stored in the microstructure at each time step.[2]

If one phase is viscoelastic, the virtual work principle was used with the viscoelastic model to calculate the mechanical energy of the viscoelastic phases inside the microstructure [51, 52]. In the domain Ω of the problem, the virtual work expression for stored viscoelastic energy is derived under a virtual stress boundary condition induced by the traction condition

$$t_i = \sigma_{ji} n_j \tag{14}$$

for all points lying on a part of the boundary denoted as S_2, where σ_{ij} are components of the Cauchy stress tensor and n_j are components of the unit normal vector [53, 54]. A variational form of virtual work for infinitesimal deformations is

$$\int_{\Omega} \delta u_i b_i d\Omega + \int_{S_2} \delta u_i t_i d\Omega - \int_{\Omega} \delta u_i \rho \ddot{u}_i d\Omega - \int_{\Omega} \delta \varepsilon_{ij} \sigma_{ij} d\Omega = 0 \,, \tag{15}$$

where ρ is mass density, b_i are body force components, u_i are displacement components, ε_{ij} are infinitesimal strain components, δ denotes an infinitesimal variation, and the overhead dots denote partial differentiation with respect to time [52]. Under a quasi-static state with a negligible inertia, the terms containing velocity components in eq. (15) can be eliminated and the instantaneous stored energy in viscoelastic phases can be approximated as

---

[2] This solution procedure for the VE/VP material problem disregards any linear momentum in the body. This approach generates negligible error since the velocity of the time-dependent deformation is extremely slow under the boundary conditions considered.

$$\psi = \frac{1}{2}\int_{\Omega} \varepsilon_{ij} C_{ijkl} \varepsilon_{kl} d\Omega + \int_{\Omega} u_i b_i d\Omega \, , \tag{16}$$

where ψ is the energy stored in viscoelastic phases and C_{ijkl} are components of instantaneous elastic moduli. For elastic phases, when the composite is subject to infinitesimal strains, the total elastic mechanical energy stored in one single voxel can be calculated by

$$En = \frac{1}{2}\int_0^1\int_0^1\int_0^1 \varepsilon_{pq} C_{pqrs} \varepsilon_{rs} dx\, dy\, dz, \tag{17}$$

where En is the total stored mechanical energy, ε_{pq} is the infinitesimal strain tensor; *p, q, r, s* = 1, 2, or 3, and the integral is over the volume of a single unit voxel. By expressing the strain tensor in terms of displacement components, eq. (17) can be rewritten as

$$En = \frac{1}{2} u_{rp}^{T} D_{rpsq} u_{sq} , \tag{18}$$

where D_{rpsq} is the stiffness matrix and u_{rp} is the *p*'th component of displacement at *r*'th node.

From eq. (13), the strain tensors for any voxel in the microstructure can be approximated as the sum of the mechanical strain and the apparent strain, and so may the displacement vector of the nodes,

$$u_{rp} = U_{rp} + \delta_{rp} + \delta_{rp}^{apparent} \tag{19}$$

where U_{rp} is the displacement vector determined by the surrounding voxels, δ_{rp} is the correction vector determined by periodic boundary conditions, and $\delta_{rp}^{apparent}$ is the correction vector determined by the apparent strain produced in the microstructure during the dissolution process. Defining $\delta_{rp}^{combined} = \delta_{rp} + \delta_{rp}^{apparent}$, eq. (18) becomes

$$En = \frac{1}{2}\left[u_{rp}^{T} D_{rp,sq} u_{sq} + 2\delta_{rp}^{combined} D_{rp,sq} u_{sq} + \delta_{rp}^{combined} D_{rp,sq} \delta_{sq}^{combined}\right] \tag{20}$$

where $\delta_{rp}^{combined}$ is the total correction vector for the displacement of a node. eq. (20) can be simplified as

$$En = \frac{1}{2}\mathbf{uAu} + \mathbf{bu} + C, \tag{21}$$

where $\mathbf{A}$ is the Hessian matrix comprised of the stiffness matrices, $\mathbf{u}$ is a vector of all the displacements, $\mathbf{b}$ is a global vector, and C is a global constant; $\mathbf{b}$ and C are determined by both the external strain controlled, periodic boundary conditions, and the dissolution and precipitation process of phases that occurs in voxels, which generates apparent strain. Since in eq. (21) there is no term with an order higher than quadratic, to derive the exact displacement solution leading to the minimum energy, Simpson's rule may be used such that

$$\frac{\partial En}{\partial \mathbf{u}} = \mathbf{Au} + \mathbf{b} = 0. \tag{22}$$

Through minimizing the total mechanical energy stored in the microstructures, stress and strain fields of these microstructures at each time step can be predicted through FEM. While cementitious materials are rarely subjected to large deformation gradients on the macroscopic length scale – owing to their quasi-brittle nature – it is possible that locally large deformation gradients might still occur in the microstructure. While infinitesimal strains are considered in the analysis discussed herein, further study is needed to determine the likelihood of finite strains in the microstructure.

Prescribed, periodic volumetric strain and prescribed, periodic shear strain were applied on the boundaries of a series of microstructures at different ages to determine the evolutions of cement paste VE/VP bulk modulus and VE/VP shear modulus. To predict the time-evolving strain of the macroscopic composite under constant external stress, Boltzmann's superposition principle [55, 56] was used to simulate the constant, stress-controlled periodic boundary conditions. First, the spatially averaged hydrostatic stress of the composite under constant unit periodic volumetric strain may be calculated as a function of time for different loading ages as stress relaxes with time. In order to maintain an overall spatially averaged constant stress state, a necessary amount of extra strain must be applied on the composite at each time step. This additional strain may be calculated according to the superposition principle via

$$\begin{aligned}
&\text{if } i = 1,\ \varepsilon(t_i) = \frac{-\sigma_0}{3K_{t_i}(t_i)};\\
&\text{if } i \neq 1,\ \varepsilon(t_i) = \frac{\sigma_0 - \sum_{k=1}^{i-1}[\varepsilon(t_k)K_{t_k}(t_i)]}{3K_{t_i}(t_i)},
\end{aligned} \tag{23}$$

where σ_0 is the maintained constant boundary stress, $\varepsilon(t_i)$ is the additional linear strain to be applied on the composite at time t_i to achieve the desired boundary stress history, and $K_{t_k}(t_i)$ is the apparent VE/VP bulk modulus of the composite at time t_i when loaded at age t_k. The resultant strain history of the composite (e.g., the sum of the creep and elastic strains) is calculated through

$$\varepsilon_{total}(t_i) = \sum_{k=1}^{i} \varepsilon(t_k) \tag{24}$$

where $\varepsilon_{total}(t_i)$ is the strain of the composite at time t_i. The preceding application of Boltzmann's superposition principle was utilized in similar fashion (but with a constant applied, boundary deviatoric stress) to determine the time-dependent shear strain. The expressions were subjected to Laplace transformations to determine the VE/VP Young's modulus and Poisson's ratio from the VE/VP bulk and shear moduli. The resultant VE/VP Young's modulus and VE/VP Poisson's ratio of isotropic cement paste were subsequently calculated via [57, 58]

$$s\bar{E} = \frac{9s\bar{K}s\bar{G}}{3s\bar{K} + s\bar{G}} \text{ and } s\bar{v} = \frac{3s\bar{K} - 2s\bar{G}}{2(3s\bar{K} + s\bar{G})}, \tag{25}$$

where $\bar{E}, \bar{K}, \bar{G}, \bar{v}$ represent the Laplace transforms of apparent cement paste VE/VP Young's modulus, VE/VP bulk modulus, VE/VP shear modulus and VE/VP Poisson's ratio. The variable s is the Laplace transformed (time) variable. In order to evaluate any potential anisotropy, simulations were performed whereby different strain magnitudes were applied along different axes, the VE/VP moduli calculated, then the axes interchanged and the moduli recalculated. Comparison of the results from the two simulations indicated negligible difference, confirming the isotropy assumption. To evaluate potential differences in response to constant state of stress versus the imposed, constant state of strain primarily utilized in our simulations, we performed creep simulations that yielded VE/VP compliance, which when converted to VE/VP moduli via Laplace transformations, yielded the same results as the relaxation simulations.

As mentioned in section 2.2, a major challenge in predicting the VE/VP behavior of cement paste is that microstructure evolution associated with hydration (i.e., dissolution of cement phases and precipitation of hydrates) occurs over the same time scale as VE/VP relaxation. This change of internal structure leads to stress and strain redistribution inside the whole composite. The key assumption in the model discussed herein is that when there is phase change in one voxel between two successive time steps (e.g., C_3S to C-S-H), stress carried by the original phase would be redistributed to surrounding phases upon dissolution (thus increasing the stress carried by these phases), resulting in an apparent VE/VP deformation. This assumption implies that stress redistribution takes place much faster than chemical phase changes. Meanwhile, the newly formed phases must form in a stress-free state that conforms to the preexisting deformed configuration, and no historical responses in this voxel before formation occurs should be included in the finite element calculation. As a result, apparent strain is produced inside the microstructure and information regarding apparent strain must be stored in the finite element formulation for calculation purposes.

2.2.3 Logic flow of the computational scheme

To illustrate the process of the VE/VP model more specifically, Figure 4 shows the simplified flow chart for the computational scheme. At the first time step in the model, a strain-controlled periodic boundary condition is applied on the microstructure of a particular age, and the finite element calculation is carried out based on historical responses of each voxel and the loading histories. With the calculated stress and strain histories in each voxel, the total energy stored in the whole microstructure is calculated and minimized at each time step to determine the resultant stress and strain fields inside the microstructure, which are then spatially averaged to calculate the VE/VP moduli at the macroscopic scale.

At each subsequent time step, the new microstructure for the age corresponding to that time step is input into the model and comparison between the previous microstructure and the current microstructure is carried out on every voxel to check for phase change. Voxels with phase change are recorded and the previous mechanical responses of such voxels are disregarded in future calculations. Furthermore, any stresses within the dissolved phase are redistributed to the surrounding voxels. The VE moduli of phase-changed voxels are relaxed according to the loading histories subsequent to the time they are formed during all the following time steps. That is, if one voxel experiences phase change at the i^{th} time step ($t = t_0$), in all subsequent time steps the moduli of this specified voxel are no longer based on the mechanical

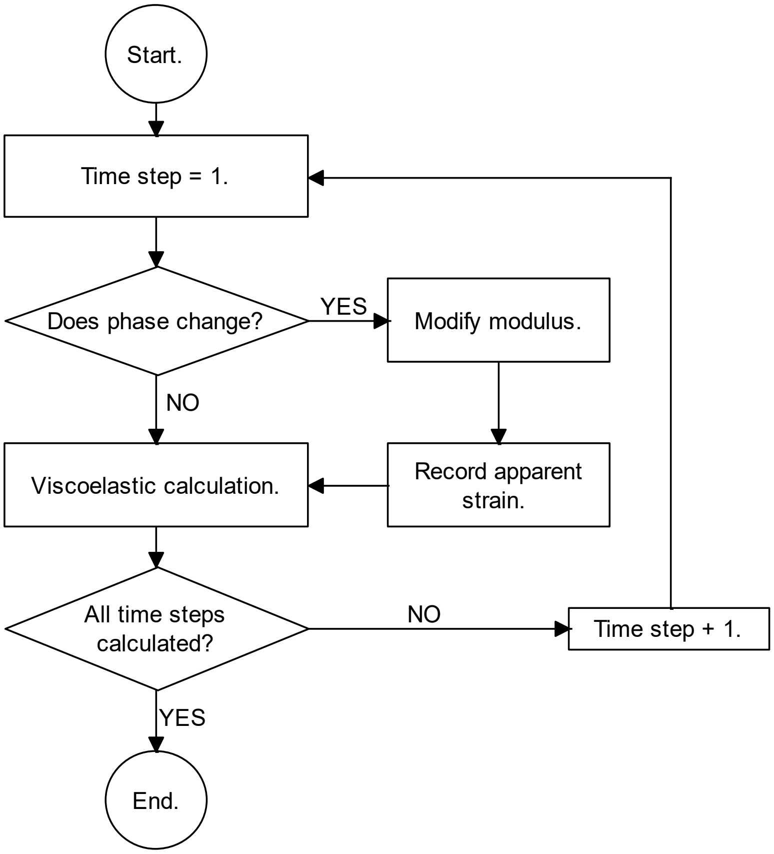

Figure 4 *Simplified flow chart for the computational finite element procedure predicting the apparent VE/VP behavior of cement paste.*

properties of the previous phase, but on the current changed phase. If the voxel is switched to an elastic phase, the moduli of this voxel are kept constant in all the following time steps with the current phase elastic moduli; if the voxel is switched to a VE phase (such as C-S-H), the moduli of this voxel would be assigned a VE moduli with the relaxation starting at time $t = t_0$, the time at which phase change occurs, for all the following time steps. Calculations are carried out based on the renewed response histories and moduli. The second step in the routine is repeated until all time steps are complete.

The computational scheme and associated material model allows investigation of relaxation caused by both intrinsic C-S-H viscoelasticity and microstructure evolution concurrently. It also can separately model the VE/VP relaxation of cement paste due strictly to intrinsic C-S-H relaxation or the apparent VE/VP relaxation of cement paste due strictly to dissolution of certain phases. One can evaluate the contribution of intrinsic relaxation to the overall VE/VP behavior by defining a unique VE or VP constitutive property for any given phase while utilizing unchanging microstructure for all time steps or one can strictly examine the effect of microstructure evolution by utilizing time-evolving microstructures of composites with purely elastic phases. This separation allows us to judge the relative magnitude of these two sources of VE/VP behavior, as compared to experiment, which always mixes the two sources.

2.2.4 Model validation

The advantage of the newly generated model and finite element implementation is that it is able to simulate apparent VE/VP effects that occur due to microstructure evolution while simultaneously considering intrinsic VE/VP properties associated with phases that exhibit VE/VP behavior. As far as the author is aware, there are no commercially available FEM software packages capable of validating this novel aspect of the new software. However, a simple simulation was performed to evaluate the physical rationality of the computed results. The simulation considered a THAMES generated microstructure for a 0.40 *w/c* cement paste (simulated under an isothermal condition of 25° C) that utilized chemical and physical data for a certain well-characterized portland cement. Microstructure snapshots were taken over the course of several days of age. Each phase in the microstructure was assigned elastic properties taken from [22], except C-S-H was assigned a VE Young's modulus prescribed as $E(t) = 11.2 + 11.2\exp\left(-0.2t\right)\ \mathrm{GPa}$, which allows 50% of the instantaneous elastic Young's modulus to be relaxed as $t \to \infty$. The Poisson's ratio of the C-S-H was prescribed to be time-independent as $\nu = 0.25$. As shown in Figure 5(a), during the first 13 days, a constant periodic bulk strain ($\varepsilon_{11}=\varepsilon_{22}=\varepsilon_{33}$) of 0.01 was applied to the composite material, and this applied strain was suddenly removed at the 13th day, forcing the material to return back to its original geometry of zero bulk strain.

Figure 5(b) shows the apparent macroscopic volumetric stress (the average value of σ_{11}, σ_{22} and σ_{33}) of the composite predicted by the finite element model. During the first 13 d, the composite showed smooth relaxation under constant controlled strain due to the two stress-relaxation mechanisms (i.e., phase dissolution of cement grains and intrinsic VE properties of the C-S-H), and at the 13th day, with the sudden removal of the periodic bulk strain, the volumetric stress of the material also exhibited a sudden drop. However, instead of returning back to zero as the external controlled strain did, the volumetric stress assumed a negative value. The existence of the residual stress within the composite is not unexpected. As illustrated conceptually by the diagrams in Figure 5(b), when a controlled strain is applied, the existing phases deform under the external boundary condition. During the hydration process, some phases inside the composite

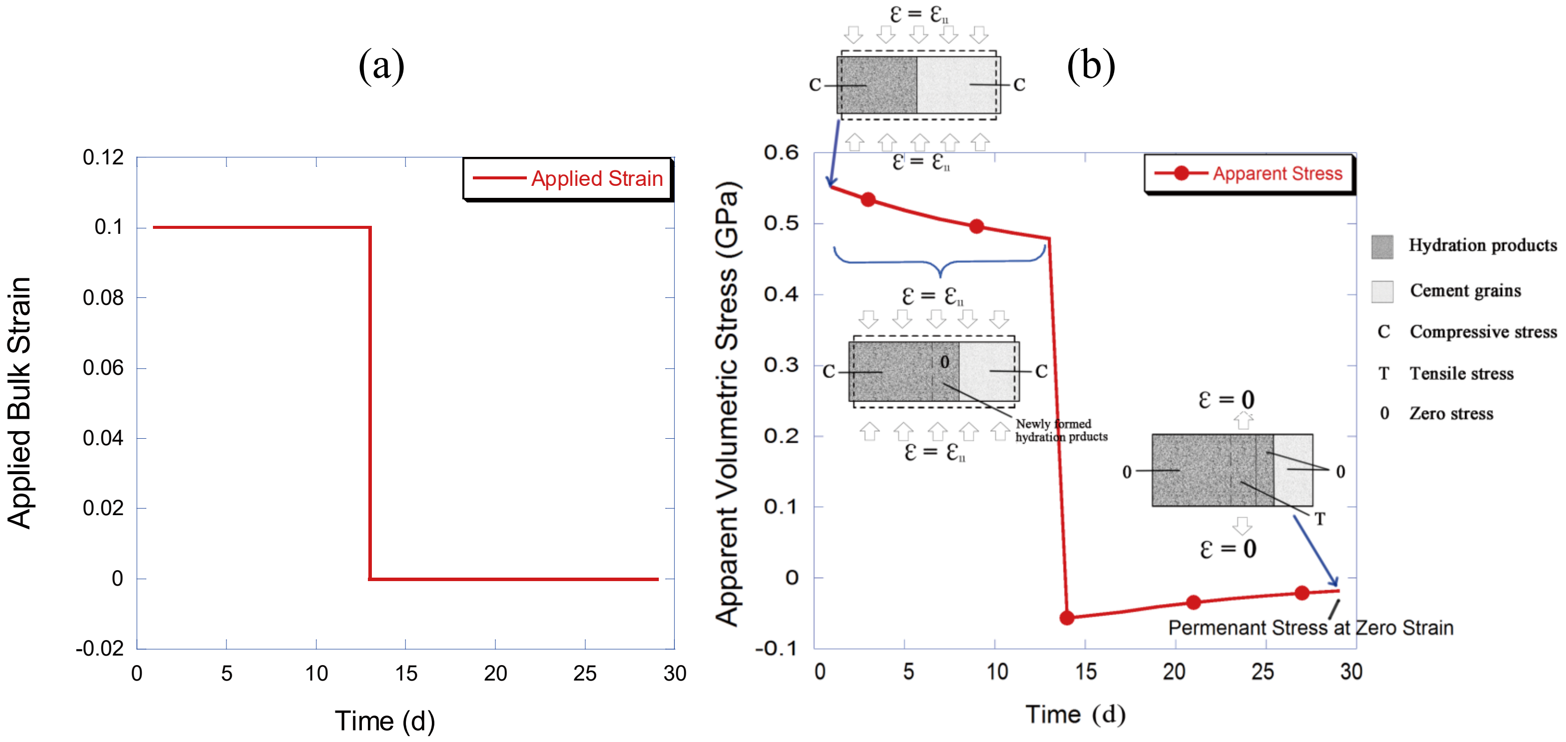

Figure 5 *Virtual experiment of 0.40 w/c cement paste with an evolving microstructure under a virtual strain controlled boundary condition. (a) Virtual applied bulk strain history with a sudden removal at 13th day. (b) Mechanical response (apparent volumetric stress) of viscoelastic composite material under boundary history (a). The VE Young's modulus of C-S-H was assumed to be* $E(t) = 11.2 + 11.2e^{-0.2t}\,GPa$*, where t is in days and the Poisson's ratio of C-S-H was assumed to be a constant value of 0.25. The elastic properties of all other phases were taken from [22]. As illustrated by diagrams using simplified parallel phase geometry, the sudden drop of the apparent volumetric stress into a negative magnitude was associated with the tensile pressure required to force those phases formed after the initial application of bulk strain back to a zero strain condition.*

material dissolve and form new phases in the deformed configuration in a stress-free state. When the bulk strain of the microstructure was suddenly forced back to zero in the simulation, opposing stresses were necessarily generated within the latter-formed phases, leading to a negative volumetric stress. A very simple model, a spring of length L, serves to further illustrate this point. Suppose the spring is extended in tension by an amount x and held there. Another spring is added in parallel, of unextended length $L^{/} = L + x$. This second spring is longer, but carries no force. When the first spring is released, it will not relax all the way back to zero extension but will retain some amount of tension since the second spring will be simultaneously pulled into compression.

3. CREEP/RELAXATION CAUSED BY C-S-H VISCOELASTICITY AND C-S-H AGING[*]

To investigate the mechanisms of cement paste VE/VP behavior, simulations are first carried out to predict the effect of intrinsic C-S-H viscoelasticity as well as C-S-H aging on the overall VE/VP behavior of cement paste.

3.1 Intrinsic C-S-H viscoelasticity

Intrinsic viscoelasticity of C-S-H has been historically regarded as the primary mechanism leading to cement paste VE/VP behavior. However, recent experimental results suggest that C-S-H may not exhibit as much creep and relaxation as previously thought [59]. A clear demonstration is required to show the contribution of C-S-H intrinsic viscoelasticity towards overall cement paste VE/VP properties. Thus, a simulation was performed where dissolution effects were ignored and periodic boundary conditions were applied onto non-aging microstructures; that is, the microstructures did not evolve with time during the simulation and the simulated cement paste relaxation was due entirely to inherent C-S-H viscoelasticity. By applying periodic controlled strain on the boundary of a series of microstructures with 100^3 voxels (with the dimension of each voxel as 1 μm^3) at different ages, the evolution of apparent cement paste VE/VP Young's modulus can be predicted by the model. All microstructures utilized in the virtual experiments were generated by THAMES on simulated sealed cement pastes of

---

[*] Reprinted with permission from "Modeling the apparent and intrinsic viscoelastic relaxation of hydrating cement paste" by X. Li, Z.C. Grasley, E.J. Garboczi and J.W. Bullard, 2015. Cement and concrete composites, 55, 322-330. 2017 by Elsevier.

CCRL Proficiency Sample Cement 168, simulated under an isothermal, sealed condition of 25 ℃ (298 K) [60]. Since, due to experimental challenges, there are no sufficient data currently available for modeling creep or relaxation of the C-S-H phase over several days, for simulation purposes, the viscoelastic Young's modulus of C-S-H was assumed to be $E(t) = 11.2 + 11.2e^{-0.2t} GPa$, where *t* is in unit of days and the Poisson's ratio of C-S-H was set to be a time-independent constant value of 0.2. All other phases in the microstructure were assigned to be elastic with properties taken from [22]. Figure 6 shows the apparent VE Young's modulus associated with the response of 0.45 *w/c* paste, where the relaxation was due strictly to the intrinsic viscoelastic relaxation of C-S-H.

In Figure 6, the 1 d cement paste VE/VP Young's modulus was generated by utilizing the 1 d microstructure, and the 28 d VE/VP cement paste Young's modulus was generated by utilizing the 28 d microstructure. After periodic strain boundary conditions were applied, microstructures were no longer allowed to evolve with time. As a result, in these simulations only the VE properties of C-S-H induced relaxation in the bulk cement paste.

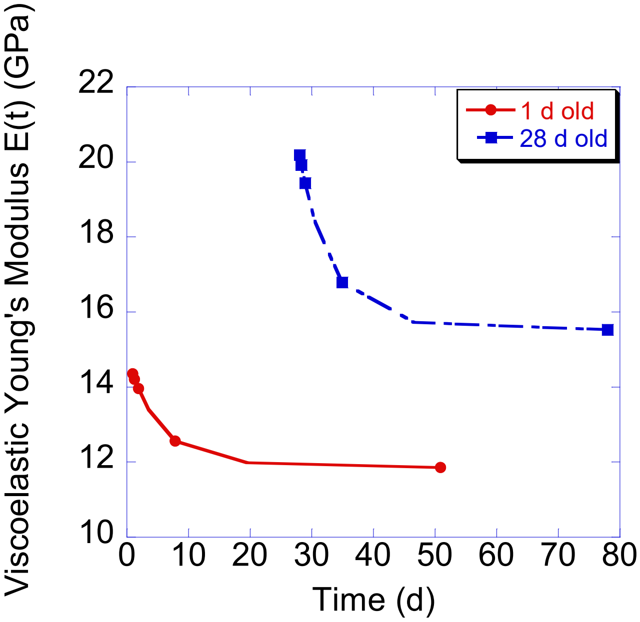

Figure 6 *VE Young's modulus for 0.45 w/c cement paste at different ages (1 d old and 28 d old) when the dissolution effect was ignored. The VE Young's modulus of C-S-H was assumed to be* $E(t) = 11.2 + 11.2e^{-0.2t} GPa$*, where t is in days and the Poisson's ratio of C-S-H was assumed to be a constant value of 0.2. The elastic properties of all other phases were taken from [22]. In this graph, all relaxation was due to intrinsic C-S-H viscoelastic relaxation.*

According to the simulation results, a 28 d cement paste would exhibit more relaxation than a 1 d cement paste. The reason behind the predicted higher relaxation for older materials is that as volume fraction of C-S-H increases with age, so does the fraction of the stress transmitted by C-S-H. If C-S-H is the only phase in cement paste able to relax stress, more C-S-H would thus result in more overall stress relaxation. However, these predictions are in contrast to existing experimental evidence [61, 62], which shows that relaxation or creep rates decrease with age (i.e., the previously mentioned aging effect). Therefore, according to these simulations, C-S-H relaxation cannot be the primary mechanism of early-age cement paste VE/VP behavior unless the VE properties of the C-S-H itself dramatically change with age. If C-S-H phases experience significant aging, the functions for C-S-H VE moduli must vary relative to the age when specific particles of C-S-H are formed.

3.2 C-S-H aging

3.2.1 C-S-H aging implementation

It has often been suggested that the aging effect of concrete is due to intrinsic aging of C-S-H properties, which can occur due to either polymerization [63] or densification [64]. Meanwhile, as hydration progresses, the volume fraction of C-S-H also increases with age. Many modeling approaches (such as the solidification theory [65, 66] and solidification theory incorporating intrinsic C-S-H aging [20]) have been developed to predict the aging behavior of concrete. However, according to the discussions in section 3.1 and in [67, 68], increases in C-S-H volume fraction yields more creep/relaxation simply because a larger volume fraction of C-S-H requires a greater fraction of the composite stress to be transmitted through C-S-H phases (and thus more creep/relaxation associated with C-S-H phases). In the traditional modeling approaches, it is assumed that cement grains are incapable of carrying stresses and the averaged stress carried by C-S-H phases *decreases* with as the volume fraction of C-S-H increases. Thus, a modeling approach (such as existing analytical approaches) that neglects the fact that cement grains carry stress is inadequate to capture the effect of C-S-H aging on macroscale

VE/VP properties of cement paste, motivating the utilization of the above-mentioned model to predict the overall VE/VP behavior of cement paste.

In the previous VE/VP moduli prediction model, all the hydrated and unhydrated phases (except C-S-H) were assigned age-independent linearly isotropic elastic moduli. As intrinsic C-S-H aging properties would lead to less overall relaxation in cement paste, to include this mechanism into the computational scheme, the finite element calculation, where the moduli of each phase were assigned, was modified in such a way that C-S-H phases formed at different ages or different time steps were treated as different phases. Each of these phases was assigned different VE/VP mechanical properties based on the initial non-aging VE/VP properties of C-S-H, the aging function of C-S-H, and the time when a specific C-S-H particle is formed. THAMES and finite element code can easily handle the many phases necessary.

The time-age superposition method [55], a conventional way to model the age-evolving properties of aging VE/VP materials, was used to model the aging VE/VP moduli of C-S-H phases. According to the time-age superposition method, the effect of different ages is incorporated by simply shifting the retardation or relaxation times without changing the shape of the compliance or moduli functions of the materials on the log time scale. By selecting one age to be the reference age or the 'master' age, the retardation or relaxation times for the other ages can be simply shifted by a constant time shift factor a_j [20]

$$a = (\mathrm{t}/t_{ref})^{f} \quad , \tag{26}$$

where t is the age of C-S-H. The aging factor f in eq. (26) is a constant (constitutive) factor throughout each simulation, and controls the aging rate of C-S-H. By simply changing the value of the aging factor f, all of the time shift factors at different ages change simultaneously. Note that as aging and relaxation occurs simultaneously on the same time scale, the constitutive equation for aging C-S-H can be written as [69]

$$\sigma_{11}\left(t : f, t_{ref}\right) = \int_0^t E\left(\xi(t) - \xi(s)\right) \frac{d\varepsilon_{11}(s)}{ds} ds \,, \tag{27}$$

where $E(t)$ is the reference age viscoelastic Young's modulus, $\sigma_{11}(t : f, t_{ref})$ is the axial stress function, $\varepsilon_{11}(t)$ is the axial time-dependent strain, and $\xi(t)$ is a pseudo-time expressed as

$$\xi(t) - \xi(s) = \int_s^t \frac{ds'}{a(s')} \,. \tag{28}$$

From the above three equations, one can see that when $f = 0$, the C-S-H phases are non-aging materials whose mechanical properties do not evolve with age. As the value of f increases the time shift factor also increases, yielding a faster and more obvious aging effect on the resultant VE properties of C-S-H. Thus, by comparing the simulation results with different input values of f, the influence of intrinsic C-S-H aging towards the overall VE/VP relaxation of cement paste can be evaluated.

While one could devise an analytical composite model using a simplified geometry (parallel, composite spheres, etc.) to simulate an aging, viscoelastic, composite material, the computationally implemented model described herein allows one to simultaneously capture effects induced by phase dissolution and to assign particular constitutive behavior to each individual phase (i.e., C-S-H, CH, etc.). Thus, the results from these simulations provide enhanced insight into aging, creep, and relaxation beyond that attainable from classical, analytical models.

3.2.2 Simulation results & discussions

Several virtual experiments were performed to probe the contribution of intrinsic C-S-H aging to the overall early age (*i.e.*, approximately one day to two month) VE/VP behavior of cement paste. A series of microstructures with 100^3 voxels (the volume of each cube-shaped voxel is 1 μm^3) at different ages were utilized in the computational model to predict the time-evolving apparent VE/VP Young's modulus and the apparent VE/VP Poisson's ratio of cement paste. All microstructures utilized in the virtual experiments were generated by THAMES on simulated cement pastes of the ASTM Cement and Concrete Reference Laboratory (CCRL: http://www.ccrl.us/) Proficiency Sample Cement 168 [60] under isothermal, sealed conditions of 25 ℃ (298 K), and the elastic moduli of each phase (e.g., C_3S, C-S-H) were taken from previous studies [22].

One thing to note about the utilized microstructures is that, in reality, for the volume of 1 cubic micron voxel size, multiple phases might exist within this volume rather than one single phase. For the voxels of C-S-H phase analyzed in the microstructure model, nanosclae porosity as well as nanoscale CH could reside within this volume, intermixed with the predominant C-S-H. In the computational model, when assigning mechanical properties to these 1 μm^3 C-S-H voxels, the "mean field" properties of this volume of "C-S-H phases" are utilized, which means that the assigned mechanical properties for each C-S-H voxel inherently account for the porosity or nanoscale CH that might reside within this 1 μm^3 volume; this is accomplished by utilizing mechanical properties obtained from experimental investigations probing a similar length scale (e.g., nanoindentation tests that probe a roughly 1 micron cube interaction volume). Thus, in this dissertation, the "intrinsic properties of C-S-H" refers to the "mean field" properties of C-S-H.

From previous sections, the main reason that C-S-H viscoelasticity was determined unlikely as the dominant mechanism leading to the VE/VP relaxation of cement paste is the fact that this mechanism gives conflicting simulation results of the cement paste aging effect in comparison to experimental evidence [61, 62]. According to the previous simulation results, older cement paste specimens exhibit larger relaxation if C-S-H viscoelastic properties do not age because of the higher C-S-H volume fractions in older, more fully hydrated specimens. However, myriad experimental data indicate that older specimens exhibit lower rates of relaxation than younger specimens. Previous simulations assigned a non-aging VE/VP constitutive function for C-S-H. Incorporating the intrinsic C-S-H aging effect into the computational model so that the overall time-dependent properties of C-S-H evolve with age may yield different early age cement paste aging effects.

As discussed in section 3.2.1, changing the values of the aging factor f enables one to evaluate by virtual experiments the effect of intrinsic C-S-H aging on the overall VE/VP relaxation of cement paste. In this dissertation, the reference age t_{ref} in eq. (26) was set to be equal to 7 d, and the VE Young's modulus of C-S-H at the reference age in Eqs. (27) and (28) was prescribed as $E(t) = 11.2\text{ GPa} + 11.2\exp(-0.2t)\text{ GPa}$, where t denotes the loading time of each specific C-S-H voxel, while the Poisson's ratio of C-S-H was assumed to have a time-independent value of 0.25. The choice of reference age is arbitrary, so long as one is consistent in shifting all other ages to the relaxation function determined for the reference age. The aging factor was assigned to be $f = 0.7$, 1.4, 2.1 or 2.8 to simulate different aging rates. All the other phases were assumed to be purely elastic with constant mechanical properties.

Figure 7 shows the simulation results for a 0.40 *w/c* cement paste with different C-S-H aging factors. These simulation results were generated using a fixed microstructure to eliminate any relaxation effects due to hydration, so that relaxations occur solely by C-S-H time-dependent properties. The non-aging, 1 d curve was generated at the loading age of 1 d, and the other curves were generated at the loading age of 7 d.

Figure 7 shows that faster C-S-H aging (*i.e.*, higher f) results in less relaxation in the apparent VE/VP Young's modulus of the composite. When the aging factor is increased to a sufficiently large value, 7 d specimens potentially can exhibit slower relaxation than the 1 d old specimen, especially for the case when $f = 2.1$ and $f = 2.8$. As already described, simulations suggested that C-S-H relaxation could not be the primary mechanism of early age cement paste VE/VP behavior because that mechanism alone implies greater overall relaxation in older specimens, in conflict with experimental data. However, the new simulations shown here demonstrate that the well-known aging effect can be recovered by introducing intrinsic aging of the C-S-H constitutive properties.

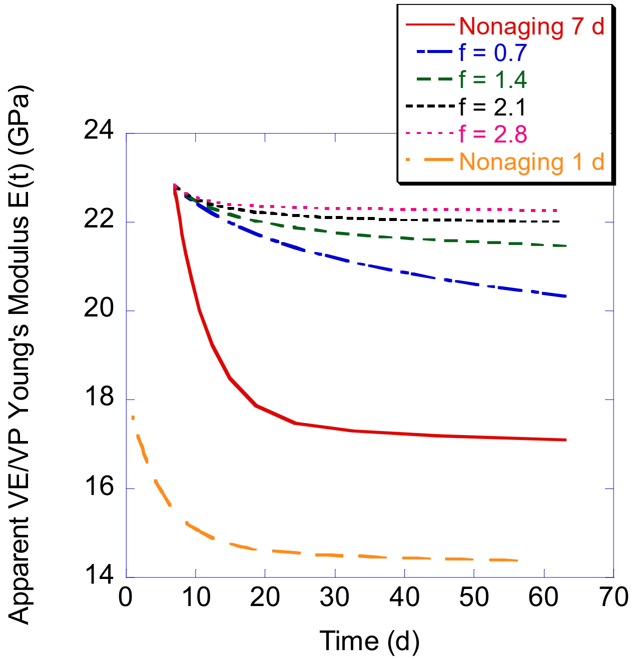

Figure 7 *Apparent VE/VP Young's modulus for 0.40 w/c at the loading age of 1 d and 7 d under different intrinsic C-S-H aging conditions. The VE/VP behavior was considered to occur due to intrinsic C-S-H time-dependent behavior while ignoring dissolution effects. The non-aging E(t) due to loading at 1 d is included in this figure as a comparison.*

Through utilizing unchanging microstructures at each specific age, Figure 8 shows the simulation results of the 0.40 *w/c* cement paste subject to loading at ages of 1 d, 7 d, 14 d and 28 d when assigned with different aging factors *f* = 0 (no C-S-H aging), 0.7, 1.4 or 2.1. The C-S-H phase was assigned a VE Young's modulus prescribed as $E(t) = 11.2\ \text{GPa} + 11.2\exp(-0.2t)\ \text{GPa}$ at the reference age of 1 d, and the Poisson's ratio of C-S-H was fixed to a constant 0.25. All the other phases are treated as purely elastic with constant mechanical properties. Apparent VE/VP Young modulus of the cement paste composite, which are normalized by the instantaneous elastic Young's modulus of each cement paste composite, are shown in Figure 8.

Figure 8 (a)-(b) show that older specimens exhibit larger and faster relaxation than younger specimens when f is small (little aging effect). When the aging factor for C-S-H is higher, as shown in Figure 8 (c)-(d), older specimens relax slower than younger ones, which is in agreement with myriad experimental data regarding aging viscoelasticity in cement paste. Thus, we have confirmed the hypothesis that the aging VE/VP behavior of cement paste may be accounted for strictly by time-dependent behavior of the C-S-H, provided that the viscoelastic properties of the C-S-H exhibit strong enough aging. This finding should not be construed to indicate that strong C-S-H aging is *necessary* for cement paste to exhibit aging viscoelastic behavior, only that it is theoretically *sufficient*. To investigate more thoroughly how cement paste at different loading ages responds to the intrinsic aging rate of C-S-H phases, or to investigate how sensitive cement pastes at different loading ages are to changes in f, Figure 9 shows the normalized apparent VE/VP Young's modulus of cement paste (which are normalized by the instantaneous elastic Young's modulus of each cement paste composite) after 56 d of loading versus the change in the aging factor f. This figure uses the same data as in Figure 8, plus one more set generated with $f = 2.8$; if the cement paste is loaded at 14 d, the normalized VE/VP Young's modulus after 56 d of loading, which is at an actual age of 70 d, was used in the figure.

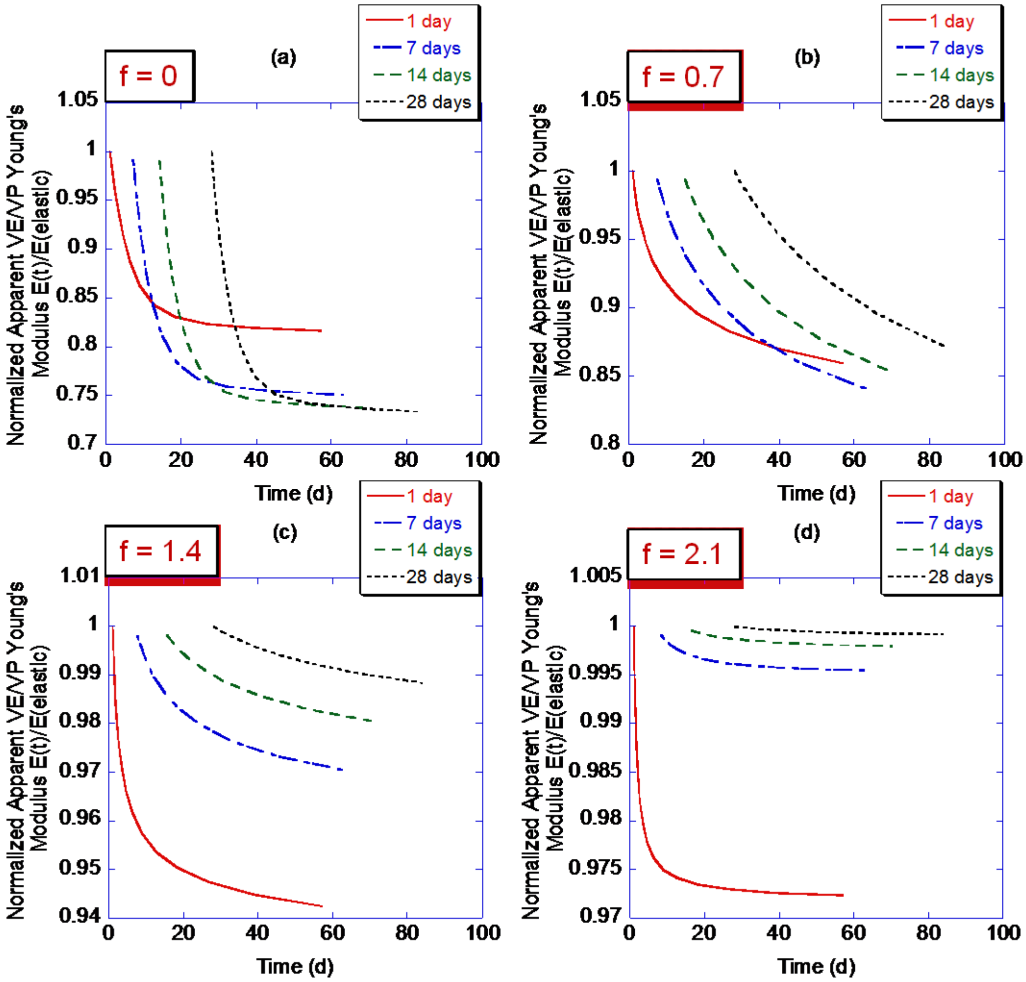

Figure 8 *Apparent VE/VP Young's modulus for 0.40 w/c cement paste at different loading ages with different aging factors of (a) f=0 (non-aging), (b) f=0.7, (c) f=1.4 and (d) f= 2.1*

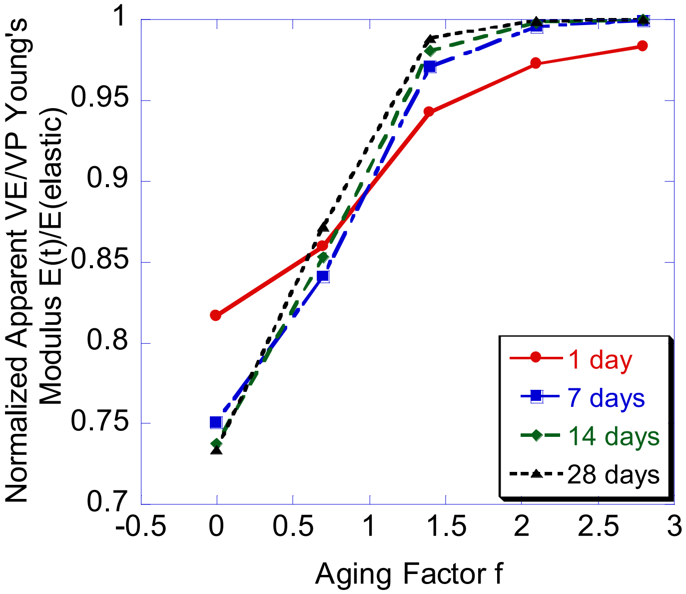

Figure 9 *Normalized apparent VE/VP Young's modulus of 0.4 w/c cement paste after being subjected to 56 d of constant controlled strain applied at the age indicated in the legend versus the aging factor f, where normalization was made by instantaneous elastic Young's modulus. VE/VP behavior was considered to occur due to intrinsic C-S-H time-dependent behavior. The data were selected from the data utilized in generating Figure 8 and one more set of data when the aging factor f = 2.8.*

When the aging factor is small ($f < 0.7$), Figure 9 indicates that cement paste loaded at an earlier age, such as 1 d, has a shallower slope than paste loaded at a later age, meaning that cement pastes are less sensitive to the change in the intrinsic C-S-H aging rate when loaded at earlier ages. The major reason for this phenomenon is that younger specimens have a lower C-S-H volume fraction. When the aging effect is minor (*i.e.*, f is small) and dissolution effects are excluded, the volume of C-S-H dominates the behavior, leading to overall less relaxation in younger specimens, as shown in Figure

8(b). As the aging factor increases, the slopes of the earlier age curves gradually become steeper than later age curves (especially when the aging factor is greater than 1.4), meaning that earlier age cement paste becomes more sensitive to the intrinsic C-S-H aging effect. This phenomenon can be explained from Eqs. (26)-(28). When substituting eq. (26) into eq. (28), under the same reference age t_{ref}, the pseudo-time function has a t^{1-f} dependence, which is more sensitive to changes in f at early ages with smaller values of t, and thereby the C-S-H VE Young's modulus, compared to an older specimen. Thus, from this aspect, younger cement pastes are more sensitive to the change in the values of f, and thus to the intrinsic aging of C-S-H phases.

Additional virtual experiments were also conducted to examine the influence of intrinsic C-S-H aging on cement paste with different *w/c*. Cement pastes with *w/c* varying from 0.35 to 0.5 were subjected to loading at 7 d with one of four different aging factors, $f = 0$, 0.7, 1.4, or 2.1. The C-S-H phase was assigned the same properties as in Figure 8. Figure 10 shows the time evolving apparent VE/VP Young's modulus of

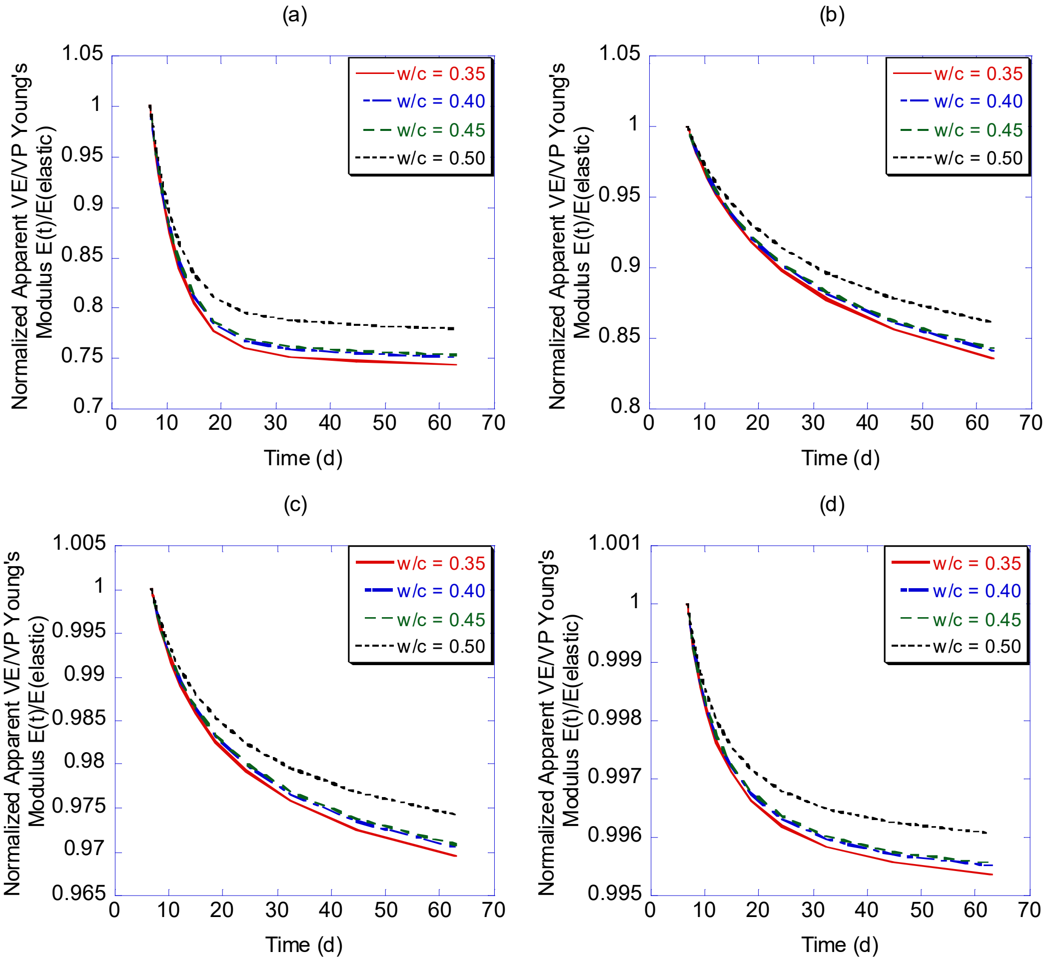

Figure 10 *Normalized apparent VE/VP Young's modulus cement paste with different w/c under the loading age of 7 d with different intrinsic C-S-H aging factors of (a) f=0 (non-aging), (b) f=0.7, (c) f=1.4 and (d) f= 2.1, where normalization was made by the instantaneous elastic Young's modulus.*

the cement paste composites, normalized by the instantaneous elastic Young's modulus, using different values of the aging factor. Figure 10 shows the normalized apparent VE/VP Young's modulus after 56 d of loading versus the change in the aging factor f to demonstrate the sensitivity of different *w/c* cement pastes towards intrinsic C-S-H aging.

From Figure 10 and 11, one can see that in all cases, cement pastes with a lower *w/c* value relax faster and are more sensitive to intrinsic C-S-H aging due to their higher C-S-H volume fractions at early ages [68]. Under the same loading age and the same aging factor, the relative amount of C-S-H phases is the only factor affecting the relative relaxation of cement paste under the mechanism of C-S-H time-dependent properties.

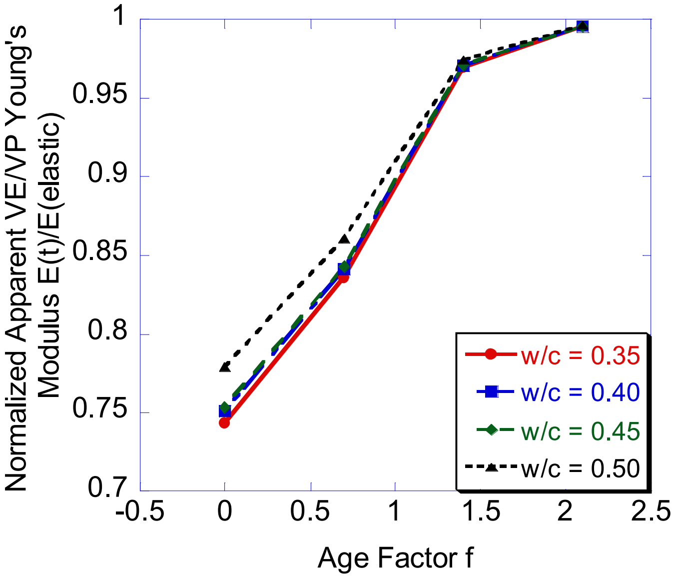

Figure 11 *Normalized apparent VE/VP Young's modulus of cement pastes with different w/c after 56 d of loading (loading age of 7 d) versus the aging factor f, where normalization was made by instantaneous elastic Young's modulus. VE/VP behavior was considered to occur due to intrinsic C-S-H time-dependent behavior. The data was selected from the data utilized in generating Figure 10.*

3.3 Summary

Without aging effect, intrinsic C-S-H viscoelasticity is not likely the primary mechanism leading to the early-age creep and relaxation behavior of cementitious materials; this is because significant C-S-H relaxation results in simulated macroscopic behavior that is in conflict with experimental evidence of early-age aging effects. When intrinsic C-S-H aging operates together with C-S-H viscoelasticity, the modeled time-dependent VE/VP properties of cement paste are consistent with the experimentally observed aging effect on cement paste creep and relaxation rates. With the increasing volume fraction of C-S-H inside cement paste as hydration progresses, the influence of intrinsic C-S-H aging on apparent VE/VP Young's modulus of cement paste likely increases with time.

4. CREEP/RELAXATION CAUSED BY CEMENT GRAIN DISSOLUTION*

Beside C-S-H viscoelasticity/viscoplasticity and C-S-H aging discussed in Chapter 3, cement grain dissolution during the hydration reaction is also a potential mechanism leading to time-dependent behavior of cement paste. To evaluate the apparent VE/VP behavior occurring strictly due to cement grain dissolution, microstructures of cement composites with pure elastic phases (no inherent viscoelasticity) at different ages are considered in this chapter.

4.1 Cement grain dissolution

In the virtual experiments carried out in this chapter, a series of microstructures of sealed cement pastes of CCRL Cement 168 with 100^3 voxels (the volume of each cube-shaped voxel is 1 μm^3) at different ages (from 1 d to 56 d) were utilized under seal condition an isothermal, sealed condition of 25 ℃ (298 K). In this whole chapter, all the simulated microstructure are generated by THAMES, and only the cement grain dissolution during the hydration reaction are considered in the microstructure model, while any potential stress-induced microstructure changes of cement paste are disregarded. Different VE/VP mechanical properties of cement paste, including apparent VE/VP Young's modulus, Poisson's ratio, Bulk modulus and Shear modulus were analyzed in this chapter, especially the first two properties, and their evolution with time all occur strictly as a result of early-age cement grain dissolution.

---

* Reprinted with permission from "Modeling the apparent and intrinsic viscoelastic relaxation of hydrating cement paste" by X. Li, Z.C. Grasley, E.J. Garboczi and J.W. Bullard, 2015. Cement and concrete composites, 55, 322-330. 2017 by Elsevier.

4.1.1 Different loading ages

Figure 11 shows the predicted apparent VE/VP Young's modulus of 0.40 *w/c* cement paste under constant periodic strain boundary condition applied at different ages of 1 d and 7 d. The relaxation shown in Figure 11 was due entirely to the time-dependent dissolution of cement grains. From the predicted results, one can see that the apparent VE/VP behavior caused by dissolution of cement grains is substantial. Thus,

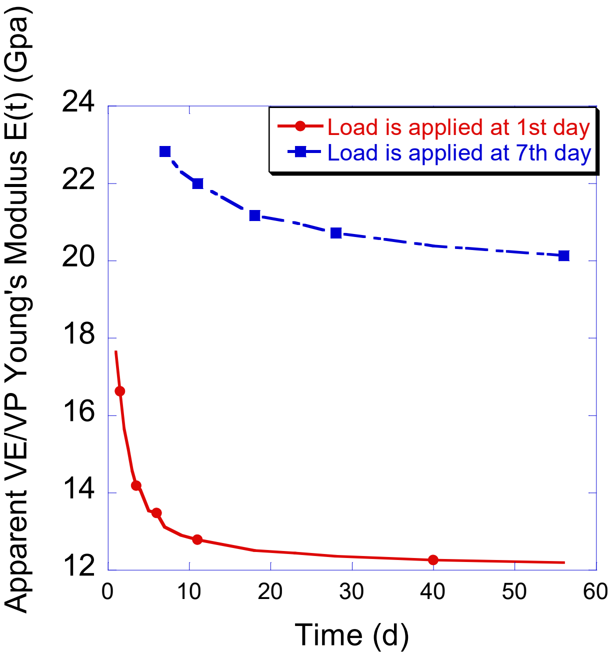

Figure 11 *Apparent VE/VP Young's modulus of 0.40 w/c cement paste when loaded at different ages (1 d and 7 d). In this graph, apparent VE/VP behavior was considered to occur strictly due to dissolution of load bearing cement grains. The dissolution of load bearing cement grains resulted in significant apparent VE/VP behavior for the macroscopic cement pastes, and was able to account for the well-known aging effect of VE/VP behavior of cement paste.*

4.1.2 Different w/c

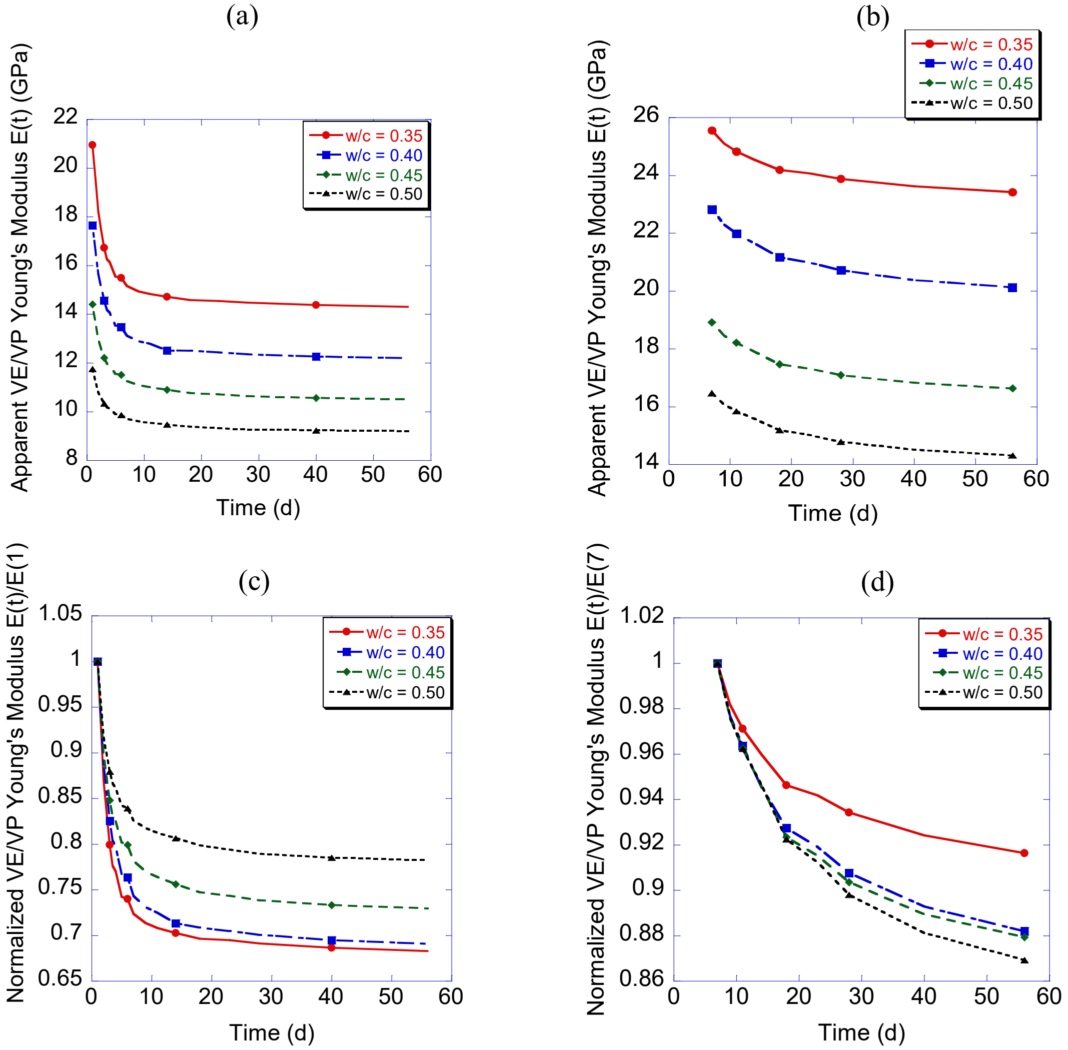

Figure 12 *Apparent viscoelastic Young' modulus for different w/c at loading age of (a) 1 d and (b) 7 d and normalized apparent VE/VP relaxation at loading age of (c) 1 d and (d) 7 d, where apparent VE/VP Young's modulus E(t) was normalized by instantaneous elastic Young's modulus. VE/VP behavior was considered to occur strictly due to microstructure evolution.*

microstructure evolution associated with the hydration process should be included as a significant mechanism in cement paste VE/VP behavior. Additionally, as the rate of relaxation of cement paste slows as cement paste ages (because of the decreasing hydration rate with age), the well-known aging effect of cement paste VE/VP behavior is demonstrated by the hydration-related dissolution mechanism.

To investigate the influence of different values of *w/c* on the apparent VE/VP Young's modulus at different loading ages, microstructures of cement paste with purely elastic phases (with elastic properties taken from [22]) and *w/c* from 0.35 to 0.50 were utilized. In this set of simulations, the VE/VP relaxation of cement paste occurred strictly due to dissolution of load bearing cement grains. Figure 12 shows the predicted results of apparent VE/VP Young's modulus for different values of *w/c* as well as the normalized apparent VE/VP Young's modulus, which are normalized by the instantaneous elastic Young's modulus at loading ages of 1 d and 7 d. As shown in Figure 12(a) and Figure 12(b), older cement pastes establish lower relaxation rates for all different *w/c* considered because of the decreasing hydration rate (and thus dissolution rate) with age, which is consistent with the discussion in previous sections and experimental results. According to Figure 12(c) and Figure 12(d), at an early age of 1 d, the normalized results clearly show that lower *w/c* results in a greater percent relaxation than higher *w/c*. This simulation result agrees with experimental data from Vichit-Vadakan and Scherer [61], which shows that lower *w/c* cement pastes experience larger relaxation than higher *w/c* pastes at early ages. According to the model discussed here, this experimentally observed ranking may occur because dissolution of load bearing cement grains is the dominant factor affecting the relaxation rate at early ages due to the high rate of hydration. As low *w/c* generates higher hydration rate at early age, a larger relaxation rate with low *w/c* paste is observed. At later loading ages, on the other hand, higher *w/c* results in larger relaxation [1]. This larger relaxation for higher *w/c* at later ages is likely due in part to the lower fraction of solid phases in high *w/c* cement pastes, which results in a smaller volume of available stress transferring phases. That is, when load bearing cement grains within a high *w/c* paste dissolve during a single time step, there would be a lower volume of previously formed solid phases (because of the high *w/c*) sharing the redistributed stress, leading to a higher relaxation rate.

4.1.3 Evolution of stresses

Besides the prediction of the effect of age and *w/c* on the apparent VE/VP properties of cement paste, predictions of the evolution of stresses (volumetric stress and deviatoric stress) carried by different phases (hydrated phases and unhydrated phases) inside cement paste composites also become achievable through the computational scheme.

Volumetric stress is the stress tending to change the volume of the body, with magnitude given by

$$p = \frac{\sigma_{11} + \sigma_{22} + \sigma_{33}}{3} = \frac{I_1}{3}, \tag{29}$$

where p is the volumetric stress, I_i are the three invariants of the stress tensor and $\sigma_{11}, \sigma_{22}, \sigma_{33}$ are normal stresses.

Deviatoric stress is the stress tending to distort the stressed body. Components of the stress deviator tensor are given by

$$[s_{ij}] = \begin{pmatrix} s_{11} & s_{12} & s_{13} \\ s_{21} & s_{22} & s_{23} \\ s_{31} & s_{32} & s_{33} \end{pmatrix} = \begin{pmatrix} \sigma_{11} - p & \sigma_{12} & \sigma_{13} \\ \sigma_{21} & \sigma_{22} - p & \sigma_{23} \\ \sigma_{31} & \sigma_{32} & \sigma_{33} - p \end{pmatrix}, \tag{30}$$

where s_{ij} is deviatoric stress, and σ_{ij} are the components of the overall stress tensor. A scalar measure of deviatoric stress magnitude is

$$s = \sqrt{\frac{1}{2} s_{ij} s_{ji}} = \sqrt{\frac{1}{3} I_1^2 - I_2} \ , \tag{31}$$

where s is the scalar deviatoric stress and $i, j = 1, 2$, or 3.

Since both volumetric stress and deviatoric stress are closely related to the three invariants of the stress tensor, their evolution with time can be representative of the corresponding evolutions of the general stress distribution inside the microstructure. Figure 13 shows the predicted evolution of p and s carried by hydrated phases and unhydrated phases at different ages. In this figure, p for each phase is normalized by total volumetric stress carried by the whole microstructure and s for each phase is normalized by total deviatoric stress carried by the whole microstructure. The normalization is expressed according to

$$\sigma(t)_N = \frac{\sum \sigma_{hydrated/unhydrated}(t)}{< \sigma(t) >} \tag{32}$$

where $\sigma(t)_N$ is either normalized volumetric or deviatoric stress at time t, $\sum \sigma_{hydrated/unhydrated}(t)$ is the summed volumetric or deviatoric stress over hydrated or unhydrated voxels at time t, and $< \sigma(t) >$ is the integrated volumetric or deviatoric stress over the whole volume of the microstructure at time t. Microstructures constructed considering 0.40 *w/c* with pure elastic phases at different ages were utilized in the model, and the elastic properties of all phases were taken from [22]. From Figure 13, stresses gradually transfer from unhydrated cement grains to hydrated phases.

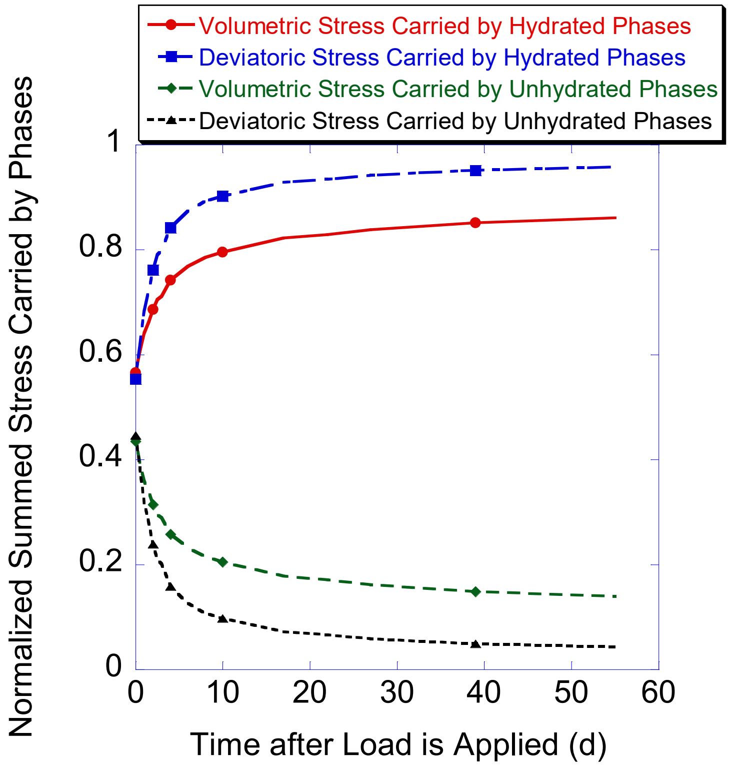

Figure 13 *Normalized volumetric stress and deviatoric stress carried by hydrated phases and unhydrated phases inside cement paste microstructure under loading age of 1 d. The summed volumetric and deviatoric stresses carried by hydrated phases and unhydrated phases at time t are normalized by total volumetric stress or total deviatoric stress carried by the whole microstructure at time t, respectively.*

4.2 Comparison with solidification theory

As C-S-H creep and relaxation has historically been considered the dominant mechanism leading to cement paste creep and relaxation, some constitutive models, such as the solidification theory [70], have been developed based on this understanding. Although the solidification theory appears to have been developed with a uniaxial stress state in mind [71], under any specific boundary conditions, evolutions of volumetric stress and deviatoric stress with time should all be capable of representing the general stress evolutions inside the microstructure, as discussed in previous paragraphs of this section. Due to equilibrium requirements, the normalized, spatially averaged stress carried by the solidified products (equivalent to hydration products) in the solidification theory may be calculated through

$$\sigma(t) = \frac{\sigma_{total}(t)}{\nu(t)} \tag{33}$$

where $\nu(t)$ is the aging function describing the volume fraction of solidified phases, and $\sigma_{total}(t)$ is the normalized total stress, either volumetric stress or deviatoric stress, predicted by the present model. Note that the solidification theory does not allow for any stress being carried by the unhydrated cement, even after the cement paste has set. From a simple composite theory view, it is clear that if solid phases are connected to the main solid backbone, they will carry load. Computations have shown that at lower values of *w/c*, the effective elastic moduli are significantly affected by the unhydrated cement [22].

For comparison purposes, the curves of normalized stresses carried by solidified phases calculated via the new model presented in this project are obtained by summing all normalized stresses carried by the phases that solidify after load is applied. The evolution of stresses carried by the hydration products after the application of load (at age of 1 d) as predicted by the solidification theory and the new model are shown together in Figure 14. The predictions considered a 0.40 w/c cement paste hydrating under isothermal conditions (25° C).

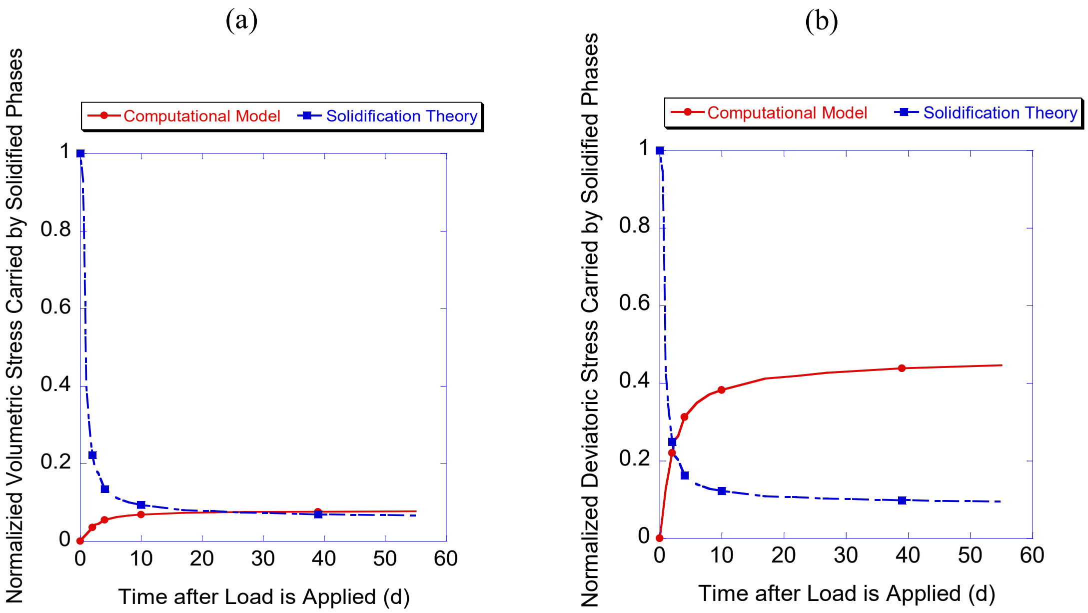

Figure 14 *Comparison between the new model developed herein and the solidification theory regarding normalized (a) volumetric and (b) deviatoric stress carried by solidified phases (hydration products). The stresses are normalized by instantaneous total stress carried by the microstructure.*

The solidification theory predicts that the average stress carried by solidified or hydrated phases decreases with time, which results from the presumption that only solidified phases may transmit stress. The solidification theory implies that hydration products are non-aging viscoelastic materials and aging arises in the bulk scale due to the increase in load bearing materials as a result of solidification and deposition of hydration products. As hydration progresses, each newly formed layer of the hydration products solidifies in a stress-free state and these layers are only subject to loads after they form. As a result of the predicted decrease in stress carried by solidified phases (including C-S-H) as hydration progresses, the solidification theory can account for the early-age aging effect through reduced C-S-H creep as stress in that phase decreases. However, according to the model developed herein and as shown in Figure 13, the total stress carried by solidified phases *increases* with age. This increase occurs because the new model accounts for the fact that stress may be transmitted by both hydrated and unhydrated phases (hydrostatic stresses may be transmitted by cement grains at any age, while deviatoric stresses may only be transmitted once percolation of the solid skeleton has occurred). Since unhydrated phases are allowed to carry stress, their dissolution results in an increase in stress on hydration products. Thus, the solidification theory is only able to capture early-age aging effects while considering C-S-H viscoelasticity as a primary mechanism for early-age cement paste creep and relaxation because the ability of cement grains to transmit stress is neglected.

4.3 Summary

The apparent VE/VP behavior of hydrating cement paste due to dissolution of cement grains is a significant factor in the overall early-age creep and relaxation of the paste. The main reasons behind this are the stress transmission from dissolved load bearing phases to surrounding hydrated phases or cement grains, and the generation of apparent strain in the new components that form in deformed configurations (i.e., the newly formed phases have a deformation gradient but no stress). The comparison between the evolution of stresses within hydration products predicted by the new computational scheme and that predicted by the solidification theory indicates that specific assumption made about the extent to which unhydrated phases can transmit stress is key to interpreting VE/VP mechanisms of cement paste. If one stipulates that unhydrated phases do not carry stress (as with the solidification theory), then increased formation of C-S-H can lead to aging of VE/VP properties of cement paste (e.g., reductions in creep or relaxation rates at later ages). However, as demonstrated by the new computational scheme and model presented herein, if one presumes that unhydrated phases may transmit stress once the solid phases form a percolated network, then their dissolution results in an increase in stress on hydration products as hydration progresses. This increase in stress in the hydration products prevents the increased formation of C-S-H from acting as a source of aging of VE/VP properties of cement paste. Conversely, the slowing of the hydration process with time may contribute strongly to the aging of creep and relaxation of cement paste.

5. EVOLUTION OF APPARENT VE/VP POISSON'S RATIO CAUSED BY BOTH INTRINSIC C-S-H CREEP AND CEMENT GRAIN DISSOLUTION[*]

To fully characterize or predict the three-dimensional stress, strain, and displacement fields in an isotropic material, at least two independent elastic moduli are required. The Poisson's ratio and Young's modulus are the most common moduli pair used in engineering to model isotropic elastic materials. After the thorough discussions on the apparent VE/VP Young's modulus of cement paste in Chapter 3 and Chapter 4, this chapter focuses on the analysis of the time-evolving apparent VE/VP Poisson's ratio due to both the mechanisms of C-S-H creep/relaxation and cement grain dissolution.

5.1 Definition of VE/VP Poisson's ratio

In an axially-loaded material, the Poisson's ratio [72, 73] is defined as the negative of the dimensionless ratio of the strain perpendicular to the loading direction to the strain in the axially loaded direction. When there are changes in the cement paste microstructure during the hydration process, leaving the whole composite with a permanent deformation after boundary conditions are removed. We would like to refer to this irreversible deformation as a viscoplastic process, and thus the term "viscoplastic" is used in this research project along with "viscoelastic." Although a substantial number of theoretical analyses have been carried out on VE/VP behavior in terms of time-

---

[*] Reprinted with permission from "Computing the time evolution of the apparent viscoelastic/viscoplastic Poisson's ratio of hydrating cement paste" by X. Li, Z.C. Grasley, E.J. Garboczi and J.W. Bullard, 2015. Cement and concrete composites, 56, 121-133. 2017 by Elsevier.

dependent moduli, the rigorous definition of VE Poisson's ratio has received limited treatment [18, 21].

Based on the original definition of Poisson's ratio [72, 73], for an isotropic material

$$\upsilon = -\frac{\varepsilon_\perp}{\varepsilon_\parallel}, \tag{34}$$

where υ is Poisson's ratio, $\varepsilon_\perp$ is the strain tensor component perpendicular to the loaded direction and $\varepsilon_\parallel$ denotes the strain tensor component in the axially loaded direction. eq. (34) describes a constitutive property for isotropic elastic materials exhibiting small deformation gradients. However, if one utilizes eq. (34) to describe the VE/VP Poisson's ratio of a given material, significant errors due to stress/strain history might be introduced [8, 18, 21, 74] since $\upsilon(t)$ (where t is time) in eq. (34) is dependent on the stress or strain history. That is, eq. (34) does not express a true constitutive property of a VE/VP material. Recently, an expression for the linear viscoelastic VE/VP Poisson's ratio was derived based on the superposition principle by Lakes and Wineman [75], with the (isotropic mechanical properties) VE/VP Poisson's ratio in the Laplace transform domain expressed as

$$\bar{\upsilon}(s) = -\frac{\bar{\varepsilon}_\perp(s)}{s\bar{\varepsilon}_\parallel(s)} \tag{35}$$

where υ is the VE/VP Poisson's ratio, the overhead lines denote the Laplace transforms of the representative variables, and the variable s is the Laplace transformed time variable. eq. (35) can also be rewritten in time domain as [76]

$$\varepsilon_\perp(t) = \int_0^t \upsilon(t-t')\frac{\partial\varepsilon_\parallel(t')}{\partial t'}dt'. \tag{36}$$

This formulation of VE/VP Poisson's ratio can be treated as a valid material property, which may be related to other linear VE/VP moduli utilizing the correspondence principle [77].

A review of the literature indicates that the VE/VP Poisson's ratio of concrete may be an increasing function of time [78], a decreasing function of time [19], or a constant independent of time [79]. Grasley and Lange found that the VE/VP Poisson's ratio of cement pastes was slightly increasing for some materials and almost constant for others [20]. A VE/VP Poisson's ratio that increases as a function of time indicates that the cement paste relaxes shear stresses faster than dilatational stresses, while a VE/VP Poisson's ratio that decreases with time indicates that the material relaxes dilatational stresses faster than shear stresses, and a constant with time VE/VP Poisson's ratio indicates equivalent relaxation rates for shear and dilatational stresses.

There are likely two main reasons for the discrepancies in the literature regarding the character of the VE/VP Poisson's ratio of concrete. First, experimentalists have frequently utilized improper definitions of VE/VP Poisson's ratio in their data analysis, such as the negative ratio of lateral and axial creep strains in the time domain as in eq. (34). A second likely source of discrepancies is the lack of reliable, accurate experimental data. This promotes the use of the computational scheme to predict the time-evolving value of apparent VE/VP Poisson's ratio.

5.2 Simulation results & discussions

A sequence of virtual experiments have been performed to probe the contribution of each VE/VP mechanism (intrinsic C-S-H viscoelasticity or cement grain dissolution) to the overall early-age (i.e. approximately one day to one month) evolution of the VE/VP Poisson's ratio of cement paste. By applying purely controlled periodic volumetric strain and purely controlled periodic shear strain on the boundary of a series of microstructures with 100^3 voxels (the volume of each cube-shaped voxel is 1 μm^3) at different ages, the evolution of apparent cement paste VE/VP bulk modulus and VE/VP shear modulus were simulated by the model, leading to the calculation of the apparent VE/VP Young's modulus and the apparent VE/VP Poisson's ratio using Eq. (25). All microstructures utilized in the virtual experiments were generated by THAMES on simulated cement pastes of the ASTM CCRL Portland cement 168 under an isothermal, sealed condition of 25 ℃ (298 K) [60], and the elastic moduli of each individual phase inside the composite were taken from previous studies [22]. The pore water in the composite was assumed to be fully compliant and thus did not become pressurized. In reality, the water in the composite would become locally pressurized immediately upon the imposition of stress to the composite boundaries, but this water pressure would be rapidly relaxed as the fluid would flow to nearby air bubbles present from self-desiccation. As the flow distance is so short (never more than a few micrometers), this fluid pressure would be relaxed orders of magnitude faster than the effects of interest in this study.

Cement grain dissolution occurring during the hydration process has a significant influence on the overall VE/VP behavior of cement paste [23]. Figure 15 shows, for several different *w/c,* the simulated time-dependent volume fraction (starting after 1 d of age) vs. time of all the hydration products and the main clinker phases, C_3S, and C_2S, which are indicative of the degree of hydration. One can see that lower w/c materials exhibit a higher hydration rate at early ages but a low hydration rate at later ages than do higher w/c materials. For demonstration purpose, only partial of the data points would be shown in the graphs. The lack of smoothness of some plotted lines is due to numerical oscillations in the data points (not plotted) associated with the coarseness of the time steps.

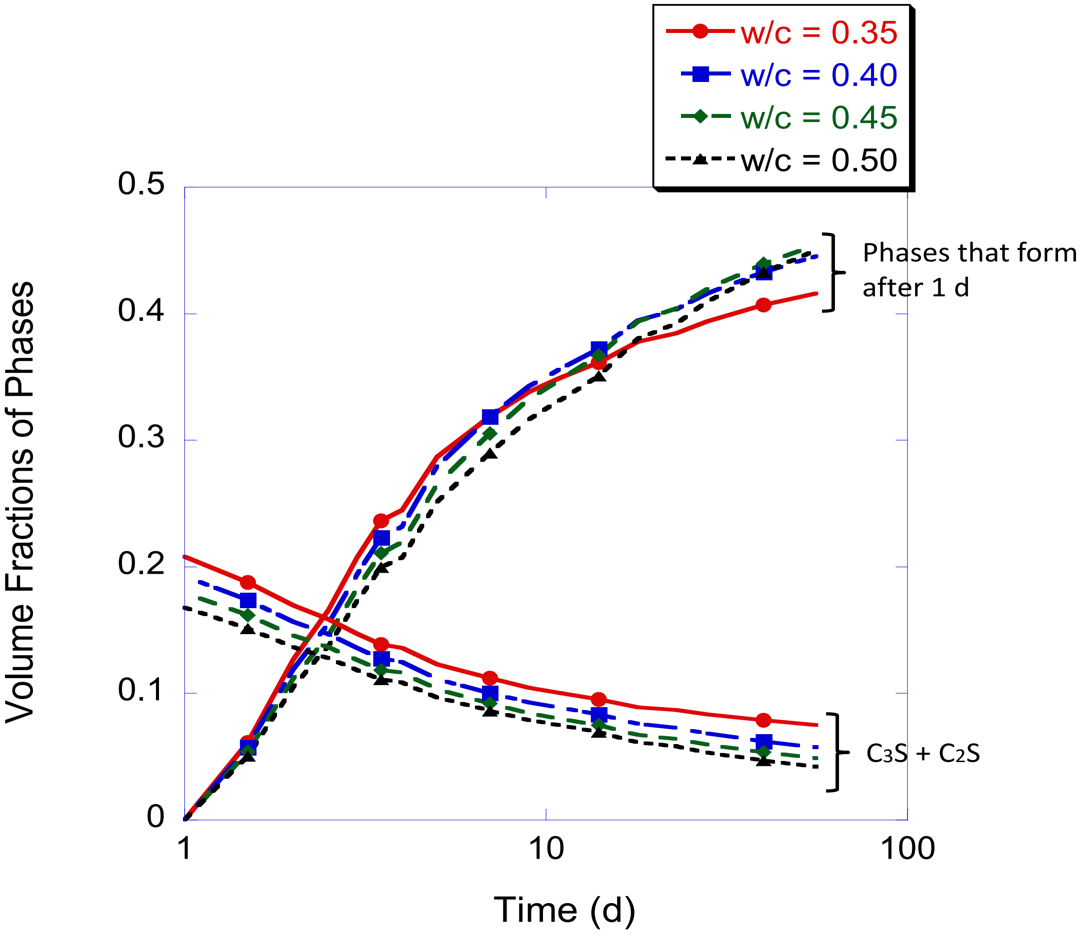

Figure 15 *Simulated volume fractions of the phases that form after 1 d inside cement paste, along with the evolution of C3S and C2S volume fractions. The lines are added as an aid to the eye.*

5.2.1 Poisson's Ratio evolution due to cement grain dissolution

Besides Young's modulus and Poisson's ratio, bulk modulus and shear modulus are the other two most commonly employed mechanical properties in characterizing the mechanical behavior of an isotropic material. Apparent VE/VP bulk modulus and apparent VE/VP shear modulus are closely related to the dilatational stress (the stress tending to change the volume of the body) and the deviatoric stress (the stress tending to distort the stressed body). Relative variations in these two moduli significantly influence the evolution of apparent VE/VP Poisson's ratio, as can been seen from eq. (25). Figure 16 gives the predicted results of apparent VE/VP bulk modulus and apparent VE/VP shear modulus for different values of *w/c* from 0.35 to 0.50 at different loading ages (i.e., the age at which the periodic strain boundary conditions are applied) of 1 d and 7 d, as well as the normalized bulk and shear moduli, which are normalized by the instantaneous elastic moduli at loading ages of 1 d and 7 d. Cement paste microstructures with purely elastic phases (with elastic properties taken from [22]) were utilized, so that in this set of simulations, the VE/VP relaxation of cement paste occurred strictly due to dissolution of load bearing cement grains.

As shown in Figure 16, for both the apparent VE/VP bulk modulus and apparent VE/VP shear modulus, older cement pastes exhibit lower relaxation rates for all *w/c* considered because of the decreasing hydration rate (and thus cement grain dissolution rate) with age. Furthermore, according to the simulation results in Figure 16(e) and Figure 16(f), the apparent VE/VP bulk modulus relaxes more quickly than the apparent VE/VP shear modulus. As the apparent VE/VP bulk modulus decreases faster with respect to the apparent VE/VP shear modulus, cement paste composites become more capable of sustaining volume-deforming strain fields relative to shape-deforming strain fields; in other words, under a controlled strain in the load direction, less deformation in the lateral direction (to prohibit the shape change in bulk composite) would exist inside cement paste at greater lengths of time under load. Therefore, from the simulation results of apparent VE/VP bulk and shear moduli in Figure 16, one should expect a decreasing apparent VE/VP Poisson's ratio with time for all different *w/c* considered, as shown in Figure 17. However, comparing Figure 16(e) and Figure 16(f), the rate of VE/VP bulk modulus relaxation and the apparent VE/VP shear modulus relaxation are much closer at later ages, particularly for lower *w/c* cement paste. As a result, the apparent VE/VP Poisson's ratio would be expected to be much less time-dependent at later ages than it does at earlier ages, as seen in Figure 17.

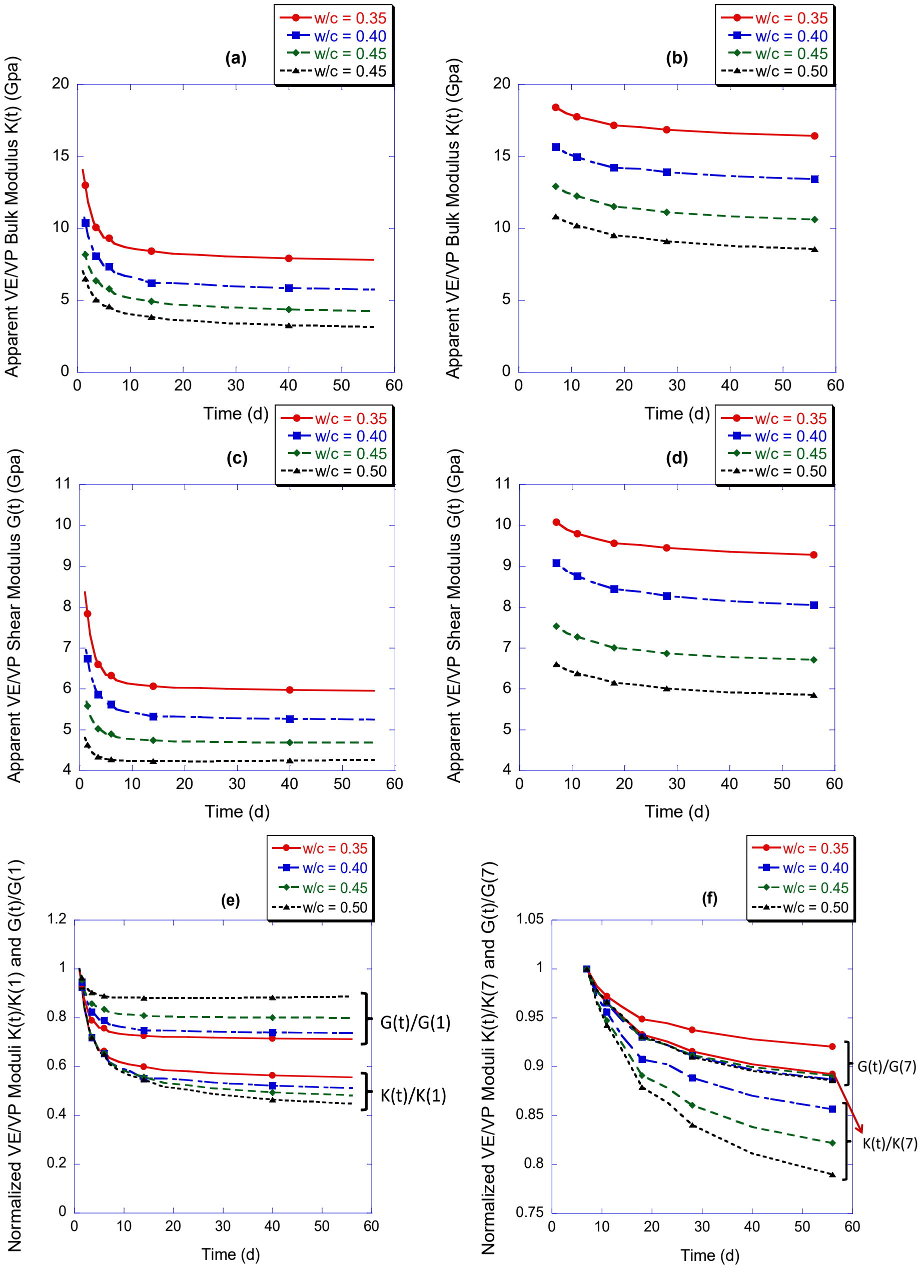

Figure 16 *Apparent VE/VP bulk modulus for different w/c at loading age of (a) 1 d and (b) 7 d, apparent VE/VP shear modulus at loading age of (c) 1 d and (d) 7 d, and normalized apparent VE/VP relaxation at loading age of (e) 1 d and (f) 7 d, where the apparent VE/VP bulk modulus K(t) and shear modulus G(t) were normalized by the instantaneous elastic bulk and shear moduli. VE/VP behavior was considered to occur only due to cement grain dissolution. The lines are added as an aid to the eye, and the y-axis scaling and limits vary among the figures to better demonstrate the trends of the evolution of the changing moduli.*

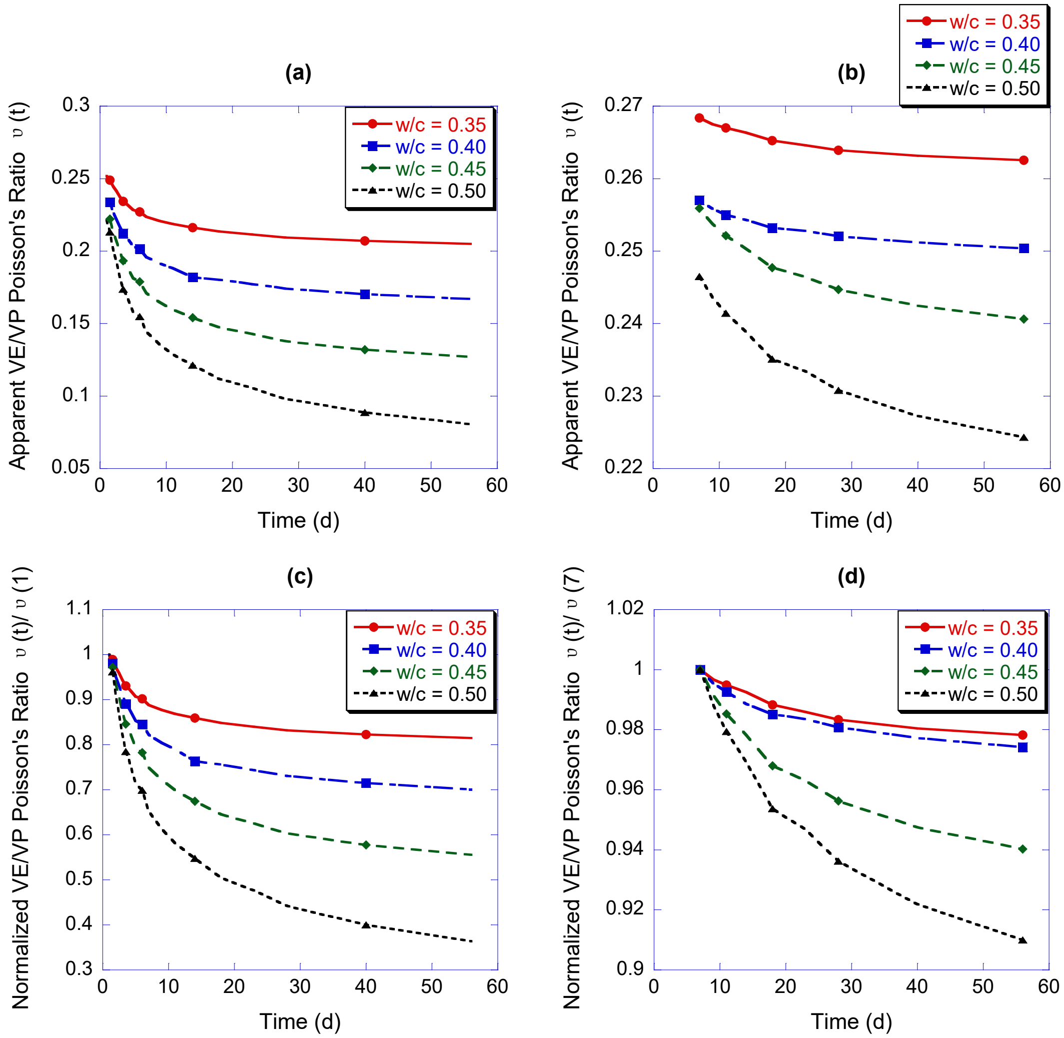

Figure 17 *Apparent VE/VP Poisson's ratio for different w/c at loading age of (a) 1 d and (b) 7 d and normalized apparent VE/VP relaxation at loading age of (c) 1 d and (d) 7 d, where the apparent VE/VP Poisson's ratio* $\upsilon(t)$ *was normalized by the instantaneous elastic Poisson's ratio. VE/VP behavior was considered to occur only due to cement grain dissolution.*

Figure 17 shows the predicted results for the apparent VE/VP Poisson's ratio for different values of *w/c* as well as the normalized apparent VE/VP Poisson's ratio, which are normalized by the instantaneous elastic Poisson's ratio at loading ages of 1 d and 7 d.

The data used to generate Figure 17 originated from the data in Figure 16. From Figure 17, four major observations may be made:

1) Cement paste with higher stiffness (e.g., lower *w/c* and later loading age) exhibits a higher predicted value of the initial elastic Poisson's ratio. Lower *w/c* pastes have higher initial elastic Poisson's ratio because the unhydrated cement clinker (which has a higher Poisson's ratio than the hydrates) carries a higher fraction of the stress in these materials. Furthermore, porosity decreases with reductions in *w/c* and increasing age (or degree of hydration). The dependence of elastic Poisson's ratio of porous materials on the pore volume fraction is not universal, but is rather dependent on pore shapes, pore connectivity, and the Poisson's ratio of the percolated solid between the pores [80]. Finite element simulations on digitized microstructures have indicated that, in agreement with the results herein, for porous materials with an average elastic Poisson's ratio of the solid skeleton exceeding about 0.2, elastic Poisson's ratio increases with decreasing porosity [80].
2) The apparent VE/VP Poisson's ratio decreases with time under load for all *w/c* considered. As cement paste hydrates while under load, stresses are gradually transferred from unhydrated phases (such as C_3S) to hydrated products (such as C-S-H). Since the unhydrated phases normally have a higher Poisson's ratio value than hydrated solids [22], the overall apparent VE/VP Poisson's ratio of the bulk cement paste composite decreases with time under load.

3) At both loading ages, 1 d and 7 d, higher *w/c* results in larger and faster overall relaxation in the apparent VE/VP Poisson's ratio despite its lower hydration rate at early loading age. When load bearing phases inside the cement paste microstructure dissolve, the stresses carried by these phases are distributed into surrounding load bearing phases. For lower *w/c*, at any given degree of hydration, there is a greater content of cement grains, relative to the entire solid backbone consisting of unhydrated cement plus hydration products, available to carry this transferred load than at higher *w/c*. Thus, on dissolution of a given grain, for low *w/c*, a larger fraction of the transferred stress ends up on other cement grains in the solid backbone, which possess a higher Poisson's ratio value than the hydrates, yielding less overall relaxation in apparent VE/VP Poisson's ratio. Figure 18 shows the comparison of the ratio of summed stresses carried by C-S-H phases to that carried by C_3S and C_2S phases for *w/c* of 0.35 and 0.50 at loading age of 1 d. Figure 18 demonstrates the stress transfer rate from cement grains (whose main component is C_3S and C_2S) to hydration products (with the main hydration product of C-S-H) is slower for lower *w/c*, since the slope for β is smaller, thus leading to a lower apparent VE/VP Poisson's ratio relaxation rate.

4) The relaxation rate of apparent VE/VP Poisson's ratio decreases with age as a result of the decreasing dissolution rate of cement grains, which is associated with the decreasing hydration rate with age.

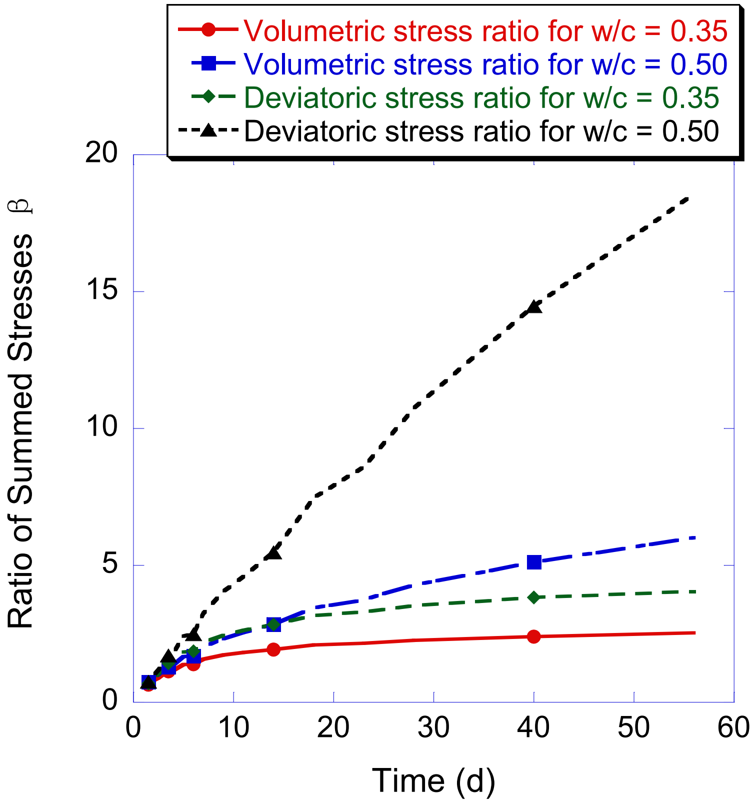

Figure 18 *Ratio, β, of volumetric stress and deviatoric stress carried by C-S-H phases to the stress carried by C3S and C2S phases inside the cement paste microstructure for a loading age of 1 d for w/c of 0.35 and 0.50. VE/VP behavior was considered to occur only due to cement grain dissolution. The ratio β is mathematically defined by* $\beta = \sum \sigma_{C-S-H}(t) / \left(\sum \sigma_{C_3S}(t) + \sum \sigma_{C_2S}(t) \right)$*, where* $\sum$ *indicates a sum over all voxels with a given phases and* σ *is either a scalar measure of dilatational stress or a scalar measure of shear stress magnitude. The lines are added as an aid to the eye.*

5.2.2 Poisson's Ratio evolution due to intrinsic C-S-H viscoelasticity

A sequence of virtual experiments was performed on the evolution of VE/VP Poisson's ratio where the VE/VP effects are attributable entirely to intrinsic C-S-H creep while ignoring the dissolution effects. According to the VE constitutive equation of C-S-

H, $\sigma_{11}(t) = \int_0^t E(t-s)$, C-S-H was assigned a time-dependent VE Young's modulus prescribed as $E(t) = 11.2\ \text{GPa} + 11.2\exp(-0.2t)\ \text{GPa}$, where t denotes the loading time of each specific C-S-H voxel, while the Poisson's ratio of C-S-H was assumed to be independent of time and equal to 0.25. The relaxation function chosen for C-S-H is based on the instantaneous elastic Young's modulus reported in Haecker et al. [22], E(0) = 22.4 GPa, with an assumed 50 % ultimate relaxation. There are little data available in the literature to guide the modeling of C-S-H relaxation. However, the purpose of this research project is to investigate the effect of various mechanisms on the behavior of the macroscopic VE/VP Poisson's ratio – as the observed trends are largely independent of the specific model utilized for C-S-H, the results are considered representative regardless of the actual accuracy of the C-S-H material model. Using these properties, Figure 19 and Figure 20 show the apparent VE/VP bulk modulus, shear modulus and Poisson's ratio for different cement pastes with *w/c* ranging from 0.35 to 0.50 at loading ages of 1 d and 7 d. The relaxation was due strictly to the intrinsic VE/VP relaxation of C-S-H with unchanging microstructure (i.e., no hydration taking place) with respect to time, and all the phases other than C-S-H in the microstructure were assigned to be elastic with properties taken from [22].

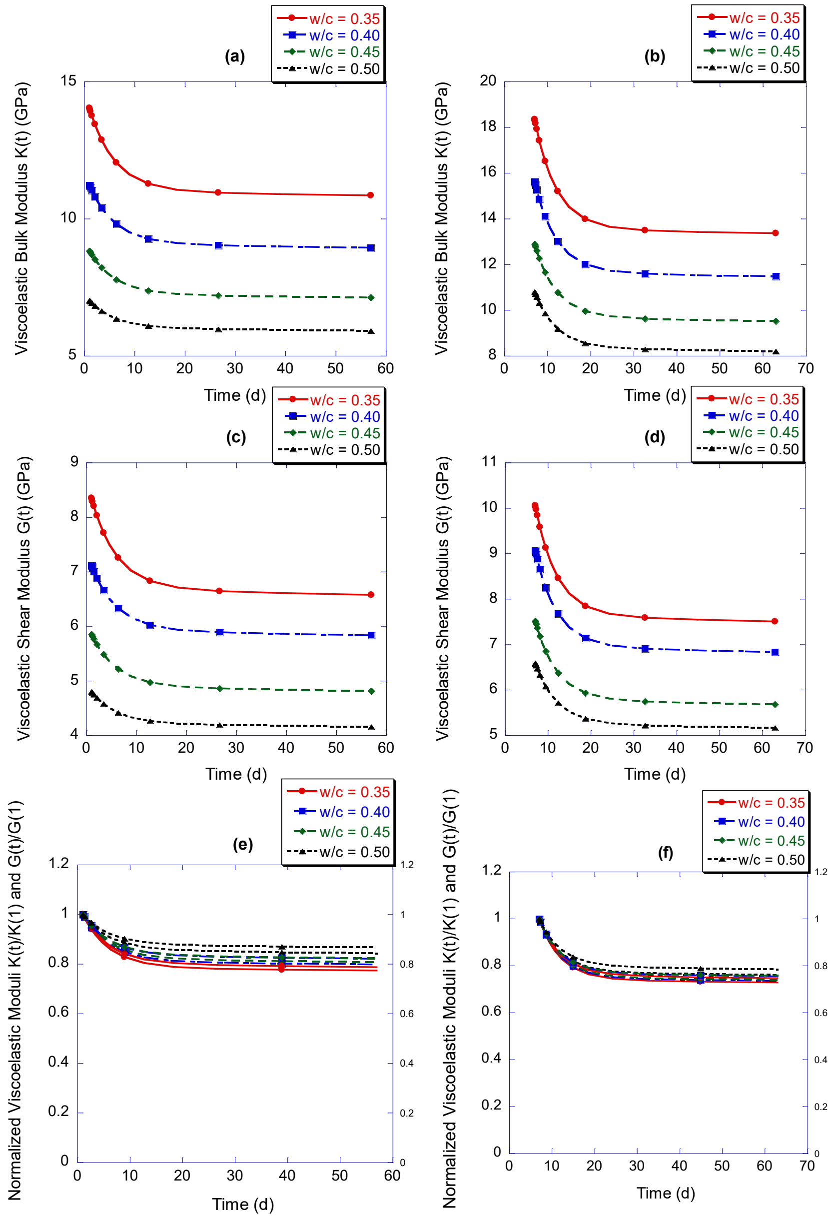

Figure 19 *VE/VP bulk modulus for different w/c at loading age of (a) 1 d and (b) 7 d, VE/VP shear modulus at loading age of (c) 1 d and (d) 7 d, and normalized apparent VE/VP relaxation at loading age of (e) 1 d and (f) 7 d, where the apparent VE/VP bulk modulus K(t) and shear modulus G(t) were normalized by the instantaneous elastic bulk and shear moduli. VE/VP behavior was considered to occur due to intrinsic C-S-H relaxation while ignoring dissolution effects. The VE/VP Young's modulus of C-S-H was assumed to be* $E(t) = 11.2\ \text{GPa} + 11.2\exp(-0.2t)\ \text{GPa}$*, and the Poisson's ratio of C-S-H was assumed to have a constant value of 0.25. The elastic properties of all other phases were taken from [22].*

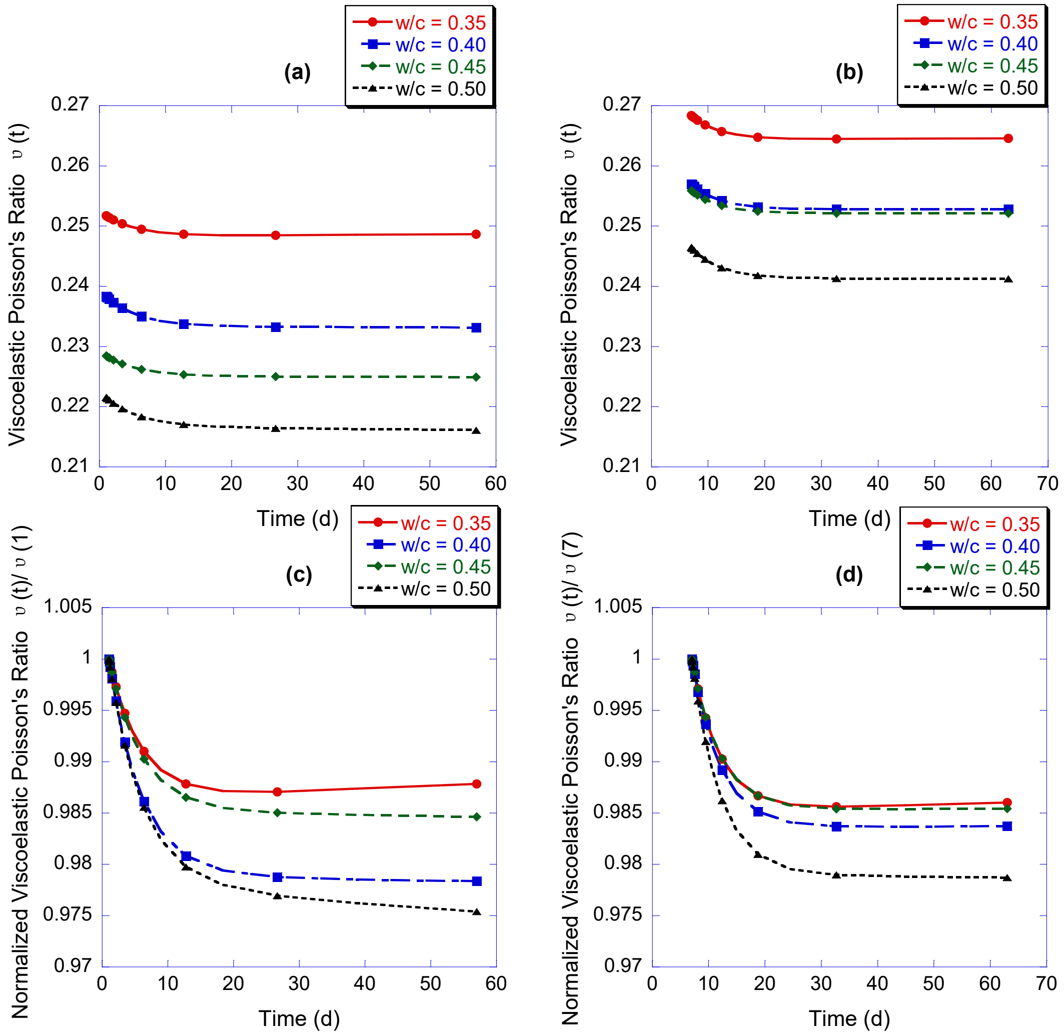

Figure 20 *VE/VP Poisson's ratio for different w/c at loading age of (a) 1 d and (b) 7 d and normalized VE/VP relaxation at loading age of (c) 1 d and (d) 7 d, where VE/VP Poisson's ratio* $\upsilon(t)$ *was normalized by instantaneous elastic Poisson's ratio. VE/VP behavior was considered to occur due to intrinsic C-S-H relaxation while ignoring dissolution effects. The VE/VP Young's modulus of C-S-H was assumed to be* $E(t) = 11.2\ \text{GPa} + 11.2\exp(-0.2t)\ \text{GPa}$ *, and the Poisson's ratio of C-S-H was assumed to have a constant value of 0.25. The elastic properties of all other phases were taken from [22].*

From Figure 19, compared with the apparent VE/VP relaxation caused by cement grain dissolution, the VE/VP bulk and shear moduli relax at much closer rates for different *w/c*, thus leads to Figure 20 that, the values of VE/VP Poisson's ratio induced by intrinsic C-S-H viscoelasticity (whose changes are less than 2.5 %) change very little with time. In the simulations presented in Figure 20, where the VE/VP Poisson's ratio of C-S-H was prescribed to be constant in time, the VE/VP bulk and shear moduli of the C-S-H would necessarily have the same rate of relaxation. However, for most VE/VP solids (e.g., polymers), the shear relaxation is much faster than the dilatational relaxation [81]. For such materials it is common to treat the dilatational behavior as purely elastic and treat the shear behavior as VE/VP. Figure 21 and Figure 22 shows the apparent VE/VP bulk modulus, shear modulus and Poisson's ratio for cement pastes with w/c ranging from 0.35 to 0.50 at loading ages of 1 d and 7 d, where the relaxation was due strictly to the intrinsic VE/VP relaxation of C-S-H, but with the VE/VP bulk modulus of C-S-H prescribed to be a time-independent value of $14.9\ \text{GPa}$ = K(0) when E(0) = 22.4 GPa and ν = 0.25 [14]. The VE/VP shear modulus of C-S-H is prescribed to be $G(t) = 4.5\ \text{GPa} + 4.5\exp(-0.2t)\ \text{GPa}$, allowing 50% of the instantaneous elastic Shear modulus to be relaxed as $t \to \infty$. The value of G(0) = 9.0 GPa is also taken from [14], and is derived from E(0) = 22.4 GPa and ν = 0.25. All other phases in the microstructure were prescribed to be elastic with properties taken from [22].

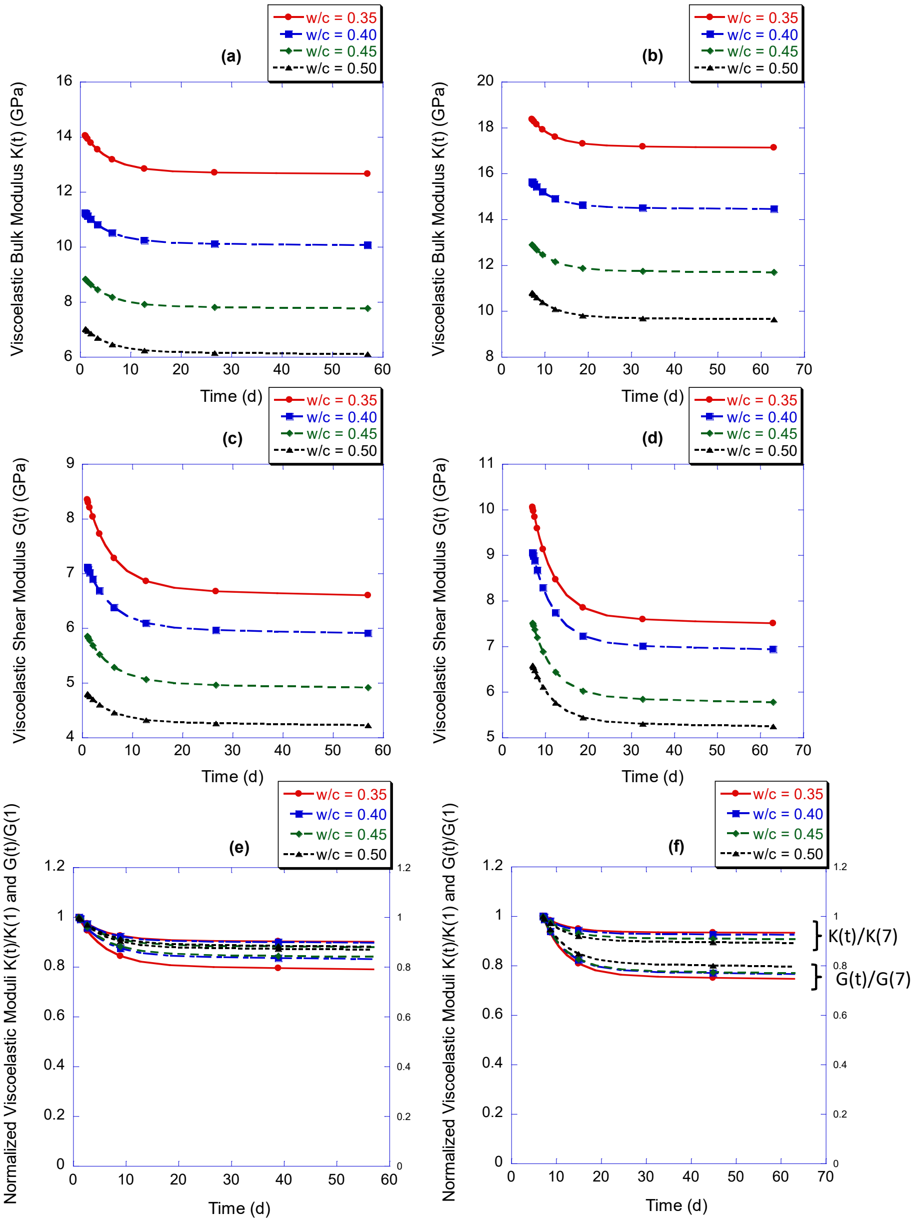

Figure 21 *VE/VP bulk modulus for different w/c at loading age of (a) 1 d and (b) 7 d, VE/VP shear modulus at loading age of (c) 1 d and (d) 7 d, and normalized apparent VE/VP relaxation at loading age of (e) 1 d and (f) 7 d, where the apparent VE/VP bulk modulus K(t) and shear modulus G(t) were normalized by the instantaneous elastic bulk and shear moduli. VE/VP behavior was considered to occur due to intrinsic C-S-H relaxation while ignoring dissolution effects. The VE/VP bulk modulus of C-S-H was prescribed to be a constant value of 14.9 GPa, and the VE/VP shear modulus of C-S-H was prescribed to be* $\mathrm{G}(t) = 4.5\ \mathrm{GPa} + 4.5\exp(-0.2t)\ \mathrm{GPa}$ *, where t is in days. The elastic properties of all other phases were taken from [22].*

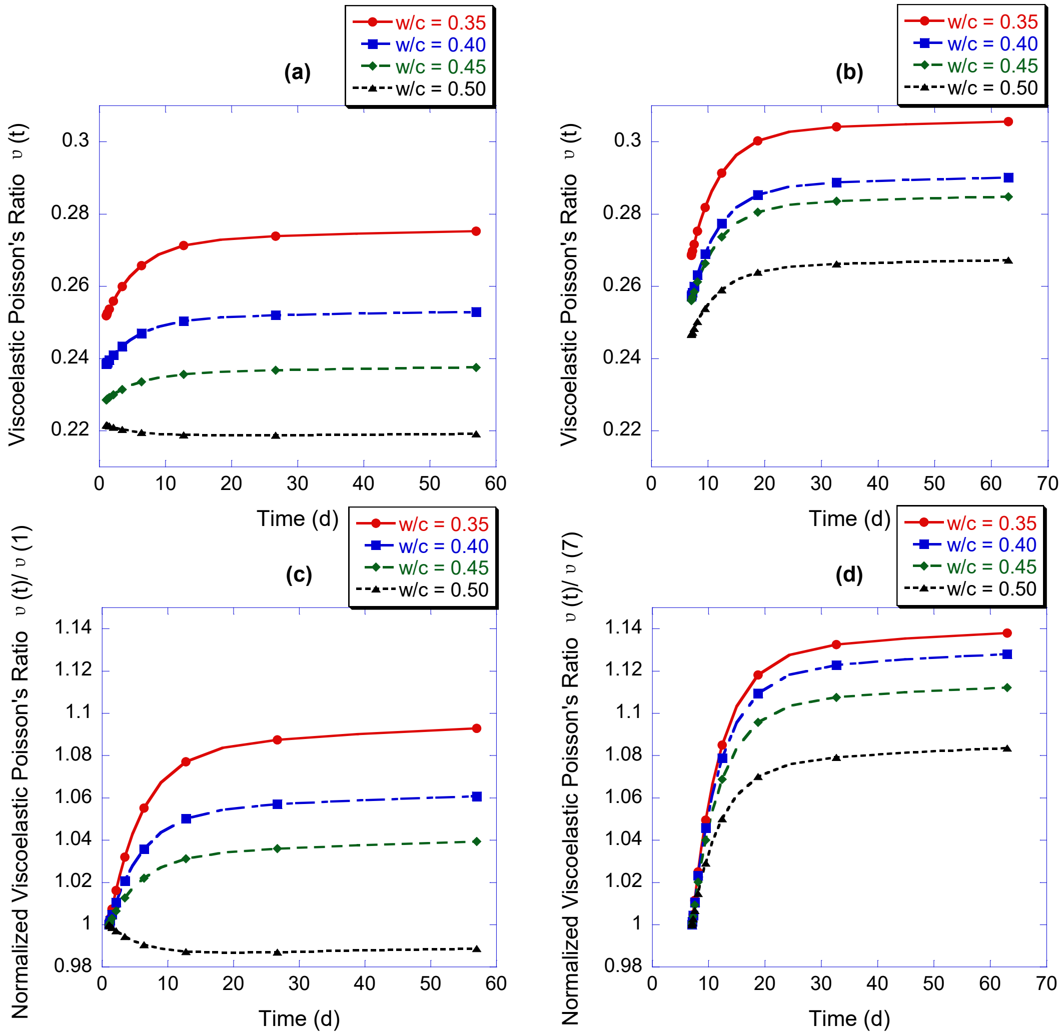

Figure 22 *VE/VP Poisson's ratio for different w/c at loading age of (a) 1 d and (b) 7 d and normalized VE/VP Poisson's ratio at loading age of (c) 1 d and (d) 7 d, where normalizion was by instantaneous elastic Poisson's ratio. VE/VP behavior was considered to occur due to intrinsic C-S-H relaxation while ignoring the dissolution of cement grains. The VE/VP bulk modulus of C-S-H was prescribed to be a constant value of 14.9 GPa, and the VE/VP shear modulus of C-S-H was prescribed to be* $\mathrm{G}(t) = 4.5\ \mathrm{GPa} + 4.5\exp(-0.2t)\ \mathrm{GPa}$ *, where t is in days. The elastic properties of all other phases were taken from [22].*

When assigning different mechanical properties to C-S-H phases, the relaxation rate of the composite VE/VP bulk modulus relative to the composite VE/VP shear modulus changes with time, which then affects the evolution of the composite VE/VP Poisson's ratio with time. In this case, where the VE/VP bulk modulus of C-S-H is kept constant while VE/VP shear modulus decreases with time, the overall VE/VP bulk moduli shows a slower relaxation than VE/VP shear moduli, leading to a time-dependent increase in VE/VP Poisson's ratio. Later loading age leads to a higher overall increase of VE/VP Poisson's ratio as a result of a faster decay in the composite shear modulus relative to the composite bulk modulus; this is because of the higher stress fraction carried by relaxing C-S-H phases at later ages. The differences of the evolution of VE/VP Poisson's ratio between Figure 20 and Figure 22 show that, depending on the different mechanical properties of the VE/VP phases inside the composite material, the overall VE/VP Poisson's ratio is capable of exhibiting increasing, decreasing or even constant time-dependency.

5.2.3 Poisson's Ratio evolution due to simultaneous intrinsic C-S-H relaxation and cement grain dissolution

Figure 23 and Figure 24 compares the simulation results of the apparent VE/VP bulk modulus, shear modulus and Poisson's ratio time evolution occurring due to both intrinsic C-S-H relaxation and dissolution effects versus the apparent VE/VP evolution occurring strictly due to cement grain dissolution. Both simulations are for a cement paste with *w/c* of 0.40 and a loading age of 1 d. When predicting the apparent VE/VP Poisson's ratio caused by both mechanisms, two different sets of virtual experiments were performed by assigning different mechanical properties to the C-S-H phases: in the first virtual experiment, the VE/VP Young's modulus of C-S-H was assumed to be $E(t) = 11.2\ \text{GPa} + 11.2\exp(-0.2t)\ \text{GPa}$, and the Poisson's ratio of C-S-H was set to 0.25, independent of time; in the other virtual experiment, the VE/VP bulk modulus of C-S-H was assumed to have a time-independent value (fixed K) of $14.9\ \text{GPa}$ and, for comparison purposes, the VE/VP shear modulus of C-S-H has the same value of G(0) but was assigned with a larger relaxation value, $\text{G}(t) = 1.125\ \text{GPa} + 7.875\exp(-0.2t)\ \text{GPa}$, than the one utilized in Figure 21 and Figure 22 so as to yield a more observable difference from the first virtual experiment shown in Figure 19 and Figure 20. In both cases, each newly created voxel of C-S-H starts its own viscoelastic properties with the substituting time $t = 0$; that is, at the time when a voxel forms, it is stipulated that $E(t = 0)$ or $G(t = 0)$ for that voxel, with relaxation of that voxel proceeding at subsequent times. All other phases in the microstructure were assigned to be elastic with properties taken from [22]. When generating the apparent VE/VP Poisson's ratio due only to cement grain dissolution, cement paste microstructures were utilized with purely elastic phases, also with elastic properties taken from [22].

One can see from Figure 23 and Figure 24 that the dissolution of cement grains dominates the evolution of the value of the apparent VE/VP bulk modulus, shear modulus, and Poisson's ratio of cement paste at early ages, up to about 5 d, leading to decreasing VE/VP Poisson's ratio values. This result lies in the fact that the inherent strain redistribution rate associated with the hydration rate significantly affects the apparent VE/VP Poisson's ratio; the rapid hydration rate at early age of cement paste leads to high relaxation rate of apparent VE/VP Poisson's ratio. As cement paste ages, the effect of cement grain dissolution on the overall apparent VE/VP Poisson's ratio relaxation decreases with decreasing hydration rate, while on the other hand, the apparent VE/VP Poisson's ratio evolution caused by C-S-H relaxation increases with age due to the increasing amount of C-S-H. One thing to notice is that, depending on the

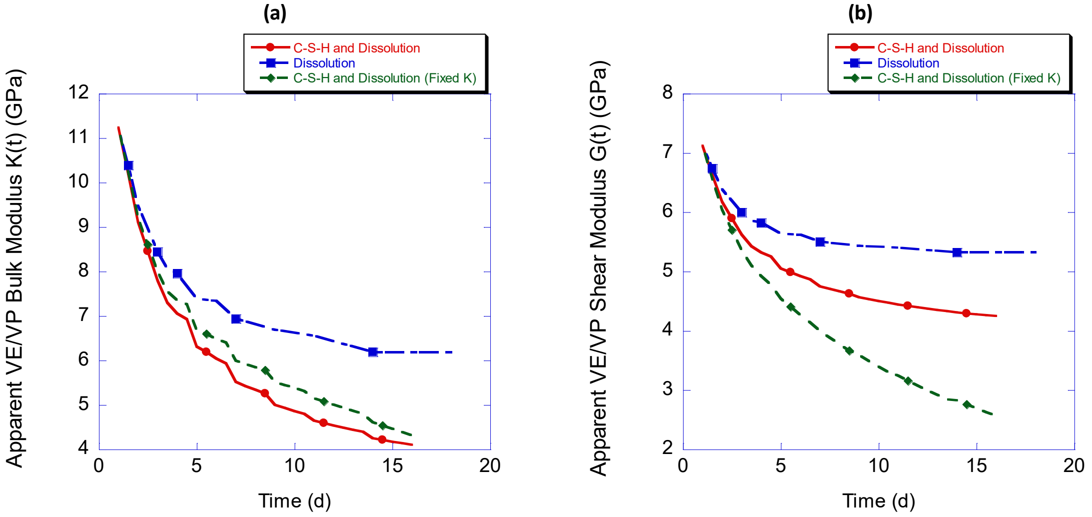

Figure 23 *Comparison of apparent VE/VP (a) bulk and (b) shear moduli where VE/VP effects due to both C-S-H viscoelasticity and cement grain dissolution are considered and where dissolution only is considered for a cement paste with w/c of 0.40 at loading age of 1 d. For the "C-S-H and Dissolution" simulation, the VE/VP Young's modulus of C-S-H was assumed to be* $E(t) = 11.2 \text{ GPa} + 11.2\exp(-0.2t) \text{ GPa}$*, and the Poisson's ratio of C-S-H was assumed to be a constant value of 0.25. For the simulation with fixed K, the VE/VP shear modulus of C-S-H was assumed to be* $G(t) = 1.125 \text{ GPa} + 7.875\exp(-0.2t) \text{ GPa}$ *and the bulk modulus of C-S-H was assumed to have a constant value of 14.9 GPa. For the "Dissolution" imulation C-S-H was assumed to be elastic. The elastic properties of C-S-H and all other phases were taken from [22].*

different mechanical properties of C-S-H (as well as different *w/c* and loading ages of cement paste), later-age cement paste, the behavior of which is dominated by intrinsic C-S-H relaxation, can exhibit increasing (short dashed line in Figure 24), decreasing (long dashed line in Figure 24) or constant VE/VP Poisson's ratio. It is clear

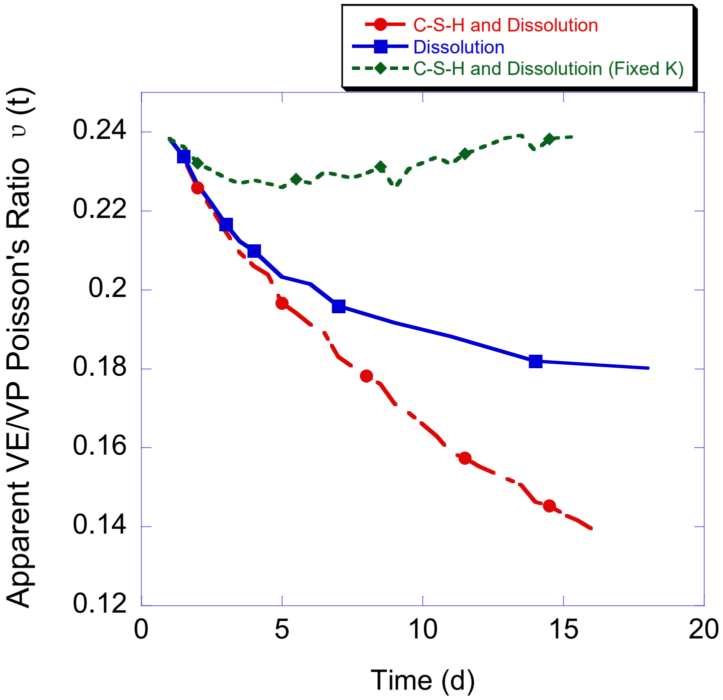

Figure 24 *Comparison of apparent VE/VP Poisson's ratio where VE/VP effects due to both C-S-H viscoelasticity and cement grain dissolution are considered and where dissolution only is considered for a cement paste with w/c of 0.40 at loading age of 1 d. For the "C-S-H and Dissolution" simulation, the VE/VP Young's modulus of C-S-H was assumed to be* $E(t) = 11.2\ \mathrm{GPa} + 11.2\exp(-0.2t)\ \mathrm{GPa}$ *, and the Poisson's ratio of C-S-H was assumed to be a constant value of 0.25. For the simulation with fixed K, the VE/VP shear modulus of C-S-H was assumed to be* $G(t) = 1.125\ \mathrm{GPa} + 7.875\exp(-0.2t)\ \mathrm{GPa}$ *and the bulk modulus of C-S-H was assumed to have a constant value of 14.9 GPa. For the "Dissolution" simulation C-S-H was assumed to be elastic. The elastic properties of C-S-H and all other phases were taken from [22].*

that dissolution effects govern the apparent VE/VP Poisson's ratio evolution at early ages, leading to decreasing VE/VP Poisson's ratio, while intrinsic C-S-H viscoelasticity determines the apparent VE/VP Poisson's ratio evolution at later ages. At a later age of 7 d, one would expect less influence from the cement grain dissolution, but more from intrinsic C-S-H aging, and thus a more likely increasing trend of the evolution of Poisson's ratio under fixed bulk modulus. Thus, the simulation results indicate that there may not be a consistent trend (e.g., increasing, decreasing, or constant) with respect to the VE/VP Poisson's ratio of cement paste. Since the properties of C-S-H in the virtual experiments are assumed values, further experimental inquiry is required to accurately characterize the three-dimensional relaxation nature of C-S-H, which can be input into the prediction model to generate more reliable results. Furthermore, we emphasize that poromechanical effects have been ignored in these simulations to elucidate the relative significance of relaxation due to dissolution/re-precipitation compared to intrinsic VE/VP deformation of C-S-H. However, for cement paste saturated with a relative low compliance fluid (e.g., water) , the poromechanical effect would tend to cause a time-dependent decrease in the VE/VP Poisson's ratio because fluid flow in the pore network results in a time-dependent reduction in the dilatational stiffness without affecting the deviatoric stiffness. Time-dependent, stress-induced dissolution of hydrates in cementitious materials might also induce apparent viscoelastic effects [82], but at this time it is unclear what influence such dissolution might have on the results presented.

From literatures, the differences between Poisson's ratio obtained from the traditional time domain calculation (with the most common form as shown in Eq. (34))

and from the inverse of Laplace transform in creep and relaxation is minor unless under large relaxation strength [75]. Figure 25 shows the relative differences between the two

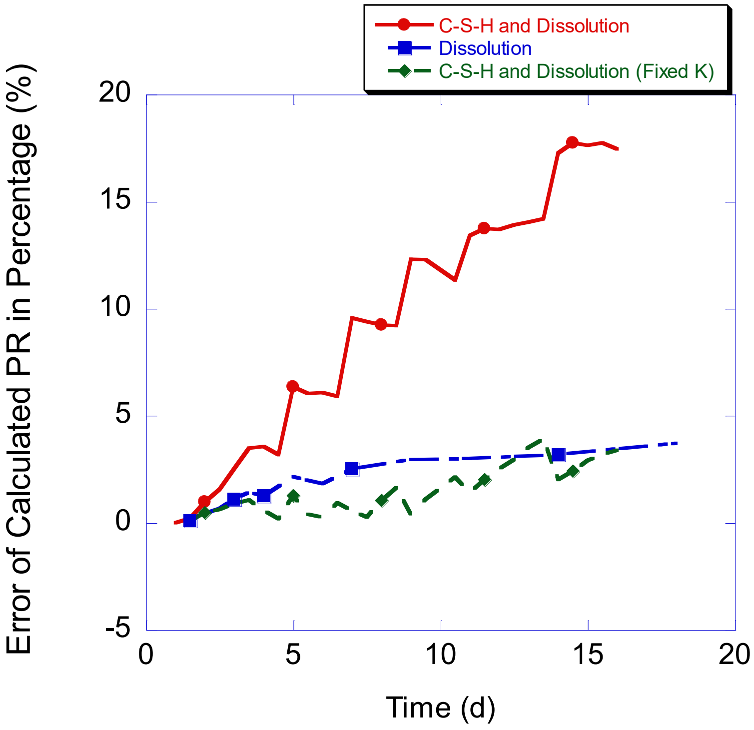

Figure 25 *The error of calculated VE/VP Poisson's ratio obtained with the traditional calculation in time domain relative to the accurate value of VE/VP Poisson's ratio obtained from the inverse of the Laplace transform. The apparent VE/VP effects occur under the same situations as in Figure 23 and Figure 24, and thus utilizing the same raw data (time evolution of bulk and shear moduli) with Figure 23 and Figure 24.*

calculation methods utilizing the same raw simulation data as in Figure 23 and Figure 24. From the raw data of the time evolution of bulk and shear moduli, the accurate VE/VP Poisson's ratio were obtained in frequency domain with inverse Laplace transformation, while the traditional Poisson’s ratio calculation utilize the apparent VE/VP bulk and shear moduli directly in time domain. From Figure 25, the error of classical Poisson’s ratio calculation increases with time, and can reach up to over 15%. Thus, the differences between the calculated results from the two methods for cementitious materials are substantial, and correct definition and calculation of VE/VP Poisson’s ratio is necessary.

5.3 Summary

The time-dependent changes in the apparent VE/VP Poisson’s ratio of cement paste are likely controlled by dissolution of cement grains at early ages due to the high early-age hydration rate. The dissolution of cement grains result in a predicted decreasing VE/VP Poisson’s ratio at early ages. Simulation results also indicate that with the increasing volume fraction of C-S-H inside cement paste as hydration progresses, the influence of intrinsic C-S-H relaxation on apparent VE/VP Poisson’s ratio of cement paste increases. Depending on the mechanical properties of C-S-H as well as *w/c* and the loading age of cement paste, later-age cement paste is capable of exhibiting increasing, decreasing, or constant VE/VP Poisson’s ratio evolution with time.

6. EARLY AGE DESICCATION SHRINKAGE CAUSED BY BOTH INTRINSIC C-S-H CREEP AND CEMENT GRAIN DISSOLUTION[*]

In order to illustrate the robustness and breadth of applicability of the computationally implemented modeling approach, the early age desiccation shrinkage occurring in cement paste during drying process is analyzed in this chapter. Under the effect of the two mechanisms (C-S-H creep/relaxation and cement grain dissolution), the desiccation shrinkage of cement paste shows irreversibility at early ages. [83]

6.1 Background of desiccation shrinkage

Desiccation shrinkage, defined as the time-dependent deformation due to loss of pore water, is a characteristic behavior of cementitious materials. Such shrinkage can be induced by external drying (e.g., through moisture diffusion and evaporation) or internal drying (e.g., when capillary pore water is consumed during hydration or other chemical reactions) (see e.g., [1, 10, 84]). The origin of desiccation shrinkage at high relative humidity (RH) has been primarily attributed to a reduction in the pore fluid pressure that results in corresponding compression of the surrounding solid microstructure [85-89]. The mechanical response to this compression is experimentally measured as desiccation shrinkage. An important observation is that shrinkage continues even under constant *RH* (and thus constant pore fluid pressure), resulting in an irreversible component of deformation and a creep-like behavior of cement paste desiccation shrinkage [90].

---

[*] Reprinted with permission from “Irreversible desiccation shrinkage of cement paste caused by cement grain dissolution and hydrate precipitation” by X. Li, Z.C. Grasley, E.J. Garboczi and J.W. Bullard, 2016. Materials and structures, 50, 104. 2017 by Springer.

Despite devoted efforts to investigate the mechanisms behind shrinkage, no unified theory has been derived to explain the creep and irreversible components of desiccation shrinkage. It is generally believed that microstructural and chemical changes are the origin of these irreversible deformations, and many theories regarding these changes have been proposed, such as the formation of bonds between pressed surfaces [85], further formation of hydration products [91], creation of new interlayer space [89] and dissolution of adsorbent molecules [92]. The major components that are generally attributed as responsible for the irreversible strains are the amorphous calcium silicate hydrate (C-S-H) [1, 93, 94] and distributed pores inside cement paste [93, 95]. A change in the internal *RH* can lead to an alteration in the internal structure of the C-S-H gel, manifesting as a drying-accelerated “aging” process of the C-S-H, potentially leading to an irreversible component of deformation. Besides the mechanisms that are directly related to these fundamental microstructure changes, internal microcracking in cement paste is another potential mechanism of irreversible desiccation shrinkage [1].

According to the simulation results from this newly developed computational scheme, when the microstructure is under external loading, dissolution of solid load-bearing constituents is a significant mechanism leading to irreversible, time-dependent deformation. As an analogous state of stress inside cementitious composites may be incurred through internal pore fluid pressure changes, it is hypothesized that a portion of early-age, irreversible desiccation shrinkage is associated with the dissolution of cement grains during the hydration process. Therefore, the desiccation shrinkage behavior of cement paste is analyzed utilizing this program to get new insights into the mechanisms behind irreversible desiccation shrinkage.

6.2 Shrinkage prediction implementation

The current version of the computational scheme has an important limitation in that the microstructures in the model can only be subjected to strain-controlled periodic boundary conditions. To predict the time-evolving desiccation shrinkage strain of the macroscopic cement paste composite, which is normally measured under zero external stress (e.g., traction free boundaries) and negative internal pore fluid pressure, Boltzmann's superposition principle [55, 56] was used. Figure 26 shows the flow chart for calculating the overall shrinkage strain of cement paste utilizing the computational program and the superposition principle.

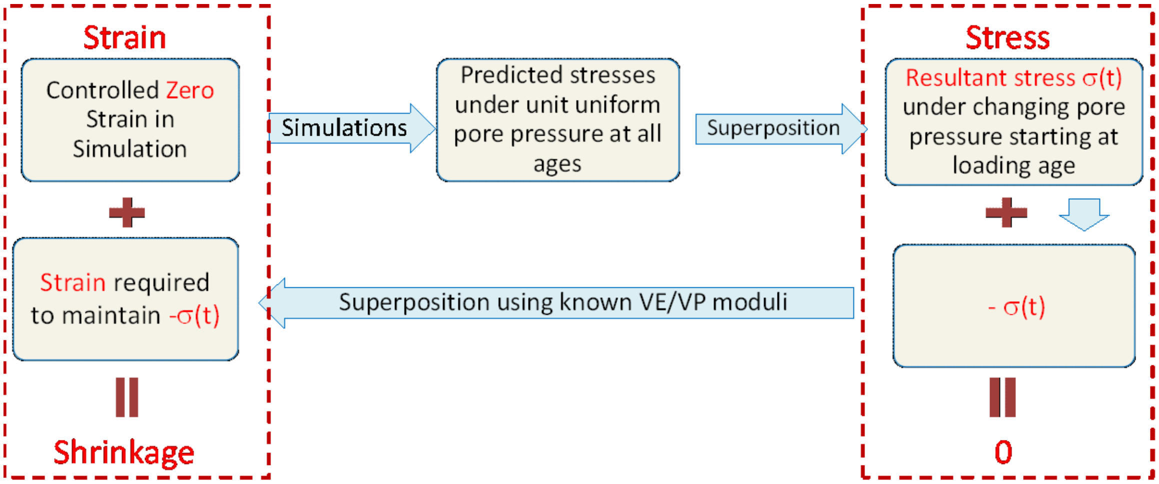

Figure 26 *Flow chart for shrinkage strain calculation under strain-controlled boundary conditions.*

To simulate experiments of desiccation shrinkage measurement and to predict the evolution of the magnitude of shrinkage strain with time, four major steps were conducted in the virtual, computational experiment. First, time was discretized into n different time steps, with each time step representing one particular age. For the preliminary simulations, a stepwise negative pore pressure $H(t)p_0$ (where $H(t)$ is the Heaviside function) and zero external periodic boundary strain were applied on a list of microstructures that were generated by THAMES for all drying ages t_1, t_2, $t_3 \ldots\ldots t_n$ (which means that pore pressure was applied on cement paste starting at time t_1, t_2, $t_3 \ldots\ldots t_n$ and each time t_i is the age represented by time step i). The negative pore pressure was applied to the fluid phases of the simulated microstructures for the purpose of simulating the drying process, and the evolution of the stress fields of the whole composite as a result of the assigned pore fluid pressure were predicted by the computational program.

The spatially averaged hydrostatic stress of the composite as a function of time for different drying ages was calculated from the simulation results. The hydrostatic stress of the composite per unit uniform pore pressure was determined as

$$\sigma_{t_m}^{unit}(t_i) = \sigma_{t_m}^{p_0}(t_i) / p_0 , \tag{37}$$

where $\sigma_{t_m}^{unit}(t_i)$ is the value of the hydrostatic stress at time t_i per unit pore pressure when dried at age t_m, $\sigma_{t_m}^{p_0}(t_i)$ is the hydrostatic stress at time t_i under pore pressure p_0 when dried at age t_m, $m = 1,2,3...n$ and $i = 1,2,3...n$. The resultant hydrostatic stress history of the composite under any given internal pore pressure history, $p(t)$, may be determined according to

$$\sigma(t_i) = \sum_{k=m}^{i} \{\sigma_{t_k}^{unit}(t_i)[p(t_k) - p(t_{k-1})]\}, \tag{38}$$

where $\sigma(t_i)$ is the hydrostatic stress of the composite at time t_i under the given pore pressure history.

The desiccation shrinkage strain was calculated utilizing the hydrostatic stress history of the composite from eq. (38) and the evolving VE/VP properties of the composite simulated using the computationally implemented model as described in Ref. [23, 67]. In order to perform the shrinkage calculation, it was necessary to apply a virtual boundary hydrostatic stress history of $-\sigma(t_i)$ to maintain an overall spatially averaged zero stress state (corresponding to "free shrinkage"), as shown in Figure 26. Then the strain history that must necessarily be applied at each time step to achieve $-\sigma(t_i)$ was calculated according to the superposition principle via

$$\begin{aligned} &\text{if } i = 1,\ \varepsilon(t_i) = \frac{-\sigma(t_i)}{3K_{t_i}(t_i)}; \\ &\text{if } i \neq 1,\ \varepsilon(t_i) = \frac{-\sigma(t_i) - \sum_{k=1}^{i-1}[\varepsilon(t_k)K_{t_k}(t_i)]}{3K_{t_i}(t_i)}, \end{aligned} \tag{39}$$

where $\varepsilon(t_i)$ is the additional linear strain to be applied on the composite at time t_i to achieve the desired boundary stress history, and $K_{t_k}(t_i)$ is the apparent VE/VP bulk modulus (i.e., computed from the model in Ref [23, 67])of the composite at time t_i when loaded at age t_k . The resultant linear shrinkage strain, $\varepsilon_{shrinkage}(t_i)$, of the composite is calculated as

$$\varepsilon_{shrinkage}(t_i) = \sum_{k=1}^{i} \varepsilon(t_k) , \tag{40}$$

In this way, the predicted time-evolution of the shrinkage strain is due to the concomitant elastic deformation of the solid microstructure with changes in pore fluid pressure as well as the dissolution of cement grains and subsequent stress redistributions in the microstructure. Although eq. (37) through eq. (40) were intended for calculating the time-evolved shrinkage strain of cement paste during the drying process, if a specimen is exposed to re-wetting and the internal *RH* of the simulated cement paste increases as a function of time, then the time-dependent swelling strain of cement paste may be predicted following the same procedures, except that the final results obtained would have an opposite sign, denoting negative shrinkage (i.e., expansion). The ability to simulate re-wetting allows direct evaluation of reversibility and irreversibility of the simulated desiccation shrinkage.

6.3 Simulation results & discussions

Microstructures of hydrating cement composites at different ages (from 1 d to 56 d) were examined in this research project to predict the time-dependent shrinkage of cement pastes. Unless stated otherwise, all the phases inside cement pastes were approximated to be linearly elastic with elastic properties taken from [22]. Using the power of the model to examine only one deformation mechanism at a time, the irreversible shrinkage occurs strictly due to the time-dependent dissolution of load-bearing cement grains.

6.3.1 Different ages of drying

Once the desiccation process starts inside cement paste, negative pore fluid pressure is induced in the pores of the cement paste composite. When the pore fluid pressure was simulated as a step function, the instantaneous application of pore pressure resulted in instantaneous reversible elastic shrinkage. All of the time-dependent increases in shrinkage strain after the instantaneous application of the pore pressure were irreversible and associated with cement grain dissolution. Figure 27 shows the predicted irreversible shrinkage strain normalized by the applied pore pressure for a 0.40 *w/c* cement paste at ages of 1 d and 4 d. From Figure 27, cement pastes continue to shrink under constant pore pressure, leading to substantial irreversible shrinkage due to cement grain dissolution. Meanwhile, under the constant pore fluid pressure, younger specimens exhibit greater irreversible shrinkage and faster shrinkage rate because of the higher hydration rate (and thus higher dissolution rate of cement grains) at early ages. Another reason leading to the faster shrinkage in younger specimens is that, when specimens are younger, more water is present inside cement paste, resulting in a greater overall contraction of the solid skeleton because the pore fluid pressure is exerted within a greater fraction of the composite volume. Additionally, the younger cement paste composite is less stiff than an older specimen, and thus is more compliant to external and internal forces, resulting in an overall larger deformation. In conclusion, from the simulation results, younger cement paste specimens are more likely to exhibit greater irreversible shrinkage from cement grain dissolution than older cement pastes, which agrees with the experimental data presented in Ref. [23, 67].

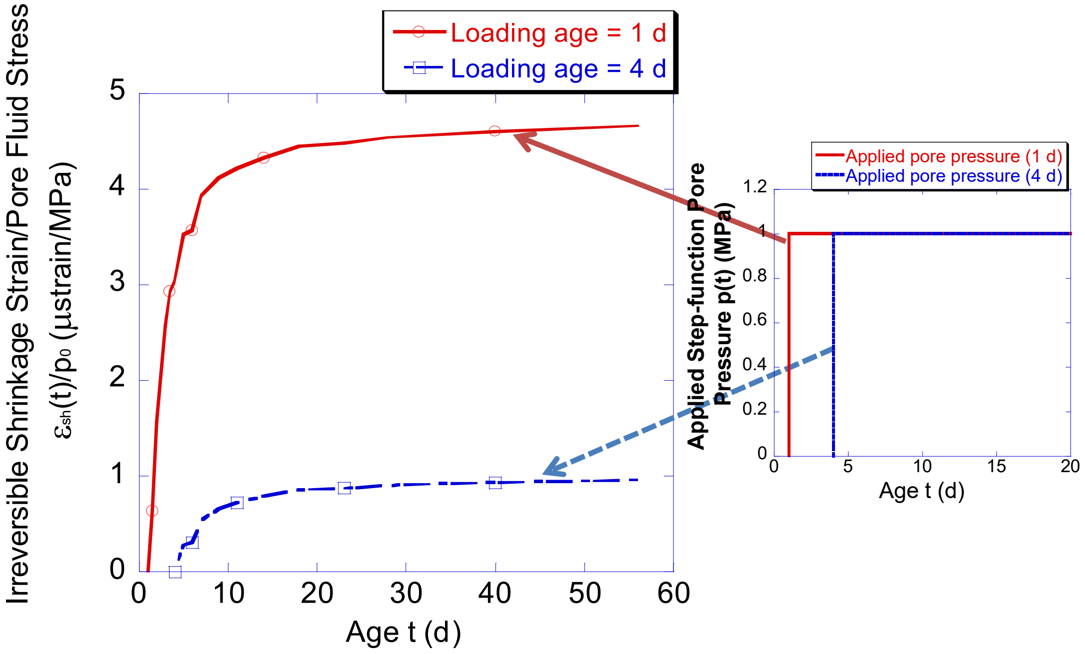

Figure 27 *Irreversible shrinkage strain normalized by the applied pore fluid pressure in a 0.40 w/c cement paste when dried at different ages (1 d and 4 d). In this graph, irreversible shrinkage strain was considered to increase strictly due to the dissolution of load-bearing cement grains.*

6.3.2 Different w/c

Figure 28 shows the predicted irreversible shrinkage strain divided by the step-applied pore fluid pressure for cement pastes with different *w/c* from 0.35 to 0.50 with drying initiating at 1 d. At early ages, higher *w/c* leads to faster shrinkage rate and greater shrinkage magnitude than lower *w/c* due to its higher water content and lower stiffness. The shrinkage rate of cement pastes for all *w/c* decreases with age.

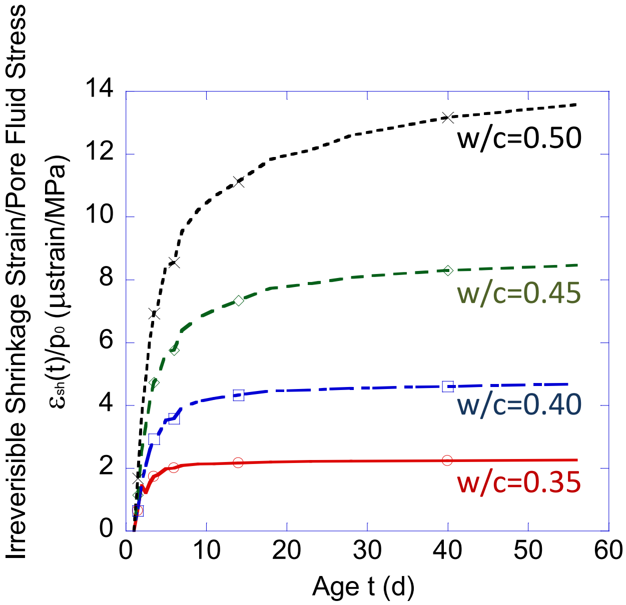

Figure 28 *Irreversible shrinkage strain normalized by the applied pore fluid pressure for different w/c at a drying age of 1 d. The irreversible shrinkage strain was considered to increase strictly due to dissolution of load-bearing cement grains.*

6.3.3 Time-evolving RH

In the previous simulations (i.e., Figure 27 and Figure 28), the pore fluid pressures were all assigned as step-functions, while in reality, the pore fluid pressure approximately changes with age as a function of the time-evolving internal *RH* through the combined Kelvin-Laplace equation

$$p \approx -\ln\left(\frac{RH}{RH_0}\right)\frac{RT}{v_w}, \tag{41}$$

where p is the pore fluid pore pressure, RH is the current internal relative humidity, RH_0 is the reference configuration internal relative humidity[3], R is the universal gas constant, v_w is the molar volume of water, and T is the temperature in Kelvin [96]. Here, the time-evolution of the effect of the dissolved species on the chemical potential of the pore fluid is neglected; a modified version of eq. (41) should be used if one wishes to simulate evolving chemistry of the pore solution during desiccation [97]. With the experimental data of the time-evolving *RH*, the pore fluid pressure inside the cement paste composite can be calculated and implemented into the computational scheme to simulate realistic shrinkage behavior of cement paste.

Figure 29 shows the predicted results of the time-dependent shrinkage strain of 0.40 *w/c* cement paste utilizing experimental data of time-evolving *RH* at the drying age of 1 d under constant temperature of 273 K. The experimental internal *RH* data [98] were obtained by embedding a small sensor in a self-desiccating (sealed from external drying) mortar bar[4]. One thing to note is that, in reality, the rate of hydration reaction has a close relationship with the internal *RH* of cement paste. At low to intermediate *RH*, the

---

[3] The initial RH (i.e., prior to any desiccation) in cement-based materials is suppressed by the reduction in water activity caused by the presence of dissolved species in the pore fluid. Such effects can be accounted for, whereby the dissolved species and their concentrations are explicitly accounted for in a modified version of eq. (41). An alternative approach is taken here whereby one defines RH_0 not as $RH = 100\%$ (i.e., the RH that is measured over a flat surface of pure water), but rather as the relative humidity above a flat surface of the pore solution as it exists prior to any desiccation. The latter approach is taken here, using experimental data from the literature.

[4] Since the referenced experiments only involved mortars rather than pastes and since the cement utilized in the specimens was not characterized to the extent necessary to utilize THAMES to simulate the microstructure evolution, it was not deemed useful to compare the actual measured autogenous shrinkage of the mortar bar with simulated autogenous shrinkage of the paste. The *RH* history was simply utilized to represent a “typical” history for simulation purposes.

hydration reaction significantly slows down or even stops, while at high *RH*, the *RH* magnitude has little effect on the hydration kinetics [99]. Since the simulations presented were all conducted under relatively high *RH* conditions (with *RH* > 80%), it was assumed, for simplification, that the hydration rate was independent of the internal *RH*.

In Figure 29, besides the time-evolving measured *RH* history on the right hand Y axis, which leads to time-evolving pore fluid pressure, three different sets of predicted shrinkage strain history are included. The solid line and the dashed shrinkage strain line with square markers were obtained from the computationally predicted data. The solid line considered the microstructure-evolving properties of cement paste at all ages; it shows the increase of the shrinkage strain as a combination of both the elastic response to increasing internal pore fluid pressure as well as the dissolution effect of the load bearing cement grains. The dashed line with square markers considered the cement paste composite at each time step as a purely elastic material with constant mechanical moduli independent of microstructures from other ages; it simply shows the change of the cement paste shrinkage strain from the elastic response to the pore fluid pressure increase while neglecting the phase dissolution effects. The shrinkage demonstrated by the dashed line with square markers is simply a result of the elastic deformation of cement paste, and the differences between this line and the solid line are the predicted irreversible shrinkage induced by cement grain dissolution.

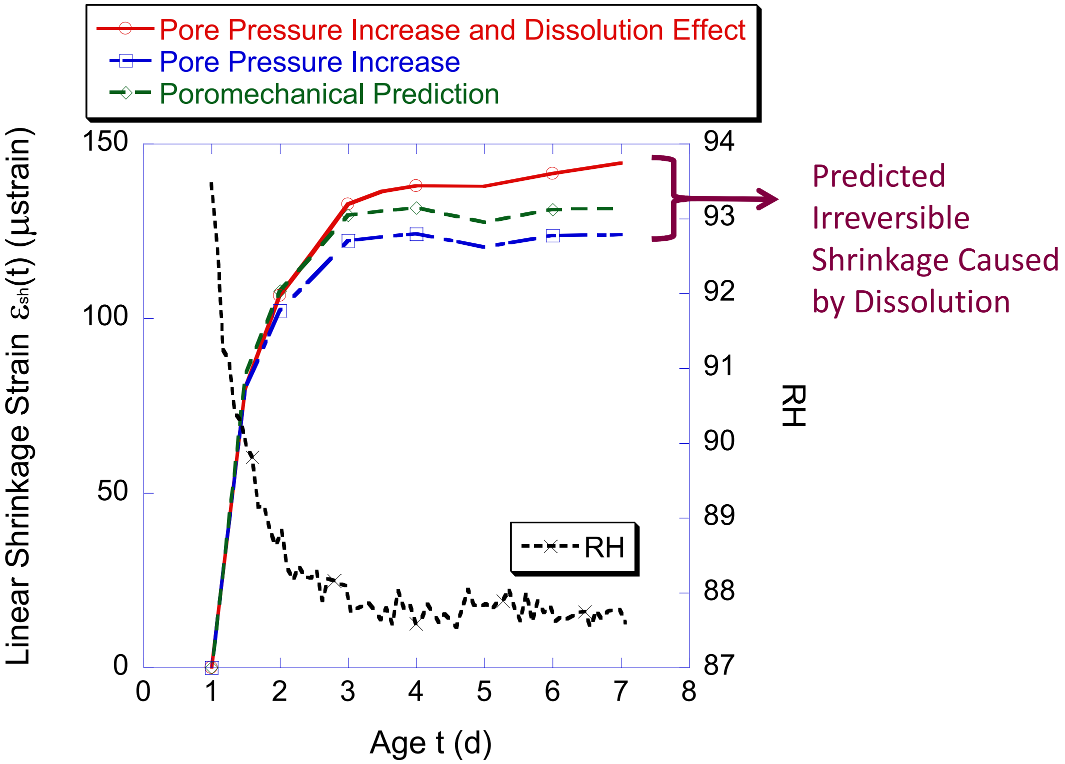

Figure 29 *Predicted shrinkage strain of 0.40 w/c cement paste with drying initiated at age of 1 d. In this graph, the computationally predicted data is shown (i) by treating cement paste at all ages as a microstructure-dependent time-evolving material (solid line), which shows the overall shrinkage due to both pore pressure increase and cement grain dissolution effects; (ii) by treating cement paste as purely elastic while neglecting phase dissolution effects (dashed shrinkage line with square markers), which shows the shrinkage of cement paste occurring purely due to instantaneous elastic deformation; and (iii) by poroelasticity (dashed shrinkage line with diamond markers). The RH history (dotted line with cross markers) was also included in this graph on the right hand Y axis. Due to the irregularity of the real life RH data, the RH history curve is not smooth, while the computational scheme utilizes microstructures of cement paste at certain limited number of discrete ages, the predicted shrinkage curves are more smooth.*

Among analytical models for predicting the desiccation shrinkage of cementitious materials, from a mechanics perspective, poroelasticity has been used to predict the elastic, recoverable shrinkage of cement paste [10, 90, 100, 101] according to

$$d\varepsilon_{sh}(t) = \frac{S(t)dp(t)}{3}\left(\frac{1}{K_p(t)} - \frac{1}{K_s}\right), \tag{42}$$

where t denotes time, $\varepsilon_{\mathrm{sh}}(t)$ is the time-dependent function of linear shrinkage strain, $S(t)$ is the function of saturation coefficient (fraction of pores filled with liquid pore solution), $dp(t)$ is the differential of pore fluid pressure, $K_p(t)$ is the time-dependent function of bulk modulus of the drained porous medium and K_s is the bulk modulus of the solid skeleton, which can be considered as constant. Comparison between the computationally predicted recoverable shrinkage and the poroelastic shrinkage would be carried out.

The dashed shrinkage line with diamond markers in Figure 29 was obtained from the poroelastic calculation results utilizing a discretized form of eq. (42) in the computational model,

$$\varepsilon_{sh}(t_i) = \sum_{i=1}^{n} \frac{S(t_i)\Delta p(t_i)}{3}\left(\frac{1}{K_p(t_i)} - \frac{1}{K_s}\right) \tag{43}$$

where $\Delta p(t_i) = p(t_i) - p(t_{i-1})$, denoting the pore pressure difference between two different time steps. The shrinkage predicted by poroelasticity follows the same trend as the predicted elastic recoverable shrinkage (the dashed line with square markers). One potential reason to explain the differences between the two dashed shrinkage prediction lines is that, for a partially saturated porous material, poroelasticity has significant drawbacks, and its accuracy highly depends on the microstructure (pore size distribution) of the material [100]. From the comparison between the solid shrinkage line and the two dashed shrinkage lines, the dissolution of load-bearing cement grains during the shrinkage process appears to be a significant mechanism leading to irreversible shrinkage. Poroelasticity underestimates desiccation shrinkage, as has been noted previously [10, 90]. However, while Lura et al. [90] and Grasley and Leung [10] suggested that inherent viscoelasticity or creep of the cement paste phases might account for the under-prediction, here we suggest that dissolution of cement grains plays a role in such under-prediction at early ages. As cement paste ages during drying, the difference between the poroelastic calculation and the overall computational prediction (including both dissolution effect and pore pressure change) increases, as can be noted in Figure 29.

6.3.4 Recovering RH

Using the same *RH* data as used in Figure 29 but forcing *RH* to return back to its initial value after 6 (Figure 30a) and 7.5 days (Figure 30b) of drying, the results shown in Figure 30 can be obtained for drying initiating at 1 d and 3.5 d. Microstructures of 0.40 *w/c* cement paste were used in the simulations, and the temperature was kept constant at 273 K. In both Figure 30(a) and (b), the *RH* histories were included on the right hand Y axis. The solid shrinkage lines show the overall shrinkage due to both pore pressure change and cement grain dissolution effects, and the dashed shrinkage lines show the predicted shrinkage of cement paste occurring purely due to pore pressure change. In both figures, cement paste shrinks with decreasing *RH* and swells with recovering *RH*. After *RH* returns back to its initial value, the irreversible shrinkage strains caused by the dissolution effect could be predicted by the differences between the solid lines and the dashed lines. Comparing to Figure 30(b), Figure 30(a) shows the shrinkage strain history of cement paste when drying initiated at an earlier age, and it can be seen that, when dried at earlier ages, a much larger irreversible shrinkage would be observed due to the more active hydration reaction at earlier ages (and thus higher dissolution rate of cement grains). These results suggest that steps to increase the degree of hydration prior to drying initiation (e.g., wet curing and heat curing) would reduce the irreversible component of desiccation shrinkage. Note that countering the effect of increased degree of hydration on reducing irreversible shrinkage is the additional shrinkage that may occur as a result of the refined pore structure associated with wet curing [102].

In the model simulations, after the *RH* returns back to its initial value or pore pressure returns back to zero, a residual shrinkage exists as a result of the increasing stiffness in the cement paste. At earlier ages, cement paste shrinks as pore pressure increases, while at later ages, when pore pressure returns back to zero, cement paste would not swell as much because of the increased stiffness, leaving a residual shrinkage value shown in Figure 30.

6.3.5 Cyclic drying and rewetting

In Figure 31, a cyclic drying and rewetting process was applied on 0.45 w/c cement

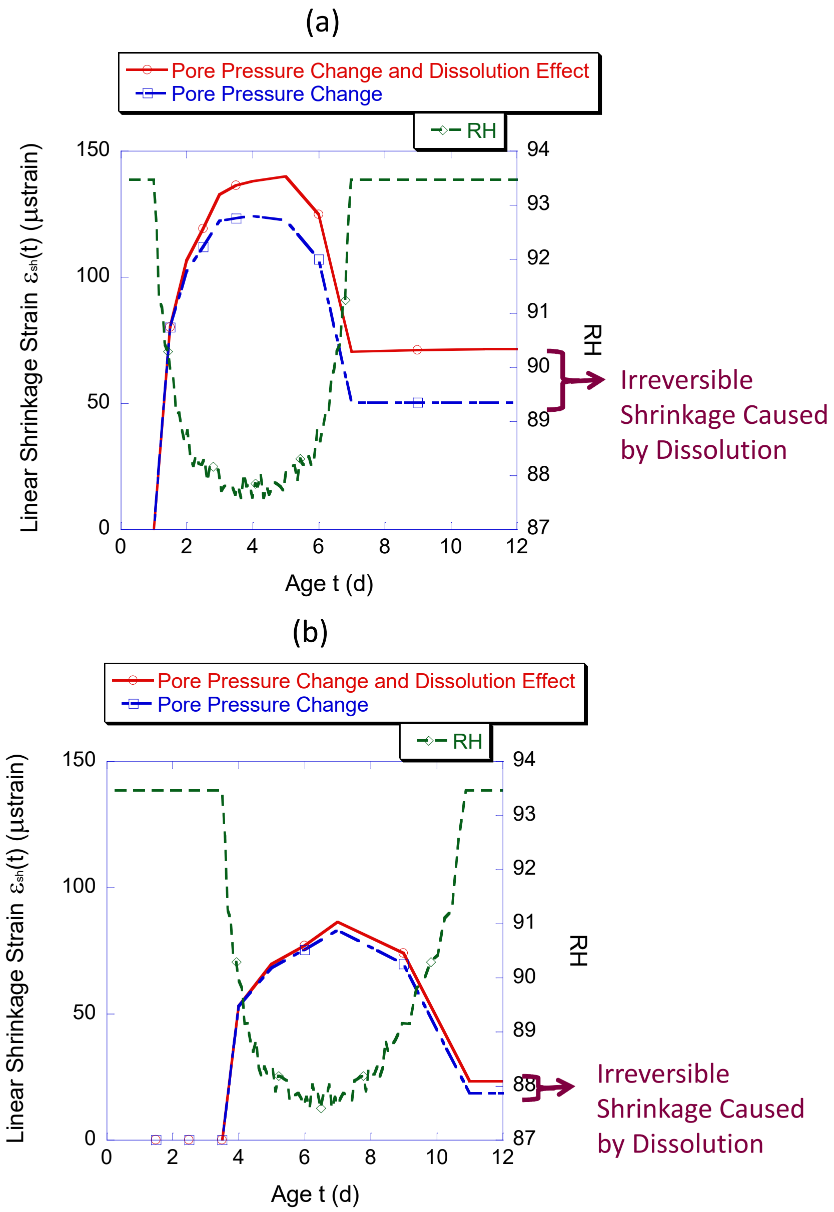

Figure 30 *Predicted shrinkage strain of 0.40 w/c cement paste with drying initiated at ages of (a) 1 d and (b) 3.5 d. In both graphs, the solid lines show the overall shrinkage due to both pore pressure change and cement grain dissolution effects, while the dashed shrinkage lines show the recoverable shrinkage of cement paste occurring purely due to pore pressure change. Internal RH history was also included in this graph on the right hand Y axis.*

paste at different ages of drying initiation of 1 d and 2 d. The *RH* history applied in Figure 31 follows the function

$$RH(t) = 100 - 10[1 - \cos(2\pi \cdot f \cdot t)](\%), \qquad (44)$$

where $RH(t)$ is the internal *RH* history as a function of time, t represents the time in days after the start of drying, and f denotes the frequency of the cyclic drying and rewetting. In this way, *RH* becomes a sinusoidal function oscillating between 100% and 80% with each cycle period equal to $1/f$ in days (d). According to eq. (41) and eq. (44), the internal pore pressure also becomes a sinusoidal function starting from zero pore fluid stress and oscillates with the frequency of f. According to the simulated shrinkage strain shown in Figure 31, which includes both the elastic deformation of cement paste due to pore pressure changes and cement grain dissolution effects, the irreversible strain increases with age under cyclic drying and rewetting and can be directly observed at the time when pore pressure returns back to zero, revealed in Figure 31 as the strains at the bottoms of the oscillating curves. As discussed in the previous sections, younger specimens would yield a larger ultimate irreversible shrinkage, and the simulated maximum strain under maximum pore pressure per drying cycle decreases with age as a result of increasing stiffness of the cement paste. The irreversible component of desiccation shrinkage associated with cement grain dissolution theoretically achieves an ultimate value as indicated above if one presumes

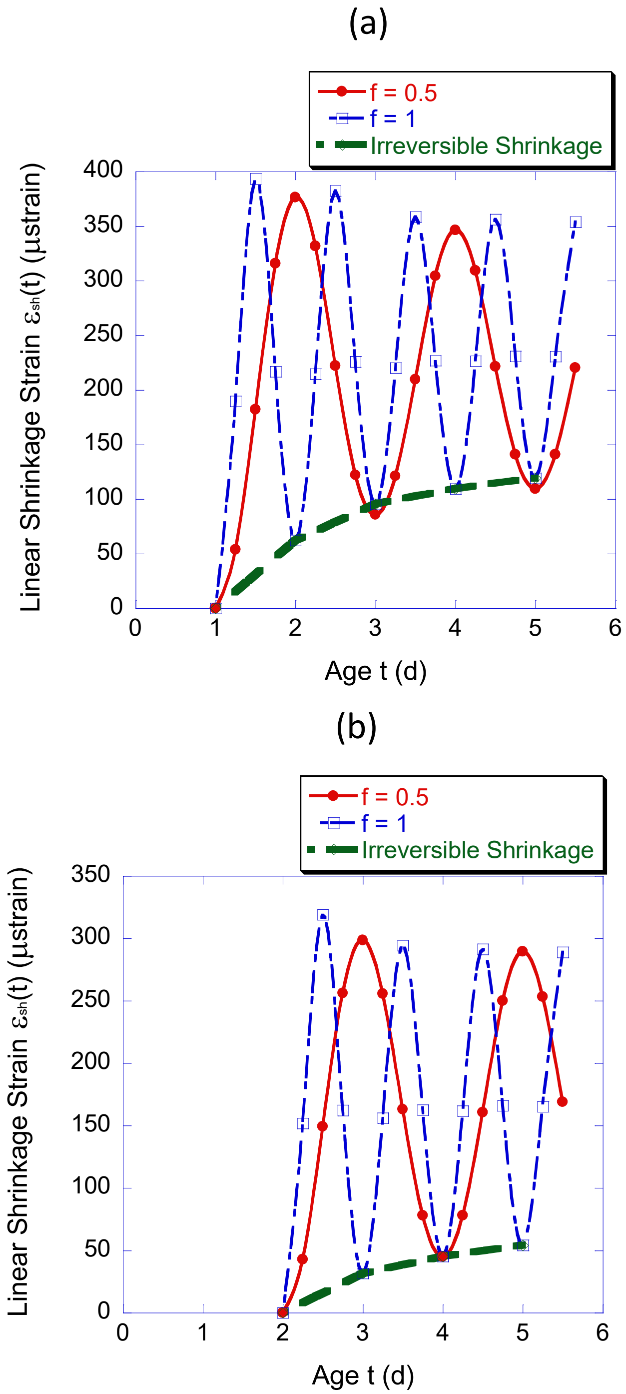

Figure 31 *Predicted shrinkage strain of 0.45 w/c cement paste when exposed to cyclic drying with different frequencies (f=0.5 and f =1) at the initial drying ages of (a) 1 d and (b) 2 d. All the lines in this figure show the predicted shrinkage as a result of cyclic drying due to both pore pressure change and cement grain dissolution effects.*

the solid phases are strictly elastic. This ultimate value would depend on several parameters, including the porosity, pore size distribution, phases present and their respective elastic properties, the drying and hydration kinetics, and the degree of hydration at the onset of desiccation. Given the complexity and multi-parameter dependency of this ultimate irreversible shrinkage, it is not plausible to derive a simple analytical expression to calculate this value.

According to Figure 31(a), more drying and rewetting cycles under the same time period would slightly increase the irreversible shrinkage value, but this increase is less than 10%. It is generally accepted that, under cyclic drying and rewetting, most irreversible shrinkage occurs in the first cycle of drying and rewetting, and the shrinkage strain in the following cycles can be treated as reversible shrinkage [1, 103], but at early ages, according to the simulation results, irreversible shrinkage is more age-dependent rather than cycle-dependent. If the period of one drying cycle is significantly long enough (e.g., 5 days in Figure 31 (a)), the shrinkage occurring after the first cycle can be treated as reversible, but if the period of one drying and wetting cycle is relatively short, the irreversible shrinkage occurring after the first cycle is not negligible.

6.3.6 Combined irreversibility due to dissolution and intrinsic plasticity

As noted in the introduction, irreversible desiccation shrinkage has historically been attributed to irreversible deformation of the C-S-H phase. Here, we evaluate the combined irreversible deformation associated with both irreversible deformation of the C-S-H and dissolution of cement grains. The quasi-instantaneous irreversible deformation of concrete associated with quasi-instantaneous application of stress is generally attributed to microcracking rather than plasticity of the phases (see, e.g., the discussion in Ref. [1, 104, 105] and the references therein). Thus, C-S-H is modeled to exhibit both an instantaneous elastic response and a time-dependent viscoplastic (VP) response to stress.

When utilizing the same *RH* history as in Figure 31 and treating the C-S-H phases inside cement paste as VP, Figure 32 can be obtained showing the shrinkage occurring due to pore pressure changes, cement grain dissolution effects and C-S-H viscoplasticity. As there are no sufficient data currently available for modeling the relaxation of the C-S-H phase over several days due to experimental challenges, for simulation purposes, in Figure 32, the VP Young's modulus of C-S-H was set to be $E(t) = 11.2\ \text{GPa} + 11.2\exp(-0.2t)\ \text{GPa}$, and the Poisson's ratio of C-S-H was assumed to have a constant value of 0.25. The irreversible shrinkage observed in Figure 32 is a combined result of both mechanisms of cement grain dissolution and C-S-H viscoplasticity. Comparing to the irreversible shrinkage occurring due to cement grain dissolution effects, which is more significant at earlier ages, the relative importance of irreversible shrinkage caused by C-S-H viscoplasticity increases with age (through observing the differences between solid lines and dashed lines in Figure 32 at different ages). This is due in part to the fact that the volume fraction of C-S-H phases inside cement paste increases with age. Without dramatic change in the mechanical properties of C-S-H phases (due to either C-S-H viscoplasticity or C-S-H aging), according to the simulation results, cement grain dissolution is still the dominant mechanism leading to shrinkage irreversibility at early ages. The reason for this is that, over relatively short drying cycle periods (i.e., about 1 or 2 days), there is very little relaxation of the C-S-H given the retardation time of 5 days, and 50% maximum relaxation used in the material model for $E(t)$. The material model chosen for C-S-H is not validated by experimental data for C-S-H given the lack of reliable data on C-S-H VE/VP properties. However, given the observed relaxation of cement paste (which includes both intrinsic C-S-H relaxation and dissolution effects) [106], it is reasonable to approximate early-age C-S-H relaxation according to the model used. Thus, the data in Figure 32 indicate that, from a modeling perspective, it may be practicable to disregard irreversible shrinkage during daily drying cycles after the first drying.

In contrast to the limited significance of intrinsic C-S-H VP with respect to irreversible shrinkage during short-term drying cycles, Figure 33 indicates that the influence of the intrinsic irreversible deformation is much more significant for long-term continuous desiccation. In Figure 33, the VE/VP Young's modulus of C-S-H was set to be $E(t) = 11.2 \text{ GPa} + 11.2 \exp(-0.2t) \text{ GPa}$, and the Poisson's ratio of C-S-H was assumed to have a constant value of 0.25. An assumed *RH* history $RH(t) = 80 + 20\exp(-t/14)(\%)$ was applied at different initial drying ages of 1 d and 14 d, where *t* represents the time in days after the start of drying. In Figure 33, the solid lines show the *RH* history, and the dashed lines show the time-dependent shrinkage of cement paste. It can be seen that the longer term drying provides a greater duration for the irreversible VP deformation to develop in the C-S-H, thus making this component of greater potential importance at later ages versus cement grain dissolution

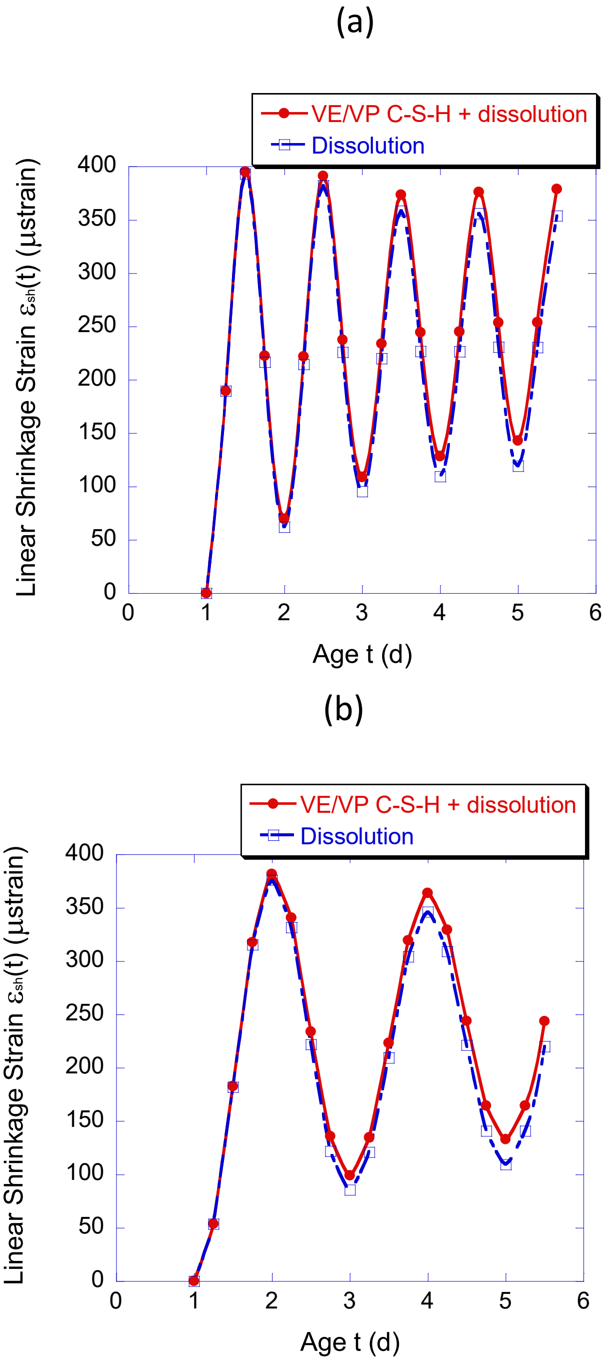

Figure 32 *Predicted shrinkage strain of 0.45 w/c cement paste when exposed to cyclic drying with different frequencies (a) f =1 and (b) f=0.5 when drying is initiated at an age of 1 d. All the lines in this figure show the overall shrinkage as a result of cyclic drying due to pore pressure change, cement grain dissolution effects and C-S-H time-dependent behavior.*

effects. Thus, in contrast to daily cycles, it may not be practicable to ignore long-term irreversible deformation of C-S-H under drying induced stresses. Ultimately, to accurately determine the contribution of C-S-H VP deformation to irreversible desiccation shrinkage (associated with either cyclical or asymptotic drying) requires greater confidence in the VE/VP constitutive function assigned to C-S-H, which requires a significant improvement in available experimental data.

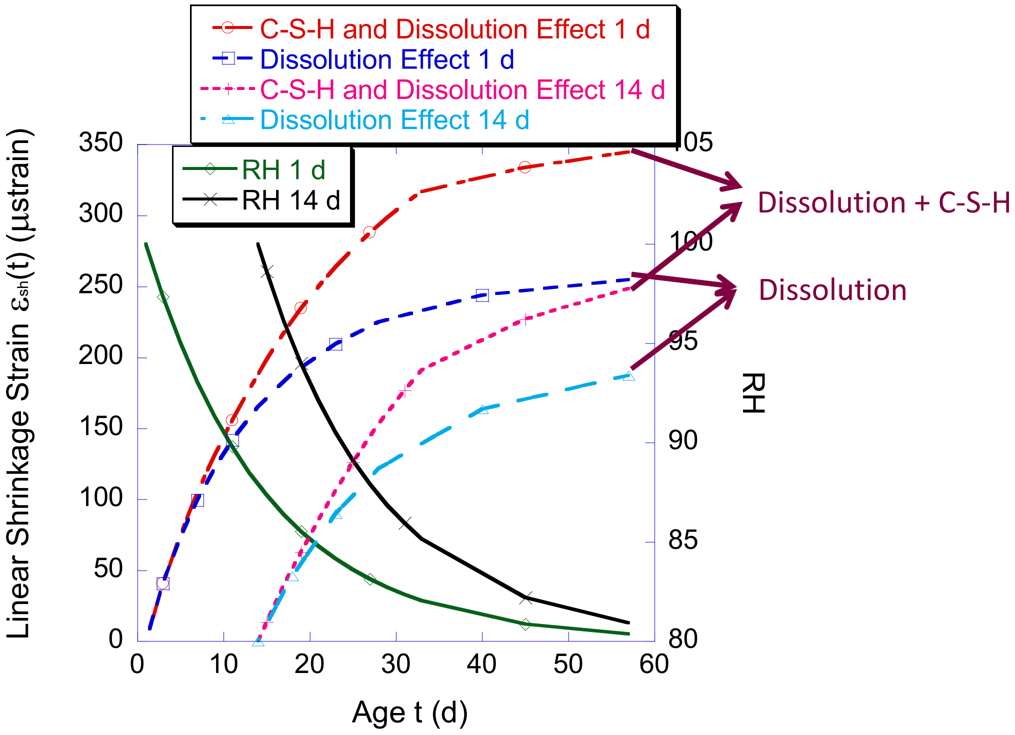

Figure 33. *Simulation of response of 0.40 w/c cement paste to long-term drying with ages of drying initiation of 1 d and 14 d. The longer term drying allows more time for VP deformation to develop within the C-S-H than occurs during short-term cycles. The solid lines show the RH history, and the dashed lines show the time-dependent shrinkage of cement paste.*

6.4 Summary

Dissolution of load-bearing cement grains of hydrating cement paste is a significant factor leading to the irreversible component of early age cement paste shrinkage. Poroelasticity under-predicts the overall early age shrinkage of cement paste as it neglects the dissolution effect of cement grains during the hydration process. The simulations also imply that irreversible shrinkage is closely related to age; delayed drying would lead to drastic reductions in irreversible shrinkage associated with cement grain dissolution. According to cyclic drying and rewetting simulations, the number of cycles has a much smaller influence on the irreversible shrinkage than the age of the sample; thus, if drying cycles are sufficiently slow, then one would expect irreversible shrinkage only on the first cycle, whereas for fast cycles, one would expect irreversible shrinkage on subsequent cycles as well.

At early ages, simulation results indicate that cement grain dissolution is likely more important than intrinsic C-S-H viscoplasticity with regards to irreversible desiccation shrinkage. For long term asymptotic drying, however, irreversible deformation within the C-S-H phase may significantly impact irreversible shrinkage. It is impossible to determine the precise magnitude of influence at this time due to a lack of quality data for intrinsic, long-term C-S-H viscoplastic properties.

7. CREEP/RELAXATION CAUSED BY STRESS-INDUCED DISSOLUTION

The creep and relaxation associated with the dissolution of unhydrated cement grains quantified in previous chapters is insufficient to fully account for experimentally measured creep and relaxation of cement paste. The dissolution of solid hydrates under stress/strain as governed by the second law of thermodynamics could also potentially lead to VE/VP behavior of cement paste. Thus, the mechanism of stress-induced dissolution of solid constituents is quantified and implemented into the computational model in this chapter. Virtual experiments are also carried out to evaluate this mechanism towards the overall viscoelasticity/viscoplasticity of cement paste.

7.1 Background of stress-induced dissolution

Dissolution of solid, load-bearing phases inside cement paste leads to significant apparent creep/relaxation behavior. According to the second law of thermodynamics, dissolution/precipitation of solid constituents could be altered by the change of stress/strain fields inside cement paste via alteration of the stress power or strain energy terms. Thus, it is hypothesized that stress-induced dissolution can affect the overall creep/relaxation behavior of cement composites.

Although the mechanism of stress-induced dissolution has not been systematically introduced and probed in cementations materials, it has long been established as one mechanism leading to creep/relaxation in other materials, which is also referred to as "pressure solution" or "dissolution creep" [107-112]. It has been suggested that pressure solution can lead to significant creep/relaxation in gypsum [107, 113], limestone[114, 115], quartz [116, 117], polymers [118, 119], olivine [120], etc. Meanwhile, it has been demonstrated by others that stress can strongly affect the hydration process of cement paste [121-123]. Thus, with the potential that both thermodynamics and hydration kinetics could be impacted by the stress/strain state, stress-induced dissolution of solid constituents is a plausible mechanism [9] contributing to the VE/VP behavior of cement composites.

In the original version of the scheme, cement grains dissolve as time evolves following empirically derived hydration kinetics equations to simulate the hydration reaction, and the hydration products and pore solution are treated as one single thermodynamic system that steps slowly from one equilibrium state to another. In this chapter, to strictly examine the effect of stress-induced dissolution of solid phases rather than confusing this mechanism with the mechanism of hydration-induced dissolution of cement grains, all the specimens analyzed in the virtual experiments are over 56 d old, where the hydration reaction can be approximated as inactive. The hydration reaction in the computationally implemented program is manually "turned off" such that the applied stress/strain becomes the only source that can lead to microstructure change of cement composite. After the loading age, according to the second law of thermodynamics, the internal thermodynamic state of every solid constituent would change as a result of applied external/internal stress/strain. The whole microstructure of cement paste would evolve with time following both the thermodynamic law (as the solid constituents tend to maintain a thermodynamic equilibrium state with the pore solution) as well as the dissolution kinetics of each constituent. The computational scheme will then predict the time-dependent mechanical properties of cement paste as a function of these time-evolving microstructures.

7.2 Conceptualization

7.2.1 Thermodynamic framework

The concept of evolving natural configurations [28, 30, 36] together with mixture theory [124] was utilized to quantify the effect of stress/strain on the thermodynamic equilibrium state of composite materials. According to the concept of evolving natural configurations, a material body would deform from the reference configuration to the current configuration when subjected to external or internal stimuli. For the body of a cement paste specimen, as it deforms under mechanical loadings, chemical hydration process progresses simultaneously. Its natural configuration, which the body would return to when stimuli is removed, also evolves with time. The kinetic framework of this process is shown in Figure 34. In Figure 34, χ s denotes the motions of the material body between different configurations. For any species *i* inside the composite material, its motion is defined by $\mathbf{x}_{\kappa}^{i} = \chi_{\kappa}^{i}(\mathbf{X}^{i}, t)$, where $\mathbf{x}_{\kappa}^{i}$ is the position vector of species *i* in the current configuration, $\mathbf{X}^{i}$ is the position vector of species *i* in the reference configuration, and the boldface indicates a vector (or, in general, a higher order tensor). Thus, it is easy to derive that, for any species *i,*

$$\begin{aligned} &\text{deformation gradient } \mathbf{F}^{i} = \frac{\partial \mathbf{x}_{\kappa}^{i}}{\partial \mathbf{X}^{i}}, \\ &\text{velocity } \mathbf{v}^{i} = \frac{d\mathbf{x}_{\kappa}^{i}}{dt}, \text{ and} \\ &\text{velocity gradient } \mathbf{L}^{i} = \text{grad}(\mathbf{v}^{i}) = \end{aligned} \tag{45}$$

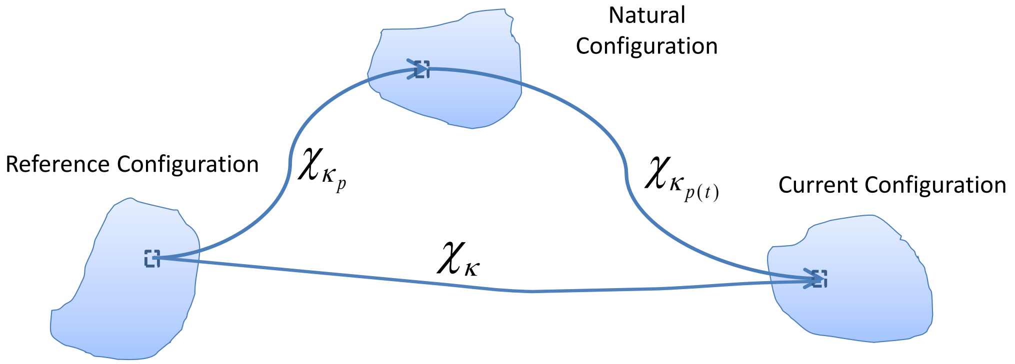

Figure 34 *Overview of the thermodynamic framework of the concept of evolving configurations.* χ *s denote the motions of a material point between different configurations. The body deforms from the reference configuration to the current configuration under external or internal stimuli. As a chemical process progresses, the natural configuration, which the body will return to when stimuli is removed, may also evolve with time.*

The quantification of the effect of mechanical stress/strain fields on the thermodynamic equilibrium of a material body is achieved through the term of stress power. The volume specific stress power of species *i* is defined by $\lambda^i = \boldsymbol{\sigma}^i \cdot \mathbf{L}^i$, where $\boldsymbol{\sigma}^i$ is the Cauchy stress tensor applied to species *i*. Through decomposition of the deformation gradient, one finds that [97, 125]

$$\lambda^i = \lambda^i_{\kappa_{p(t)}} + \lambda^i_{\kappa_p} = \boldsymbol{\sigma}^i \cdot \mathbf{L}^i_{\kappa_{p(t)}} + \boldsymbol{\sigma}^i \cdot \mathbf{L}^i_{\kappa_p}, \tag{46}$$

where $\lambda^i_{\kappa_{p(t)}}$ is the non-dissipative volume specific stress power and $\lambda^i_{\kappa_p}$ is the dissipative volume specific stress power of species *i*. The terms $\mathbf{L}^i_{\kappa_{p(t)}}$ and $\mathbf{L}^i_{\kappa_p}$ represent the velocity gradient of species *i* for motion $\chi^i_{\kappa_{p(t)}}$ and $\chi^i_{\kappa_p}$ respectively.

According to mixture theory [125], when ignoring mass diffusion, the rate of the change in internal energy for species *i* can be expressed as

$$\rho^i \frac{du^i}{dt} = \rho^i r^i - \mathrm{div}(\mathbf{j}_q^i) + V^i \lambda^i - \mu^i \frac{dm^i}{dt} - \mathbf{v}^i \cdot \mathbf{m}^i + \frac{1}{2}(\mathbf{v}^i \cdot \mathbf{v}^i)\frac{dm^i}{dt}, \qquad (47)$$

where ρ^i is the density, u^i is the total stored internal energy, r^i is the mass specific rate of radiant heating, $\mathbf{j}_q^i$ is the mass specific heat flux, V^i is the volume, μ^i is the mass specific chemical potential and m^i is the mass of species *i*. $\mathbf{m}^i$ is the momentum transferred from other species to species i. The rate of entropy production for species *i* can be expressed according to

$$\rho^i \zeta^i = s^i \frac{dm^i}{dt} + \rho^i \frac{ds^i}{dt} - \rho^i \frac{r^i}{T^i} + \mathrm{div}(\frac{\mathbf{j}_q^i}{T^i}), \qquad (48)$$

where ζ^i is the mass specific rate of entropy generation, s^i is the mass specific entropy, and T^i is the temperature of species *i*. If the term $T^i s^i \frac{dm^i}{dt}$ is assumed to be equal to $-\frac{1}{2}(\mathbf{v}^i \cdot \mathbf{v}^i)\frac{dm^i}{dt} + \mu^i \frac{dm^i}{dt}$, with $\mathrm{div}(\frac{\mathbf{j}_q^i}{T^i}) = \mathrm{div}(\mathbf{j}_q^i) - \frac{\mathbf{j}_q^i}{(T^i)^2}\mathrm{grad}(T^i)$, through combining (47) and (48), it can be derived that

$$T^i \rho^i \zeta^i = T^i \rho^i \frac{ds^i}{dt} - \rho^i \frac{du^i}{dt} + V^i \lambda^i - \mathbf{v}^i \cdot \mathbf{m}^i - \frac{\mathbf{j}_q^i}{T^i}\mathrm{grad}(T^i). \qquad (49)$$

The rate of the thermodynamic potential of species *i* (ω^i) thus becomes

$$\rho^i \frac{d\omega^i}{dt} = \rho^i \frac{du^i}{dt} - T^i \rho^i \frac{ds^i}{dt} = V^i \lambda^i - \mathbf{v}^i \cdot \mathbf{m}^i - \frac{\mathbf{j}_q^i}{T^i}\mathrm{grad}(T^i) - T^i \rho^i \zeta^i. \qquad (50)$$

Since $\rho^i \frac{d\omega^i}{dt} = \frac{\partial \rho^i \omega^i}{\partial t} + \mathrm{div}(\rho^i \omega^i \mathbf{v}) - \mu^i \frac{dm^i}{dt}$, where $\mathbf{v} = \sum_{i=1}^{n} \frac{1}{\rho} \rho^i \mathbf{v}^i$, (50) can be rewritten as

$$\frac{\partial \rho^i \omega^i}{\partial t} + \mathrm{div}(\rho^i \omega^i \mathbf{v}) = \mu^i \frac{dm^i}{dt} + V^i \lambda^i - \mathbf{v}^i \cdot \mathbf{m}^i - \frac{\mathbf{j}_q^i}{T^i} \mathrm{grad}(T^i) - T^i \rho^i \zeta^i . \qquad (51)$$

Summing (51) over all the species in the mixture under the equilibrium state, with $\sum_{i=1}^{n} T^i \rho^i \zeta^i = 0$ and $\sum_{i=1}^{n} \mathbf{v}^i \cdot \mathbf{m}^i = 0$, it can be obtained that

$$\frac{\partial \rho \omega}{\partial t} + \mathrm{div}(\rho \omega \mathbf{v}) = \sum_{i=1}^{n} \mu^i \frac{dm^i}{dt} + \sum_{i=1}^{n} V^i \lambda^i - \sum_{i=1}^{n} \frac{\mathbf{j}_q^i}{T^i} \mathrm{grad}(T^i). \qquad (52)$$

For mixtures comprised of purely elastic phases exhibiting small deformation gradients and negligible temperature gradients, according to (46), (52) can be simplified as

$$\rho d \qquad {}_{i=1}^{n} \qquad {}_{i=1}^{n} \qquad . \qquad (53)$$

where ε is the infinitesimal strain tensor for species *i*. When integrating over time,

$$\rho d\omega = \sum_{i=1}^{n} \mu^i dm^i + \sum_{i=1}^{n} V^i \boldsymbol{\sigma}^i d\boldsymbol{\varepsilon}^i . \qquad (54)$$

An alternative yet equivalent form of (54) in units of moles is

$$Gn(\mathbf{a}) = \sum_{i=1}^{n} a^i (\psi^i + e^i), \qquad (55)$$

where a^i denotes the number of moles of species i, $\mathbf{a} = \{a^i\}$, ψ^i denotes the mole specific chemical potential of species i, and $Gn(\mathbf{a})$ is the scalar total thermodynamic potential as a function of $\mathbf{a}$. The term e^i is the mole specific strain energy of species i with the expression $e^i = \frac{1}{a^i} \int V^i \boldsymbol{\sigma}^i d\boldsymbol{\varepsilon}^i = \frac{V^i \boldsymbol{\sigma}^i \boldsymbol{\varepsilon}^i}{2} \frac{1}{a^i}$. According to the second law of thermodynamics [126, 127], for a system to reach thermodynamic equilibrium, the expression in (55) should be minimized while the moles of the species $\{a^i\}$ follow the mole balance constraint of the independent components. The expression in (55) is the essential thermodynamic function utilized in the computational scheme introduced in this research project.

7.2.2 Dissolution kinetics

It can be seen from eq. (55) that, once stress is applied, the mole specific thermodynamic potential for all load-bearing phases will increase (because the strain energy is always positive or zero). For the whole thermodynamic system to reach thermodynamic equilibrium and to minimize the total thermodynamic potential stored in the system, the amount of load-bearing phases would tend to decrease, resulting in the dissolution of solid phases. Once dissolution occurs, the solid phases can no longer be approximated as maintaining a near-equilibrium state with the pore solution, and the solid phases would dissolve with time following the dissolution kinetics of each solid constituent.

The dissolution process is a non-elementary reaction, which involves many elementary steps, including the breaking of each bond of the crystal unit from the lattice, diffusion of the unit away from the lattice site, the detachment of the unit from the crystal surface, and the multi-step decomposition of the unit in solution to individual hydrated ions. In general, the overall dissolution rate of a solid phase is often expressed as the product of kinetic terms with a thermodynamic driving force. According to experiments [128, 129], the thermodynamic driving force for dissolution/growth of a solid is Q / K_{eq}, where Q is the activity product for the solid dissolution reaction and K_{eq} is the equilibrium value of the activity product (the equilibrium constant or solubility product, which is a function of the chemical potential). When a solid phase is in equilibrium with the pore solution, the value of Q / K_{eq} equals 1. When stress/strain is applied on this phase, the value of K_{eq} would increase as a result of applied strain energy, thus the value of Q / K_{eq} will be less than 1, leading to dissolution of this solid phase.

Consider the dissolution of portlandite (CH[5]) in water:

$$\mathrm{Ca(OH)_2} \rightleftharpoons \qquad \mathrm{2OH^-},$$

where the dissolution rate equation is written as

$$\dot{l} \qquad A_{CH}[1-(\frac{Q_{CH}}{K_{eq\_CH}})^2], \tag{56}$$

where $\dot{l}$ is the net dissolution/growth rate, k_{CH}^f is the kinetic rate constant, A_{CH} is the surface area, Q_{CH} and K_{eq_CH} are the activity product and equilibrium activity product of CH, respectively. The value of k_{CH}^f has been measured experimentally at room temperature with $k_{CH}^f = 7.19 \times 10^{-6} \mathrm{mol\ m^{-2}s^{-1}}$.

The derivation process of the dissolution rate of C-S-H is more complicated because (a) the solid phase is like a solid solution with an activity different from one, (b) water is involved as a reactant and not just a catalyst in the overall reaction, and (c) the surface area of C-S-H is difficult to measure in the saturated state. For simplification purpose, the phase C-S-H is approximated as a stoichiometric solid with fixed composition (meaning that activity is equal to one), and the activity of water in pore solution is also approximated to one as it is typically greater than 0.9. Thus,

---

[5] Cement chemistry oxide notation will be utilized in this work.

$$C_xSH_y+(1+x-y)H_2O \rightleftharpoons \qquad +H_3SiO_4^-+(2x-1)OH^- ,$$

and

$$\dot{1} \qquad {}^{f}_{C-S-H} A_{C-S-H}(1-\frac{Q_{C-S-H}}{K_{eq\_C-S-H}})^3 \tag{57}$$

where $\dot{1}$ is the net dissolution/growth rate, k^f_{C-S-H} is the kinetic rate constant, A_{C-S-H} is the surface area, Q_{C-S-H} and K_{eq_C-S-H} are the activity product and equilibrium activity product of C-S-H, respectively. The value of k^f_{C-S-H} has been measured experimentally to be equal to 1.5×10^{-10} mol $m^{-2}s^{-1}$.

For the other solid constituents inside cement paste, as currently there is not sufficient experimental data to quantify their kinetic rate constants, the dissolution/growth rate equations of these phases are uncertain. For better simulation purpose, some of these phases are assigned with the same kinetic equations to that of C-S-H or CH in the computational scheme. Ettringite and hydrotalcite are assigned to dissolve/grow following the same dissolution equation as C-S-H, while monosulfate and monocarbonate are assigned to dissolve/grow following the same dissolution equation as CH. These assignments are taken as “best guess”, as these phases are most resembled structurally to C-S-H or CH. For all the other phases left inside cement composite, as the total volume occupation of these phases is less than 5% in matured specimens (older than 56 d), the dissolution/growth of these phases can only make limited differences. No dissolution/growth kinetic rules are assigned to them, and they are allowed to freely dissolve/grow inside the computational scheme independent of the state of stress or strain.

7.3 Computational implementation

7.3.1 Computational implementation

The computationally implemented model developed in this chapter is an updated version of the (hydration-induced) cement grain dissolution prediction model introduced in [23, 67, 130]. The cement grain dissolution prediction model has been utilized in different areas to predict the time-dependent behavior of cement composites [23, 67, 130]. Based on this model, with the hydration reaction “turned off” inside the program, the newly developed (stress-induced) dissolution prediction model is composed of three, fully coupled parts: a finite element model that calculates the time-evolving stress/strain fields as well as the mechanical properties of cement composite, a thermodynamic engine that predicts the speciation of the composite based on the thermodynamic laws, and a microstructure model that generates 3D microstructure images based on the calculated composite speciation. To account for the time and history dependence of the behavior of the cement composite, the whole model is discretized in time. Figure 35 shows the flow chart of the computationally implemented model, with FEM being the finite element mechanical model, GEMS (Gibbs Energy Minimization) being the thermodynamic engine, and THAMES (Thermodynamic Hydration and Microstructure Evolution) being the microstructure model.

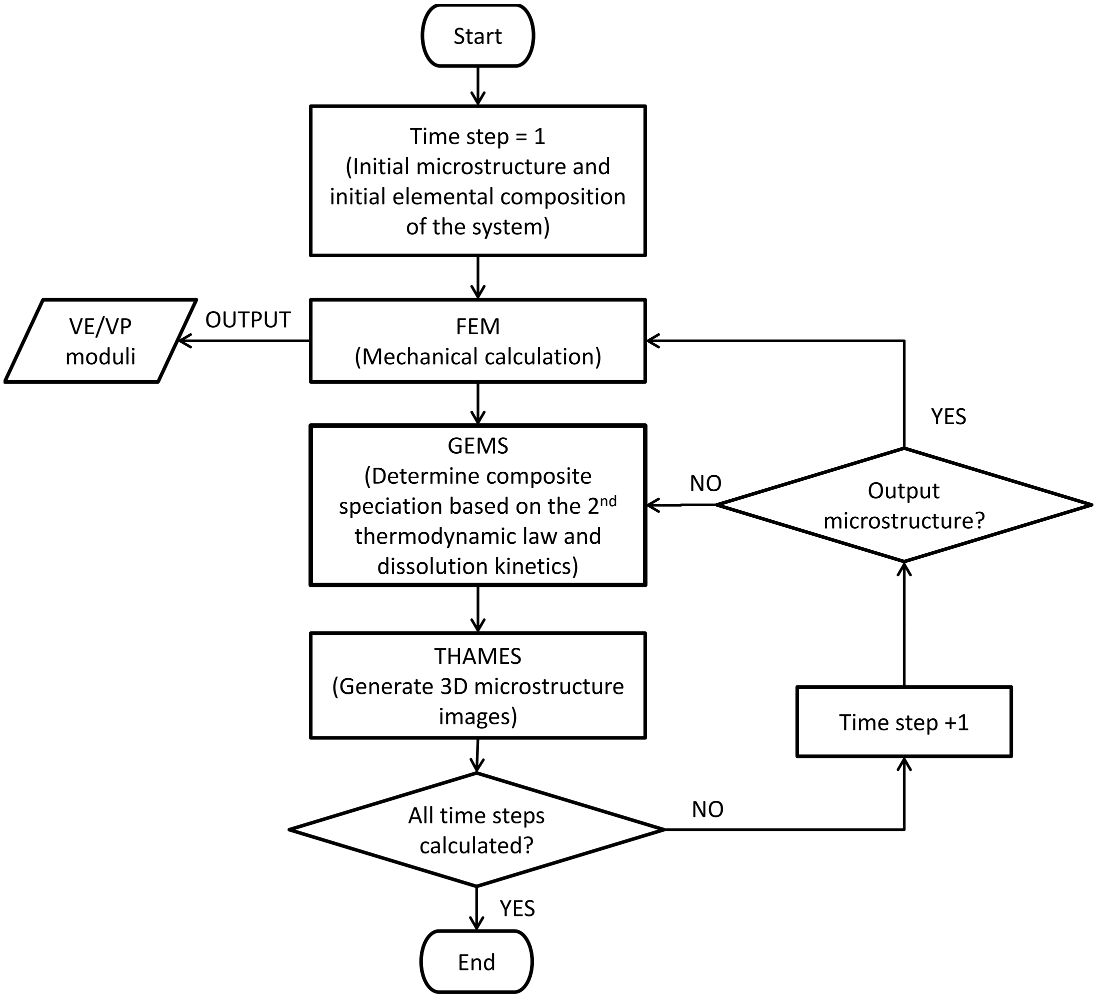

Figure 35 *Flow chart of the computationally implemented model.*

Before the start of the program, two primary files are input into the computational program, including the 3D microstructure image of cement paste at the loading age (where the loading age is 56 d or later) and the composition of the system (which is composed of hydrates and pore solution) at this age. Every 3D microstructure image utilized is one snapshot of a cement composite that is directly mapped to a finite element mesh, with each voxel being an eight-node tri-linear cubic element consisting of a unique phase. All the 3D images are of the dimension of 100^3 voxels, with each voxel occupying the space of 1 μm^3. When the scheme starts in the program, the 3D image file is meshed as a finite element model (FEM) for mechanical calculation.

The finite element calculation model embedded in the program predicts the time-dependent VE/VP moduli of cement paste as a function of time-evolving microstructures. In the model, constant strain-controlled periodic boundary conditions are applied on a representative volume of cement composite (whose microstructure may evolve with time), and through minimizing the total mechanical energy stored in the system at each age, the stress/strain fields can be calculated. One assumption made in the model is that, once dissolution occurs in one voxel inside the microstructure (as a result of applied stress/strain), all the historical responses stored in this voxel may be disregarded, and the newly-formed phases form in the deformed configuration carrying no stress. Stress is redistributed from dissolved phases to the surrounding solid phases at a very fast rate, much faster than the chemical processes inside cement paste, increasing the stress carried by the remaining solid constituents and resulting in creep/relaxation of cement paste on the bulk scale. Since all the phases in the model were assigned to be purely elastic with elastic properties taken from [22], the predicted creep/relaxation by FEM occurs strictly due to the dissolution of solid, load-bearing phases.

Besides calculating the apparent VE/VP moduli of cement paste in FEM, according to eq. (55), to accurately account for the effect of strain energy on changing the thermodynamic state of a cement composite system, the mole specific strain energy for each phase should also be calculated in the program. Based on the averaged strain energy of each phase inside the composite, the mole specific strain energy for species *i* can be calculated through

$$e^i = \frac{V^i}{n}\sum_{j=1}^{n}\frac{\sigma_j^i \varepsilon_j^i}{2}, \tag{58}$$

where n is the total number of voxels inside the composite (or chosen subdomain in the composite) that consist of phase *i*, V^i is the molar volume of phase *i*, and $\frac{\sigma_j^i \varepsilon_j^i}{2}$ is the strain energy calculated for voxel *j* that is consist of phase *i*. Implementing (58) into (55), the total change in thermodynamic potential of the composite due to internal strain energy change can be calculated.

With the initial input of the elemental composition of the system and the calculated strain energy from FEM, GEMS (Gibbs Energy Minimization) [46, 47, 131] calculates the composite speciation of the system at equilibrium state. It is assumed in GEMS that a near-equilibrium state is achieved between the hydration products and the pore fluid solution, and according to the second law of thermodynamics, the total stored Gibbs free energy stored in the system should be minimized.

In the original version of the thermodynamic engine utilized in previous simulations [23, 67, 130], the total stored Gibbs free energy was calculated through

$$G(\mathbf{a}) = \sum_{i=1}^{n} a^i \psi^i, \tag{59}$$

where $G(\mathbf{a})$ is the scalar total Gibbs energy as a function of speciation vector $\mathbf{a}$. Equilibrium speciation $\mathbf{a}$ in the chemical system was found by minimizing the total Gibbs free energy $G(\mathbf{a})$. At the beginning of the program, the elemental composition of the thermodynamic system was input into GEMS, and GEMS calculated the formation of the dependent species following the mole balance constraint of the independent elements. In the updated version of GEMS, to account for the effect of stress power, the total thermodynamic potential, which is calculated through eq. (55), is minimized. The mole specific strain energy $\{e^i\}$ is obtained from eq. (58), and the same calculation algorithm as implemented in the original version of GEMS (which was used to minimized eq. (59)) is utilized to determine the equilibrium speciation $\mathbf{a}$.

One thing to note is that although the total amount of solids that tend to dissolve/form as a result of applied stress/strain can be calculated in the updated GEMS, the actual amount of solids that can really dissolve/form between two neighboring time steps are strictly limited by the dissolution kinetic rules of every solid phase. In cement pastes, the dissolution/formation of solid constituents occurs over a finite period of time, and the rate of this process depends on many factors. According to previous sections, the dissolution/formation rate of one solid phase depends on: 1) an empirically derived kinetic constant, 2) the surface area of this solid phase that is in contact with the pore solution, and 3) a thermodynamic driving gradient, which is expressed as Q / K_{eq}. For each solid phase, its surface area can be calculated at each time step utilizing the 3D microstructure images, and its thermodynamic driving force, Q / K_{eq}, is a direct output from GEMS. Thus, with the known kinetic constant, the net dissolution rate of every solid constituent can be calculated in the program (e.g., the net dissolution rate of CH and C-S-H can be calculated utilizing eq. (56) and (57)). The total amount of one solid phase that is "kinetically allowed" to dissolve/form between two neighboring time steps is calculated through $\dot{l}$, where $\dot{l}$ is the net dissolution/formation rate of a solid phase, and Δt is the time gap between these two time steps.

To account for the change in the computational scheme due to changes in equilibrium induced by strain energy as well as the dissolution kinetics, the following routine was implemented into GEMS. At any time step $t = t_n$, the speciation of the system from the previous time step can be obtained from GEMS, denoted as $\mathbf{a}(t_{n-1}) = \{\mathrm{a}^i(t_{n-1})\}$. Meanwhile, the amount of different species that are allowed to dissolve/form between these two time steps, $\mathbf{d}_{t_{n-1}} = \{d^i_{t_{n-1}}\}$, could also be calculated utilizing the dissolution kinetics: $d^i_{t_{n-1}} = \dot{l} \quad t_{n-1})$, where $\dot{l}$ is the net dissolution/formation rate of species i at time step $t = t_{n-1}$. After the internal stress/strain state changes in the composite as a result of the microstructure evolution at the current time step, the new speciation $\mathbf{a}(t_n)$ should be calculated. When GEMS tends to calculate the new $\mathbf{a}(t_n)$ utilizing the thermodynamic law, one constraint was set ahead in the program that $\mathbf{a}(t_n) \geq \mathbf{a}(t_{n-1}) - \mathbf{d}_{t_{n-1}}$. In this way, it is assured in the program that no more solid will dissolve/form at each time step than the allowed amount, and the dissolution kinetic laws for solid constituents are strictly followed. One thing to note here is that, once dissolution kinetics were implemented into GEMS, the hydrates can no longer be approximated as being in quasi-equilibrium state with the pore solution. The whole system will remain non-equilibrium (and this is why solids will continuously dissolve) until all the solid phases that are required to dissolve by the second thermodynamic law (through minimizing eq. (55)) has fully transformed into pore solution.

THAMES [44, 45] originally was a hydration based microstructure model, which predicts the microstructure evolution of cement paste during the hydration reaction. In this chapter, the hydration reaction in THAMES was manually "turned off" (as all the specimens tested in the chapter are over 56 d old and the hydration reaction can be treated approximately as stopped). Starting from the initial input 3D microstructure image, and with the calculated dissolved/formed solid phases from GEMS, THAMES predicts the 3D microstructure evolution under the constant applied strain at each time step. There are several factors that THAMES considers in determining the spatial locations of the newly-dissolved or newly-formed phases: 1) the local geometric information regarding interfaces to restrict the location where one particular constituent can grow, 2) the empirical information regarding the growth/dissolution habit of each constituent (*e.g.*, random, acicular, isotropic) and 3) the stress/strain field distribution inside cement paste to determine the dissolution or formation order of one particular phase. Detailed discussions regarding the first two factors can be found in [44, 132]. With the implementation of strain energy into the computation scheme, the third factor becomes a new major factor that affects the dissolution/formation location preference of a solid constituent. Inside the program, the strain energy of each voxel was calculated in FEM. For the dissolution process, voxels exhibiting higher strain energy will dissolve prior to the voxels with lower strain energy. Although the surface tension between the water phases and solid phases also affects the location preferences of the dissolved solids, comparing to the stress/strain exhibited on these phases, the effect of surface tension is presumed limited (as the magnitude of surface tension is much smaller than the magnitude of the stresses applied on the voxels). As for the precipitation of new solid phases, since they all form in a stress-free state, the stress/strain distribution inside cement composite will not affect their growth location.

After calculating the 3D microstructure of cement paste in THAMES at the current time step, the next step in the program is to determine whether to output the 3D microstructure of cement paste from THAMES to FEM. To accurately simulate the dissolution process inside cement paste, a relatively fine set of time steps is required (e.g., the simulation of solid phase dissolution right after loading age can progress in units of hours), which, however, is finer than required for the mechanical calculations in FEM (in which the creep/relaxation rate of cement paste is calculated in units of days or even months). As the major utility of the microstructures in this program is to carry out mechanical finite element analysis and predict stress/strain fields inside cement paste, the required time gap between two neighboring microstructure output ages can be much wider than the crucial time gap (necessary for accurately simulating the dissolution process). Thus, the program only passes the 3D microstructure images from THAMES to FEM at desired ages. If the age in the program has reached the next microstructure output age, a 3D microstructure snapshot that is directly mapped to a finite element mesh is input into FEM. If the age in the program has not reached the next microstructure output age, the program loops over directly to the next round of calculation in GEMS.

In summary, and as shown in Figure 35, the flow of the computationally implemented model is as follows:

1. FEM calculates the apparent VE/VP moduli of cement paste at each age and also calculates the strain energy of different phases. The information of the strain energy is then updated in GEMS.
2. GEMS calculates the amount of dissolved/formed solid phases and inputs into THAMES.
3. THAMES generates 3D microstructure images.
4. Depending on ages, if the microstructure is not to be input into FEM, go back to step 2 and increase time step; otherwise, input the microstructure into FEM, go back to step 1 and increase time step.
5. Loop over until all time steps are calculated.

7.3.2 Choice of thermodynamic equilibrium domain size

The essence of the thermodynamic framework utilized in GEMS is that the second law of thermodynamics holds for one mixture system, but the question as to whether this mixture system should be considered as the whole cement paste composite or a subdomain of the composite is unsettled. The term "domain" is defined here as the sub mixture system (inside the whole cement composite) over which the thermodynamic equilibrium is enforced. As the dimension of the whole cement paste composite in the computational model is fixed as 100^3 voxels (each of 1 μm^3 volume), when subdividing the cement composite equally, e.g., the composite is divided into 2^3 subdomains (2 sections per axis), the size of a domain inside the program would be 50^3 voxels.

The introduction of the concept of domains into the program is essential, especially when the effect of strain energy is taken into account. When a cement composite is subjected to external load, the stress/strain field inside the composite is not uniformly distributed, as well as the mole specific strain energy and stress power of each species *i*. If the whole cement composite is treated as one single domain, the strain energy for any species *i* is calculated through spatial averaging of the strain energy of species *i* over the whole composite, as shown in eq. (58). This disregards the non-uniform distribution of strain energy and leads to a potential result that one could under-predict or over-predict the dissolution of solid phases. For example, when the averaged strain energy over the whole composite as a result of external applied load is insufficient to induce a speciation change according to eq. (55), while however, due to the relatively higher stress/strain concentration in some local areas (with respect to the global area of the whole composite), solids in these areas tend to dissolve (because of the high local strain energy). Neglecting these locally higher strain energies by averaging over the whole composite could cause an under-estimation of the stress relaxation or creep of cement paste. Similarly, when the averaged strain energy is large enough to cause solid phase dissolution on the global scale, while in some local areas, the effect of strain energy is not as significant, the creep/relaxation of cement paste is over-predicted in that locale. Thus, to more accurately predict the amount of dissolved solid constituents, as well as creep/relaxation of cement paste, the concept of an equilibrium domain should be introduced into the computational scheme.

While it is clear from the above discussion that the thermodynamic domain must not be too large (at the risk of neglecting locally high/low strain energy), such a domain may not be too small, either. At the extreme lower limit, each domain could be the size of an individual voxel (consisting of one phase) – in this case, one does not have a true mixture, and the derived thermodynamic relationships are inapplicable. Thus, the appropriate domain size must be large enough to consider the constituents within the domain as a mixture of solids and pore solution, yet small enough to capture local strain energy effects.

To computationally implement the concept of domains into the program, Figure 36 shows the updated conceptual flow chart of the computational scheme for one time step. At the beginning of each time step, FEM predicts the inherent stress/strain field inside the original 3D microstructure. The VE/VP moduli of cement paste are still calculated based on the averaged stress/strain over the bulk composite paste, while the strain energy was averaged within each domain and recorded in GEMS. Then in the program, as the whole cement paste (with dimension of 100^3 voxels) is equally subdivided into different domains in space, the amount of aqueous solution together with all the hydrate phases within each domain (and thus the elemental composition within each domain) could be calculated based on the microstructure image. Depending on the different mole specific strain energies inside each domain as well as composition, the program calculates the dissolution rates for the solid constituents inside each domain separately. Then, based on these calculated dissolution rates and the second law of thermodynamics, the new speciation of each domain at the end of this time step are calculated. The sum of these calculated speciation from all the domains is the overall speciation of the whole mixture system. For each species i, $a^i = \sum_{d=1}^{n} a_d^i$, where a_d^i is the amount of species i in d th domain and n is the total number of domains.

One thing to note is that after involving the concept of domain, when a solid phase dissolves within one domain at one time step, the same phase could precipitate in another domain at the same time. Due to the combined result of the dissolution and precipitation process, the total amount of dissolved solid phases within the whole composite between two neighboring time steps could be underestimated by simply adding up the speciation composition of all domains, as well as the total amount of precipitated solid phases. As THAMES predicts the microstructure evolution based on the total amount of dissolved and precipitated phases, direct input of the summed speciation of the composite into the microstructure model would lead to incorrect microstructure prediction. To avoid this problem, inside this computationally implemented program, THAMES will predict the microstructure evolution in two parts for each time step. First, THAMES calculates the cement paste microstructure based the on the composite speciation where only dissolution is allowed to occur, while the precipitation process is neglected. The input speciation is $\{a^i\} = \{\sum_{d=1}^{n} a(dissolve)_d^i\}$, where $a(dissolve)_d^i = a_d^i$ if species i dissolves within d th domain; otherwise, $a(dissolve)_d^i$ equals the originally input amount of species i in d th domain before the thermodynamic calculation has been carried out. For the small microstructure considered in the program, diffusion of solutes between time steps considered always cover the whole volume of the composite (100^3 μm^3), which is pre-requested in THAMES [44]. THAMES will compare the new phase and speciation composition of the system with the phase and speciation composition of the system from previous time step to get the true amount of dissolved phases. The location of the newly dissolved solids can be determined according to the factors discussed previous sections. Then the new speciation $\{a^i\} = \{\sum_{d=1}^{n} a_d^i\}$ would be input into THAMES. Through comparing $\{\sum_{d=1}^{n} a(dissolve)_d^i\}$ and $\{\sum_{d=1}^{n} a_d^i\}$, the total amount of newly precipitated solids can be calculated. THAMES then determines the location of these precipitated phases and calculates the finalized 3D microstructure.

As noted previously, a major concern regarding the implementation of subdomains into the computational scheme is that, to accurately account for the non-uniform distribution of stress/strain fields inside cement paste, a relatively fine division of the composite system (100^3 voxels) is required. The finer the division (or the smaller the size of one domain), the more accurately the localized stress/strain can be accounted for. Theoretically, the smallest domain size the program could choose is 1^3 voxel. However, as the concept of “domain” is that one domain can reasonably represent the thermodynamic condition of the entire mixture, which includes both liquid aqueous solution and solid hydrates, both the existence of a reasonable amount of pore solution voxels and precipitated hydrates voxels are required. Thus, one major challenge of this

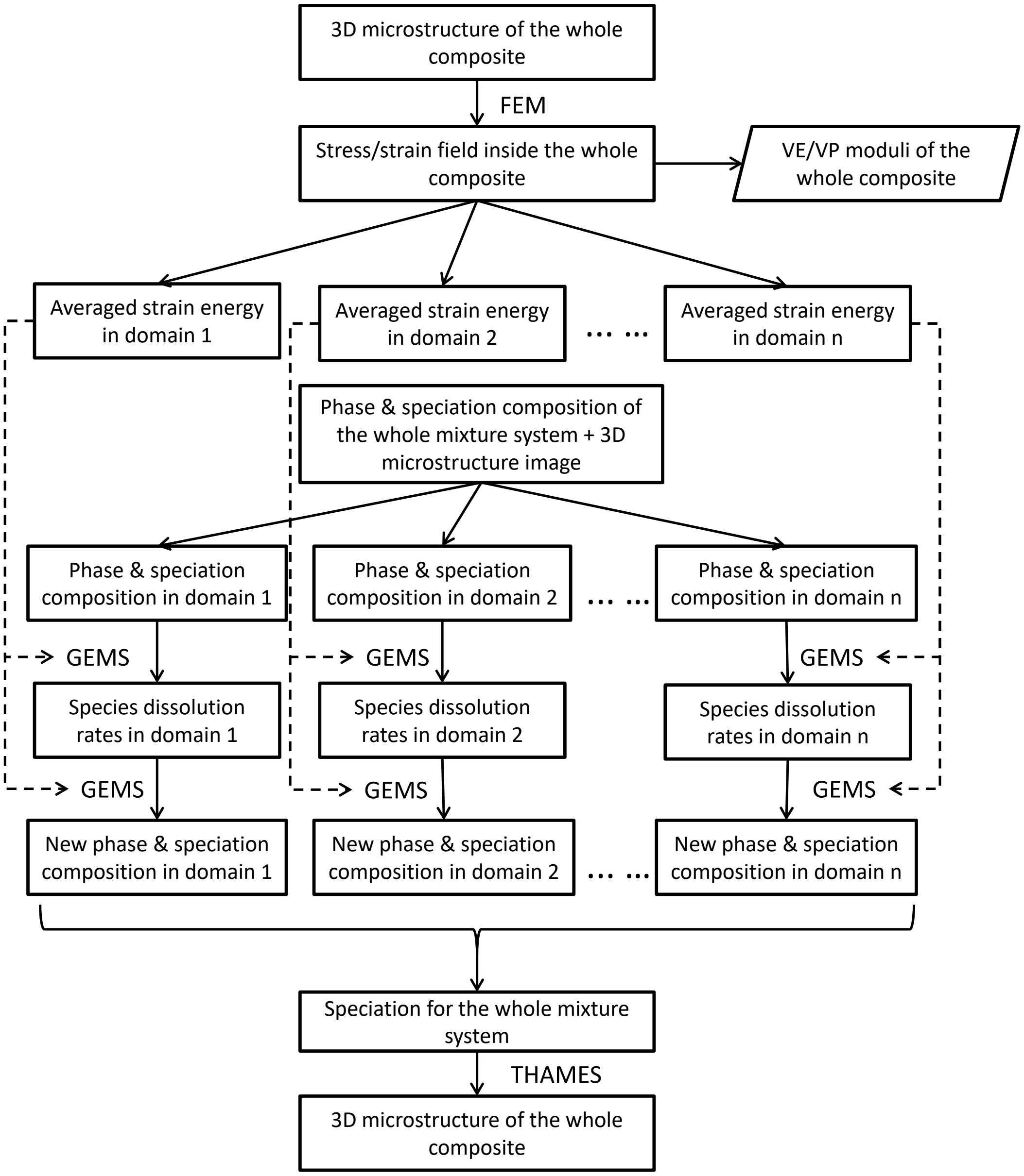

Figure 36 *Conceptual flow of the computational scheme for one time step when implementing the concept of domains.*

computationally implemented program is to define a correct choice of the domain size for the cement paste tested. If the size of a domain is too large, the program could not account for the non-uniform distribution of stress/strain; if the size of a domain is too small, the “invalid” mixture systems will lead to inaccurate predictions. In this chapter, after various virtual experiments carried out on portland CCRL 168 cement, the most appropriate choice of domain size was identified.

7.4 Simulation results and discussions

7.4.1 Different choices of domain size

The first task in this section is to determine the most appropriate choice of domain size such that the non-uniform distribution of strain energy inside the cement composite could be captured in the computational program, while at the same time requiring that each domain chosen is a representative mixture system (no extremely low or high volume fraction of one particular phase within this domain). One thing to clarify here is that there is no single appropriate choice of domain size that is universal for all different types of porous composite materials, but this choice depends on many factors, e.g., different materials (different cement types for cement pastes, or different sizes of aggregates in concrete) and microstructure size (dimension of the microstructure image and coarseness of voxelation). To derive the appropriate choice of domain for the considered cement paste composite, a series of virtual experiments were carried out. In all the virtual experiments discussed, the cement pastes utilized were comprised of portland cement CCRL 168, and the phases inside the cement pastes were all assigned with linearly elastic properties taken from [22]. In this way, the predicted time-dependent behavior of cement paste occurs strictly due to the dissolution of solid phases, and the resultant calculated moduli associated with the dissolution process are referred to as the “apparent VE/VP moduli”.

Figure 37 shows the predicted apparent VE/VP Young’s modulus of 0.45 *w/c* cement paste as a function of time when loaded at the age of 56 d. The cement pastes were subject to external strain-controlled boundaries, and two virtual controlled strains, (a) 0.0001 and (b) 0.0002, were applied on the specimens. After the loading age, the hydration reaction within the specimens are considered as stopped in the program, and all the predicted relaxation of cement occurs due to stress-induced dissolution of solid constituents. Four different choices of domain size are included in this figure, with the size of the domains being 100^3 voxels, 50^3 voxels, 20^3 voxels and 10^3 voxels (the total number of domains within a cement composite being 1, 2^3, 5^3 and 10^3). It can be seen from the figure that, due to different choices of domain size, even when under the same boundary conditions, the simulation results show significant differences.

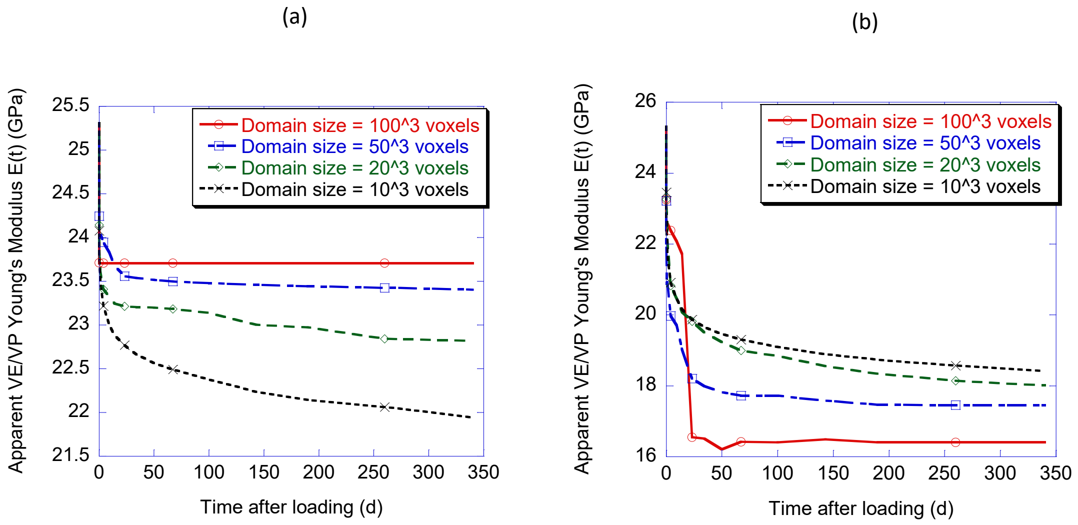

Figure 37 *Predicted relaxation of the apparent VE/VP Young's modulus of 0.45 w/c cement paste when loaded at 56 d. Different periodic controlled strain (a) 0.0001 and (b) 0.0002 were applied on cement paste microstructures, and four different choices of domain size, 1003 voxels, 503 voxels, 203 voxels and 103 voxels, were utilized to obtain the figure. The relaxation of cement paste in this figure occurs purely as a result of stress-induced dissolution of solid constituents.*

From Figure 37(a), when the external applied boundary strain is 0.0001, smaller domain size will give higher prediction of cement paste relaxation. This is because under this applied strain, the averaged strain energy over the whole composite is insufficient to induce dissolution of solid phases over the whole microstructure. While on the other hand, when the microstructure is divided into domains, strain energy concentration at local areas could be accounted for, inducing solid phase dissolution in these areas. Thus, a finer division of domain could more accurately account for the strain energy concentration, inducing more localized phase dissolution and larger predicted relaxation of cement pastes. Similarly for Figure 37(b), when the applied boundary strain is relatively high (0.0002), the averaged strain energy over the whole composite causes the dissolution of solid constituents on the global scale. When the division of domains can more accurately justify the non-uniform distribution of strain energy, the dissolution of solid phases in some low-stressed areas is prohibited, leading to a lower prediction of cement paste relaxation within finer domain divisions. In summary, from the perspective of the concern of strain energy concentration, a finer division of the microstructure would lead to a better prediction of cement paste relaxation, and according to Figure 37(a) and (b), domain sizes of 100^3 voxels and 50^3 voxels might not be sufficiently fine to account for the non-uniform stress/strain distribution inside cement paste.

Another observation from Figure 37 is that, as the size of the chosen domain decreases, the predicted relaxation results do not necessarily converge. Although under higher strain (0.0002 as shown in Figure 37(b)), some convergence occurs as the size of domain gets smaller, under a lower strain (0.0001 in Figure 37(a)), the divergence between different predicted results can even increase as the size of a domain goes down. As discussed in previous sections, a finer division of domain does not necessarily lead to a more accurate prediction. When the size of a domain is too small, this domain could no longer be defined as a mixture system, and the calculation in GEMS could no longer be applied on this domain. From the 3D microstructure data, for 0.45 *w/c* cement paste at the age of 56 d, the average volume fraction of pore solution within the composite is around 7.4%. When the composite is divided into 10^3 domains (with the size of each domain being 10^3 voxels), around 37% of the domains will have a pore volume fraction less than 5%, and the lowest pore volume fraction within a domain can reach 0% (no pore solution within this domain). When the composite is divided even finer to 20^3 domains (with the size of each domain being 5^3 voxels), the number of the domains with less than 5% pore volume fraction reaches up to 45%.

In summary of the observations from Figure 37, when domain size is too large, the non-uniform distribution of strain energy inside cement paste cannot be addressed properly. As the domain size decreases, the predicted apparent Young's modulus of cement paste under different choices of domain might show some convergence. With the further decrease of the domain size, because the small domains can no longer be treated as the representative of thermodynamic mixture systems, the predicted relaxation of cement paste could start to diverge. For the microstructures utilized in this chapter (100^3 voxels), as the microstructure is subdivided into more sections per axis (1, 2, 3…100 sections per axis), the size of a domain can differ from 100^3 voxels, 50^3 voxels to 5^3 voxels, 4^3 voxels or even 1^3 voxels. One thing to note is that under some choices of divided sections, the size of the domains inherent the microstructure can be inconsistent, e.g., the size of a domain can be either 33^3 voxels or 34^3 voxels when the microstructure is subdivided into 3 sections per axis. Theoretically, as the domain size gets smaller, the divergence among the neighboring predicted apparent VE/VP Young's modulus under neighboring choices of domains (when each axis of the microstructure is subdivided into adjacent integers) should reach the minimum under certain choice of domain. This choice of domain with the minimum divergence was utilized as the most appropriate choice of domain size. To obtain the most appropriate choice of domain, the divergence among different serials of data sets should be quantified.

In this research project, for any three neighboring predicted data series of $E(t)$ under adjacent choices of domain, the averaged standard derivation among these three data series is utilized as the "divergence" of these three predicted $E(t)$. For example, when each axis of the microstructure is divided into 7 sections (14^3 voxels or 15^3 voxels per domain), the predicted $E(t)$ under this choice of domain will be compared with the predicted $E(t)$ when the microstructures is subdivided into 6 sections (16^3 voxels or 17^3 voxels per domain) and 8 sections (12^3 voxels or 13^3 voxels per domain). To obtain each relaxation curve of $E(t)$, a fixed number of j data points (or j time steps implemented inside FEM) would be predicted by the computational program, and the "divergence" can be calculated through

$$Divergence = \frac{1}{j}\sum_{i=1}^{j} s.t.d.(t_j)\,, \tag{60}$$

where $s.t.d.(t_j)$ is the standard derivation of the three predicted value of $E(t_j)$ under the three different choices of domain size. Figure 38 shows the calculated divergence among the different series of predicted $E(t)$ under different choices of domain sizes. 0.45 *w/c* cement paste was utilized to obtain this figure. Controlled strain of 0.0002 was applied at the age of 56 d, and the size of the domain varies from 100^3 voxels (1 section per axis) to 5^3 voxels (20 sections per axis). One thing to note is that, for the domain size of 100^3 voxels, because there is only one neighboring domain size next to it (50^3 voxels, or 2 sections per microstructure axis), the standard derivation was calculated based on only two data series of $E(t)$. Meanwhile, as the microstructure images get divided finer and finer, at some point, even when the microstructure is divided into different sections per axis, the sizes of the domains do not differ much, e.g., 17 and 18 sections. This could potentially lead to very similar predicted $E(t)$ under these choices of divided sections because the size of domain basically does not change, while the divergence between different domain sizes cannot be demonstrated appropriately. Thus, when selecting the data for obtaining Figure 38, the chosen adjacent domain sizes should differ at least one voxel per axis. For example, when selecting the neighboring domain sizes for the domain of 10^3 voxels, the adjacent domain size should be at least 11^3 voxels or at most 9^3 voxels. From Figure 38, it can be seen that, the divergence reaches the minimum values at the domain sizes between 15^3 voxels and 25^3 voxels. Therefore, in this dissertation, a domain size of 20^3 voxels (when dividing the composite into 5 sections per axes) is utilized as the finalized appropriate domain size, which lies in the middle of the range where the divergence is minimized.

There are also some other reasons behind choosing the domain size of 20^3 voxels. First, as the distribution of stress/strain fields inside cement paste is closely related to the phase distribution inside cement paste, and thus partially depends on the particle size distribution of the cement studied in the program. Portland cement CCRL 168 is the only cement utilized in the simulations in this research project, and according to the particle size distribution test carried out on this type of cement, the median effective diameter of the CCRL 168 cement grains is 11 μm and the mode diameter of the CCRL168 cement grains is around 20 μm [44]. When the size of domain is assigned 20^3 μm^3 (20^3 voxels), the diameter of cement grains with respect to the domain dimension is

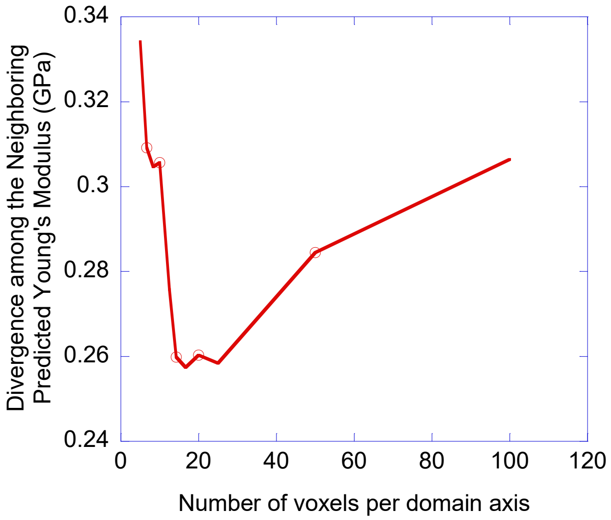

Figure 38 *Calculated divergence among neighboring predicted apparent Young's modulus under different choices of domain size. Controlled strain of 0.0002 was applied on 0.45 w/c cement paste at 56 d. The sizes of the domains differ from 1003 voxels to 53 voxels.*

relatively large, this choice of domain division can partially account for the stress/strain concentration inside cement paste. Second, when the domain size is 20^3 voxels, less than 20% of the domains will have a pore volume fraction less than 70% of the averaged pore volume fraction of the composite, and the lowest pore volume fraction among all these domains is around half the value of the averaged composite pore volume fraction. This could avoid the problem of inadequate aqueous solution inside one domain mixture system. Based on these two aspects, and meanwhile, from the virtual experiment results shown in Figure 38, the domain size choice in this research project is finalized as 20^3

voxels. All the following virtual experiments discussed in this research project are carried out under this choice of domain size.

7.4.2 Stochastic microstructures of cement paste

Besides different choices of cement paste, the prediction results from the computationally implemented model also vary depending on different input microstructures of cement paste. Because of the stochastic nature of the microstructure model, even for cement pastes with the same characteristic properties (e.g., *w/c*), different initial input microstructures could be generated for cement pastes under the same age. Although the microstructures differ from each other, their speciation compositions as well as mechanical elastic properties are essentially the same. Figure 39 shows the predicted apparent VE/VP Young's modulus of cement paste when loaded at the age of 56 d. Three different microstructures of CCRL 168 cement with *w/c* equal to 0.45 were created and subdivided into 20^3 domains. Two virtual controlled strains, (a) 0.0001 and (b) 0.0002, were applied on these specimens to obtain the figure. In Figure 39, all the phases inside the cement pastes were assigned linearly elastic properties and all the predicted relaxation of cement occurs due to stress-induced dissolution of solid constituents.

From Figure 39, it can be seen that under the same external boundary conditions, the same characteristic properties of cement paste, the same loading age and the same choice of domain size, different initial input microstructures could still lead to some differences in the predicted relaxation results. Because of the involvement of the concept of domain into the program, the location and the inherent phase composition of each domain become important factors that influence the final computed results. For the domains located in the same location within different microstructures, due to their

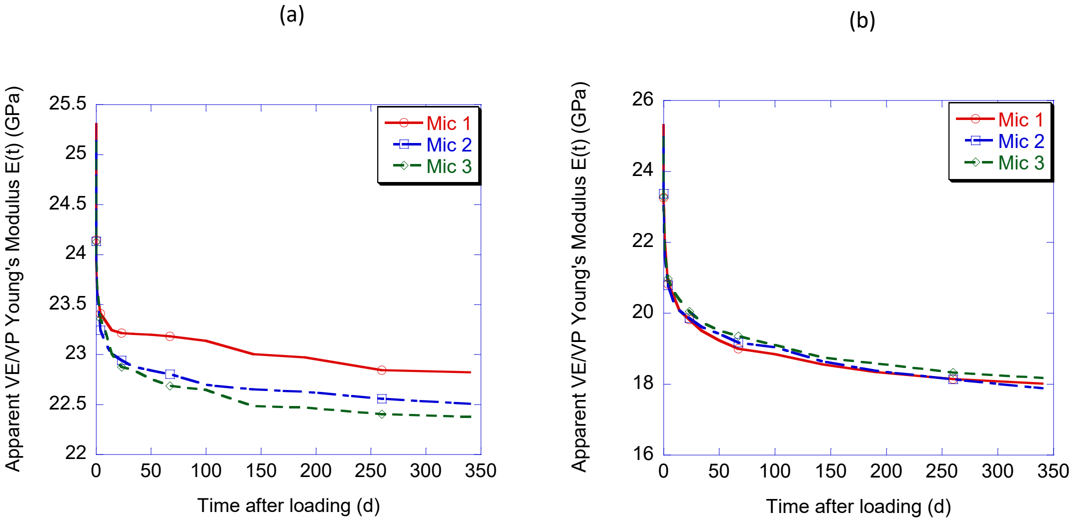

Figure 39 *Predicted relaxation of the apparent VE/VP Young's modulus of three different microstructures of 0.45 w/c cement paste when loaded at 56 d. Different periodic controlled strain (a) 0.0001 and (b) 0.0002 were applied on cement paste microstructures, and the choice of domain size is 203 voxels. The relaxations of cement paste in this figure occur purely as a result of stress-induced dissolution of solid constituents*

different surrounding environments, the calculated strain energy within these domains could be different, affecting the overall prediction of the VE/VP properties of cement paste. Thus, for the prediction of the relaxation/creep of cement paste caused by stress-induced dissolution of solid constituents, the prediction results can vary from microstructure to microstructure. These differences on phase composition and the local microstructure environment are also responsible for the discrepancies on the predicted relaxation when different domain sizes are chosen, as shown in Figure 37. From both Figure 39 and Figure 37, when the externally applied strain is at a relatively high value (0.0002), the differences in the predicted results caused by different choices of domain size (when the chosen domain size are 20^3 voxels and 10^3 voxels) and by different input cement paste microstructures are much smaller than under a smaller boundary strain (0.0001). One potential reason behind this is that, when the applied strain is smaller, the occurrence of phase dissolution within a domain has a higher dependency on the phase composition and microstructure environment of this domain. According to the second law of thermodynamics, dissolution of solid phases would only occur after the applied strain energy reaches a certain value. When the strain energy is lower, the amount of the domains that experience phase dissolution is less. For any slight changes in the microstructure inside one domain, it could potentially promote or prohibit the dissolution of solid phases in the surrounding domains, and thus affecting the overall amount of the solid phases that tend to dissolve in the microstructure. When the applied stress/strain is high, solid phase dissolution has already occurred in most domains. Changes in the microstructures would have less impact in the amount of dissolving solid phases, and thus leads to less discrepancy in the computed results.

7.4.3 Different magnitudes of applied strain/stress

Figure 40 shows the predicted apparent VE/VP Young's modulus of 0.45 *w/c* cement paste when loaded at the age of 56 d. Periodic controlled strain varying from 0.0001 to 0.0025 were applied on the cement composites. Domain size of 20^3 voxels was utilized in the figure. From Figure 40, it can be seen that the predicted relaxation of cement paste increases with the magnitude of applied strain. As the applied strain/stress increases, the strain energy exhibited on the solid phase voxels increases. This strain energy increase promotes more solid phase dissolution and promotes increasing dissolution rates of the solid phases, and thus induces larger and faster relaxation/creep behavior of cement pastes. Dissolution of solid constituents associated with strain energy can be a substantial mechanism leading to cement paste VE/VP behavior.

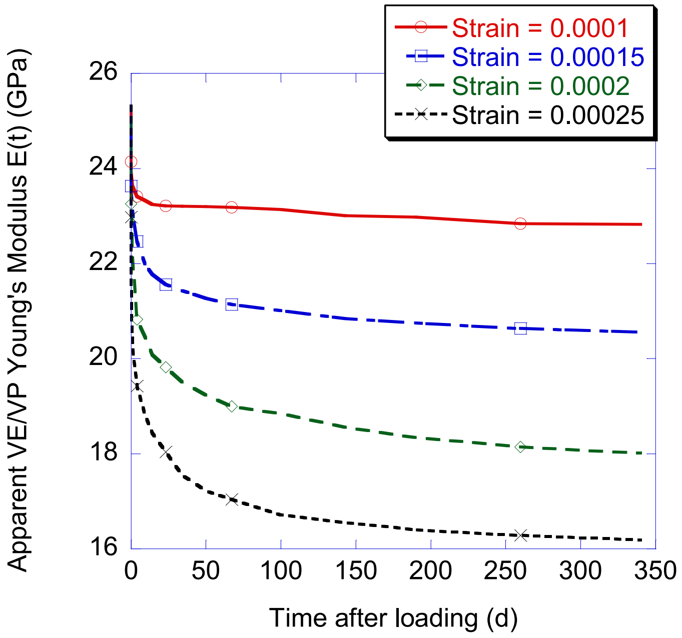

Figure 40 *Predicted relaxation of the apparent VE/VP Young's modulus of 0.45 w/c cement paste when loaded at 56 d. Different periodic controlled strain were applied on cement paste microstructures, and the choice of domain size is 203 voxels. The relaxation of cement paste in the figure occurs as a result of the combined effect of dissolution of solid constituents.*

7.4.4 C-S-H and CH dissolution

When cement pastes are of 56 d old or older, the two major components of the solid constituents inside cement composites are C-S-H and CH [1]. The dissolution of these two phases under load is the major source leading to stress-induced relaxation/creep of cement paste. When cement pastes were under controlled strains as shown in Figure 40, the total amounts of dissolved C-S-H and CH versus time are shown in Figure 41. Boundary strains were applied on 0.45 *w/c* cement paste at the age of 56 d, and domain size of 20^3 voxels was utilized in Figure 41.

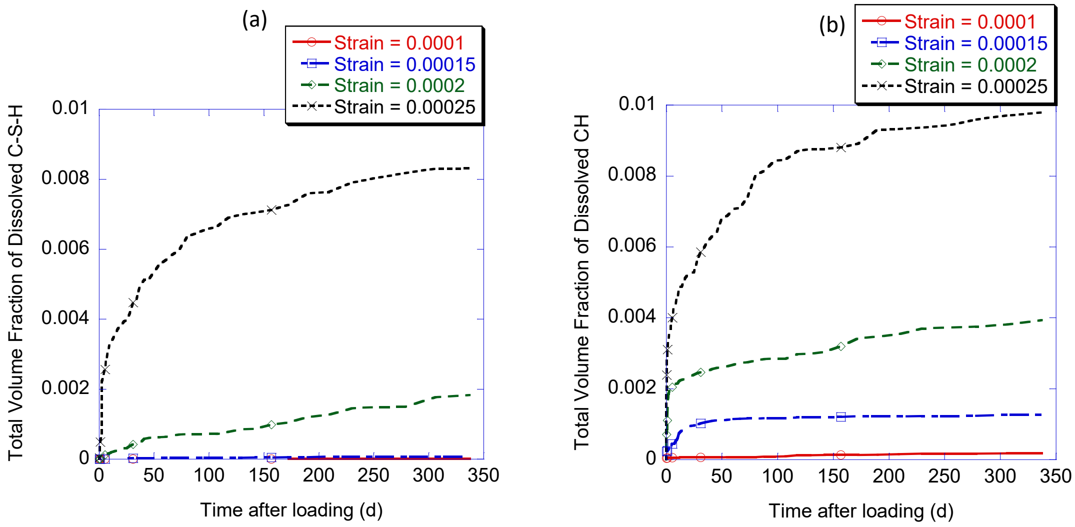

Figure 41 *Total volume fraction of dissolved (a) C-S-H and (b) CH of 0.45 w/c cement paste when loaded at 56 d. Different periodic controlled strain were applied on cement paste microstructures, and the choices of domain size is 203 voxels.*

Before loading, the volume fraction of C-S-H inside the simulated cement paste was 0.4427 and the volume fraction of CH was 0.1869. These two phases occupied over

60% of the volume of cement paste. Then in Figure 41, after load is applied, both C-S-H and CH would gradually dissolve into pore solution with time as a result of strain energy. The total amount of dissolved C-S-H and CH as well as the dissolution rate of C-S-H and CH increase with the magnitude of applied strain. Due to the different dissolubility (or dissolution kinetics) of C-S-H and CH, the dissolution rate of CH might be higher than C-S-H in a short time right after loading (through comparing Figure 41(a) and Figure 41(b) under controlled strain of 0.00015 and 0.0002), at later ages, however, the dissolution rates of these two phases are mostly governed by the magnitude of applied stress/strain. The dissolution process would slow down with time as the mixture system (which includes both the hydrate phases and pore solution) gradually reaches equilibrium state. Although it seems in Figure 41 that the total amount of dissolved C-S-H and CH does not occupy a significant volume inside cement composite, it is capable of leading to substantial creep/relaxation behavior in cement paste. According to previous research results [23], the dissolution of cement grains between 7 days to 28 days in 0.45 *w/c* cement paste would lead to around 20% relaxation in the predicted apparent VE/VP Young's modulus of cement paste, while the dissolved cement grains only occupy 3.5% volume in the early age specimens. For the specimens tested in Figure 41, the total amount of dissolved C-S-H and CH can reach up to 1.8% volume of cement paste under controlled strain of 0.00025. As the hydrated phases are normally carrying the major portion of the stresses rather the unhydrated cement grains, this means that dissolution of hydrate phases will lead to more stress redistribution inside cement paste, and thus more relaxation/creep in bulk cement composite. In combination with other dissolved solid phases inside cement paste, dissolution of C-S-H and CH is capable of leading to the relaxation shown in Figure 40. In summary, dissolution of C-S-H and CH under stress/strain plays a substantial rule in leading to long-term VE/VP behavior of cement paste.

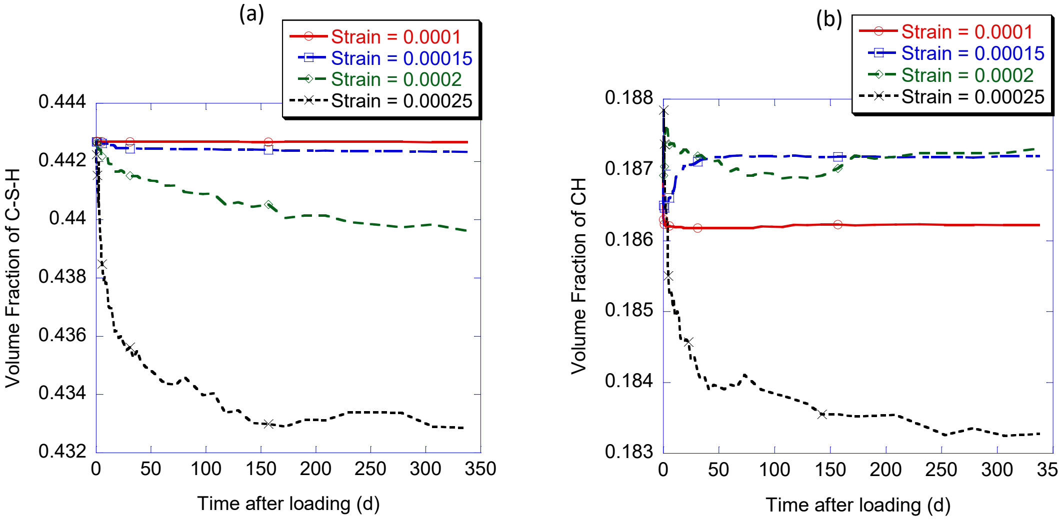

Figure 42 *Predicted volume fraction changes of (a) C-S-H and (b) CH of 0.45 w/c cement paste when loaded at 56 d. Different periodic controlled strain were applied on cement paste microstructures, and the choices of domain size is 203 voxels.*

Figure 42 shows the volume fraction changes of C-S-H and CH versus time under the same condition as in Figure 41. Through comparing Figure 42(b) and Figure 41(b), it can be seen that although the total volume of dissolved CH increases with time under different magnitudes of applied strain, the actual volume fraction of CH does not necessarily decreases with time. In Figure 42(b), other than the case of 0.0001 applied strain, the volume of CH shows different amount of sharp increases right after the application of load (when the applied strains are 0.00015, 0.0002 and 0.00025). This occurs because of the re-precipitation of the CH phases. At the time right after loading, both a portion of C-S-H and CH dissolve, increasing the iconic concentration of the pore solution. Much of the dissolved material would precipitates elsewhere in the microstructure, but not before redistribution of stresses occur. Because the elemental composition of C-S-H (C_xSH_y) is much more complicated than CH, the dissolution of C-S-H would have a much larger impact on the pore solution speciation. This could potentially promote the growth of CH, even under stressed condition, and thus leading to an increase in the volume fraction of CH, as shown in Figure 42(b). Nevertheless, this re-precipitation process will not affect the overall relaxation behavior of cement paste as the newly precipitated phases form in a stress-free state. It is the increasing amount of dissolved C-S-H and CH under stress that induces VE/VP behavior of cement paste.

7.4.5 Different w/c

Figure 43 shows the predicted apparent VE/VP Young's modulus of 0.40, 0.45 and 0.50 *w/c* cement pastes, as well as the normalized apparent VE/VP Young's modulus of these cement pastes, which are normalized by the elastic instantaneous Young's modulus at the loading age. Load was applied at the age of 56 d and periodic controlled strain 0.0002 was applied on the cement composites. Domain size of 20^3 voxels was utilized. From the figures, it can be seen that stress-induced dissolution of solid constituents can cause relaxation in cement pastes with different *w/c.* From Figure 43(b), the total predicted relaxation decreases with *w/c.* From previous discussions, dissolution of C-S-

H and CH phases are likely to be substantial sources leading to the relaxation/creep of cement paste. As the value of *w/c* decreases, the volume fraction of C-S-H as well as CH at the age of 56 d would increase, so too the available amount of C-S-H and CH that could dissolve due to the state of stress in the material. Thus, a lower *w/c* could potentially leads to a higher stress-induced relaxation in cement paste.

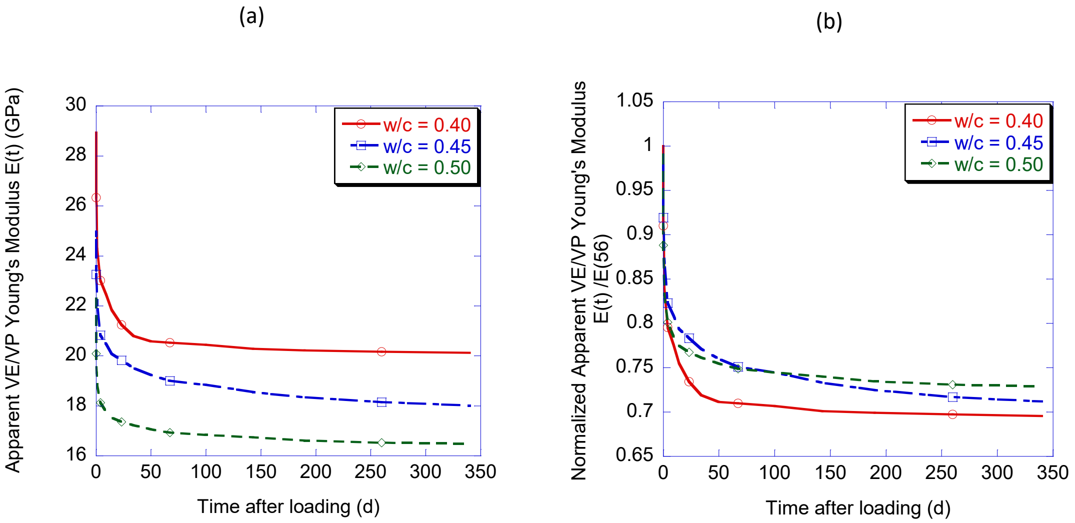

Figure 43 *Predicted relaxation of the (a) apparent VE/VP Young's modulus and (b) normalized apparent VE/VP Young's modulus of 0.40, 0.45 and 0.50 w/c cement paste when loaded at 56 d. The normalization is made by divided by the elastic Young modulus at the loading age. Periodic controlled strain of 0.0002 was applied on cement paste microstructures, and the choice of domain size is 203 voxels. The relaxation of cement paste in the figure occurs as a result of the combined effect of dissolution of solid constituents.*

7.4.6 Different loading ages

Figure 44 shows the predicted apparent VE/VP Young's modulus of 0.40 *w/c* cement paste when loaded at different ages of 56 d, 180 d and 720 d. Periodic controlled strain of 0.0002 was applied on the cement composites. Domain size of 20^3 voxels was utilized in the figure. From this figure, it is clear that the total relaxation time after the loading age can last for years. Unlike the relaxation of cement paste

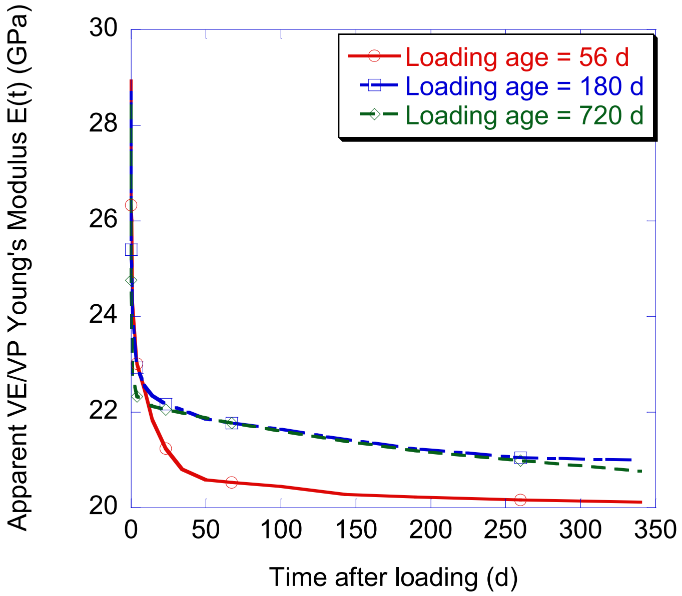

Figure 44 *Predicted relaxation of the apparent VE/VP Young's modulus of 0.40 w/c cement paste when loaded at different ages of 56 d, 180 d, and 720 d. Periodic controlled strain of 0.0002 was applied on cement paste microstructures, and the choice of domain size is 203 voxels. The relaxation of cement paste in the figure occurs as a result of the combined effect of dissolution of solid constituents.*

cause by hydration reaction, which only applies for early-age cement paste, stress induced dissolution of solid phases can explain the long-term relaxation/creep behavior of cement paste, and this mechanism could still be substantial for old (more than around 2 years) specimens. In combination with the discussions from previous sections, stress induced dissolution of solid constituents is an important mechanism leading to long-term VE/VP behavior of cement paste.

7.5 Summary

The mechanism of stress-induced dissolution of solid constituents can increase the overall relaxation/creep of cement paste, and depending on the magnitude of applied load, the effect of this mechanism can be significant. Meanwhile, as stress/strain can be applied at any age, the stress-induced dissolution of solid phases can occur at any age, and the significance of this mechanism does not decrease with age. While hydration induced dissolution only affects early age creep or relaxation, stress induced dissolution may yield long-term (years) creep or relaxation. Among the major solid phases that would dissolve under the effect of applied strain/stress, dissolution of both C-S-H and CH phases can be substantial sources leading to stress-induced relaxation/creep of cement paste.

8. CONCLUSIONS

8.1 Dissertation summary and primary conclusions

A computational scheme that couples a microstructure evolution model and a time-stepping finite element method capable of tracking phase formation was developed to predict the apparent VE/VP properties of cement paste as a function of time-evolving microstructures. A kinematic framework was established to quantify the effect of dissolution of load-bearing phases on the overall stress and strain fields in evolving composite materials. Various virtual experiments have been carried out, and a list of multiple mechanisms that could potentially lead to creep/relaxation behavior of cement paste were evaluated and compared in the manuscript. In order to illustrate the utility of the computationally implemented modeling approach, the early age desiccation shrinkage occurring in hydrating cement was also analyzed. According to the simulation results:

1. Without significant aging effects, intrinsic C-S-H viscoelasticity is not likely the primary mechanism leading to the early-age creep and relaxation behavior of cementitious materials.
2. When intrinsic C-S-H aging operates together with intrinsic C-S-H viscoelasticity, the modeled time-dependent VE/VP properties of cement paste are consistent with the experimentally observed aging effect on cement paste relaxation rates.

3. The apparent VE/VP behavior of hydrating cement paste due to dissolution of cement grains is a significant factor in the overall early-age creep and relaxation of the paste.
4. When comparing the solidification theory with the computational scheme developed herein, the major difference between the two models is to which extent that unhydrated phases can transmit stress, and this difference can strongly influence the interpreted mechanisms behind the VE/VP behavior of cement composites.
5. The time-dependent changes in the apparent VE/VP Poisson's ratio of cement paste are likely controlled by dissolution of cement grains at early ages due to the high early-age hydration rate. Depending on the mechanical properties of C-S-H as well as *w/c* and the loading age of cement paste, later-age cement paste is capable of exhibiting increasing, decreasing, or constant VE/VP Poisson's ratio evolution with time.
6. Dissolution of load-bearing cement grains of hydrating cement paste is a significant factor leading to the irreversible component of early age cement paste shrinkage.
7. The mechanism of stress-induced dissolution of solid constituents can increase the overall relaxation/creep of cement paste, and depending on the magnitude of applied load, the effect of this mechanism can be significant and long lasting (e.g., for years).

8. Among the major solid phases that would dissolve under the effect of applied strain/stress, dissolution of C-S-H and CH phases can both be substantial sources leading to stress-induced relaxation/creep of cement paste.

8.2 Limitations of the computational model and future research

Besides the many advantages of the developed computational scheme, there are also many limitations of the current version of the computational routine. One of the primary limitations is lack of reliable experimental data of the mechanical properties of C-S-H. Experiments are needed to directly measure the aging of C-S-H VE/VP properties in order to test and help improve the accuracy of the aging function used in the model. Due to a lack of reliable data, the simulation results presented in the C-S-H aging section highlight only the *potential* for C-S-H aging to strongly contribute to the overall aging of cement paste creep and stress relaxation. Reliable experimental data that probe explicitly the age dependency of C-S-H creep or relaxation are needed to further evaluate the *extent* to which aging of the C-S-H plays a role in the aging, VE/VP properties of cement paste.

Meanwhile, when simulating the early-age shrinkage behavior of cement paste, the coupling between the hydration reaction and the internal *RH* is neglected. Once the internal *RH* is reduced sufficiently, the hydration rate is substantially slowed or even halted (due to either kinetic or thermodynamic constraints). If hydration slows, then the dissolution of cement grains likely slows correspondingly, which would reduce the amount of irreversible shrinkage expected. However, at early ages where cement grain dissolution rates are more significant, the internal *RH* is generally not reduced to the point where the hydration rate would be significantly affected.

In the future, with the further finalization of this computational scheme and with the utilization of the mechanism of stress-induced dissolution of loading bearing solid constituents inside the model, it could be applied to further more different areas. First of all, prediction of the time-dependent moduli of cement paste under different applied stresses (including Poisson's ratio) at different loading ages, including but not limited to early ages, could be achieved without conducting time-consuming experiments. Meanwhile, with the implementation of the mechanism of stress-induced dissolution of solid phases, the mechanism of drying creep, which is the combined result of mechanical creep and drying shrinkage, could be potentially explained through carrying out more virtual experiments utilizing the computational approach. Besides drying creep, some phenomena associated with supplementary cementing materials, e.g., increased autogenous shrinkage when adding silica fume into the mixture (which will induce more dissolved hydrates under pore pressures at early ages), could also be predicted by this program. Further improvement of the program and application of this program into these areas could be carried out in the future.

REFERENCES

1. Mindess, S., J.F. Young, and D. Darwin, *Concrete*. 2nd ed. 2002, Upper Saddle River, NJ: Prentice Hall.

2. Pierre-Claude, A., *Cements of yesterday and today: Concrete of tomorrow.* Cement and Concrete Research, 2000. **30**(9): p. 1349-1359.

3. Tamtsia, B.T. and J.J. Beaudoin, *Basic creep of hardened cement paste: a re-examination of the role of water.* Cement and Concrete Research, 2000. **30**(9): p. 1465-1475.

4. Powers, T.C., *Mechanisms of shrinkage and reversible creep of hardened portland cement paste Proceedings of International Conference On the Structure of Concrete*. 1968, London, England: Cement and Concrete Association.

5. Ruetz, W., *A hypothesis for the creep of hardened cement paste and the influence of simultaneous shrinkage Proceedings of International Conference On the Structure of Concrete*. 1968, London, England: Cement and Concrete Association.

6. Suter, M. and G. Benipal, *Constitutive model for aging thermoviscoelasticity of reacting concrete I: theoretical formulation.* Mechanics of Time-Dependent Materials, 2010. **14**(3): p. 277-290.

7. Jensen, M. and P.F. Hansen, *Autogenous deformation and change of the relative humidity in silica fume-modified cement paste.* ACI Materials Jounal, 1996. **93**(6): p. 539-543.

8. Leung, C.K. and Z.C. Grasley, *Poromechanical damping of cementitious materials.* Journal of Materials in Civil Engineering, 2012. **24**(2): p. 232-238.

9. Grasley, Z.C., et al. *Elastic and Viscoelastic Properties of Calcium Silicate Hydrate*. in *NICOM 4: 4th International Symposium on Nanotechnology in Construction*. 2012. Crete.

10. Grasley, Z.C. and C.K. Leung, *Desiccation shrinkage of cementitious materials as an aging, poroviscoelastic response.* Cement and Concrete Research, 2011. **41**(1): p. 77-89.

11. Grasley, Z.C., et al., *Dynamic pressurization method for measuring permeability and modulus: II. cementitious materials.* Materials and Structures, 2007. **40**(7): p. 711-721.

12. Coussy, O. and P.J.M. Monteiro, *Poroelastic model for concrete exposed to freezing temperatures.* Cement and Concrete Research, 2008. **38**(1): p. 40-48.

13. Scherer, G.W., *Characterization of saturated porous bodies.* Materials and Structures/Materiaux et Constructions, 2004. **37**(265): p. 21-30.

14. Ulm, F.J., G. Constantinides, and F.H. Heukamp, *Is concrete a poromechanics material? - A multiscale investigation of poroelastic properties.* Materials and Structures/Materiaux et Constructions, 2004. **37**(265): p. 43-58.

15. Jones, C., Z.C. Grasley, and J. Ohlhausen, *Creep indentation of portland cement paste using an atomic force microscope*, in *Jounal of the American Ceramic Society*. n/a.

16. Jones, C.A. and Z.C. Grasley, *Correlation of hollow and solid cylinder dynamic pressurization tests for measuring permeability.* Cement and Concrete Research, 2009. **39**(4): p. 345-352.

17. Grasley, Z., et al., *Dynamic pressurization method for measuring permeability and modulus: II. cementitious materials.* Materials and Structures, 2007. **40**(7): p. 711-721.

18. Hilton, H.H. and S. Yi. *The significance of anisotropic viscoelastic Poisson ratio time dependencies*. in *Proceedings of the American Society for Composites Twelfth Technical Conference, 6-8 Oct. 1997*. 1997. Dearborn, MI, USA: Technomic Publishing.

19. Swamy, R.N., *Dynamic Poisson's ratio of portland cement paste, mortar and concrete.* Cement and Concrete Research, 1971. **1**(5): p. 559-583.

20. Grasley, Z. and D. Lange, *Constitutive modeling of the aging viscoelastic properties of portland cement paste.* Mechanics of Time-Dependent Materials, 2007. **11**(3-4): p. 175-198.

21. Hilton, H.H., *Implications and constraints of time-independent Poisson ratios in linear isotropic and anisotropic viscoelasticity.* Journal of Elasticity, 2001. **63**(3): p. 221-251.

22. Haecker, C.J., et al., *Modeling the linear elastic properties of Portland cement paste.* Cement and Concrete Research, 2005. **35**(10): p. 1948-1960.

23. Li, X., et al., *Modeling the apparent and intrinsic viscoelastic relaxation of hydrating cement paste.* Cement and Concrete Composites, 2015. **55**: p. 322-330.

24. Aydin, A.C., A. Arslan, and R. Gül, *Mesoscale simulation of cement based materials' time-dependent behavior.* Computational Materials Science, 2007. **41**(1): p. 20-26.

25. Jeon, J., J. Kim, and A. Muliana, *Modeling time-dependent and inelastic response of fiber reinforced polymer composites.* Computational Materials Science, 2013. **70**: p. 37-50.

26. Drozdov, A.D., E.A. Jensen, and J.d.C. Christiansen, *Nonlinear time-dependent response of polypropylene/nanoclay melts: Experiments and modeling.* Computational Materials Science, 2010. **47**(3): p. 807-816.

27. Ruetz, W. *A hypothesis for the creep of hardened cement paste and the influence of simultaneous shrinkage*. in *Proceedings of International Conference On the Structure of Concrete*. 1968. London, England: Cement and Concrete Association.

28. Kannan, K. and K.R. Rajagopal, *A thermodynamical framework for chemically reacting systems.* Zeitschrift fur Angewandte Mathematik und Physik, 2011. **62**(2): p. 331-363.

29. Rajagopal, K.R. and A.R. Srinivasa, *On the thermomechanics of materials that have multiple natural configurations: twinning and solid to solid phase transformation.* Zeitschrift fur Angewandte Mathematik und Physik, 2004. **55**(6): p. 1074-93.

30. Rao, I.J. and K.R. Rajagopal, *A thermodynamic framework for the study of crystallization in polymers.* Zeitschrift für angewandte Mathematik und Physik ZAMP, 2002. **53**(3): p. 365-406.

31. Rajagopal, K.R. and A.S. Wineman, *A note on viscoelastic materials that can age.* International Journal of Non-Linear Mechanics, 2004. **39**(10): p. 1547-1554.

32. Lapczyk, I., K.R. Rajagopal, and A.R. Srinivasa, *Deformation twinning during impact - numerical calculations using a constitutive theory based on multiple natural configurations.* Computational Mechanics, 1998. **21**(1): p. 20-27.

33. Lapczyk, I., K.R. Rajagopal, and A.R. Srinivasa, *Deformation twinning during impact of a titanium cylinder - numerical calculations using a constitutive theory based on multiple natural configurations.* Computer Methods in Applied Mechanics and Engineering, 2000. **188**(1): p. 527-541.

34. Rajagopal, K.R. and A.R. Srinivasa, *Modeling anisotropic fluids within the framework of bodies with multiple natural configurations.* Journal of Non-Newtonian Fluid Mechanics, 2001. **99**(2-3): p. 109-124.

35. Rajagopal, K.R. and A.R. Srinivasa, *On the thermomechanics of materials that have multiple natural configurations: viscoelasticity and classical plasticity.* Zeitschrift fur Angewandte Mathematik und Physik, 2004. **55**(5): p. 861-93.

36. Rajagopal, K.R. and A.R. Srinivasa, *On the thermomechanics of materials that have multiple natural configurations Part I: Viscoelasticity and classical plasticity.* Zeitschrift für angewandte Mathematik und Physik ZAMP, 2004. **55**(5): p. 861-893.

37. Rajagopal, K.R. and A.R. Srinivasa, *On the role of the Eshelby energy-momentum tensor in materials with multiple natural configurations.* Mathematics and Mechanics of Solids, 2005. **10**(1): p. 3-24.

38. Ravindran, P., et al., *Modelling sand-asphalt mixtures within a thermodynamic framework: Theory and application to torsion experiments.* International Journal of Pavement Engineering, 2009. **10**(2): p. 115-131.

39. Mura, T., *General theory of eigenstrains*, in *Micromechanics of Defects in Solids*. 1987, Springer Netherlands: Dordrecht. p. 1-73.

40. Bentz, D.P., *Quantitative comparison of real and CEMHYD3D model microstructures using correlation functions.* Cement and Concrete Research, 2006. **36**(2): p. 259-263.

41. Garboczi, E.J., *Finite element and finite difference programs for computing the linear electric and elastic properties of digital images of random materials*. 1998, Building and Fire Research Laboratory,National Institute of Standards and Technology.

42. Bohn, R.B. and E.J. Garboczi, *User manual for finite element and finite difference programs: A parallel version of NISTIR-6269*. 2003, Gaithersburg: U.S. Department of commerce, Technology Administration, National Institute of Standards and Technology, Information Technology Laboratory, Building and Fire Research Labortory.

43. Garboczi, E.J. and A.R. Day, *An algorithm for computing the effective linear elastic properties of heterogeneous materials: Three-dimensional results for composites with equal phase poisson ratios.* Journal of the Mechanics and Physics of Solids, 1995. **43**(9): p. 1349-1362.

44. Bullard, J.W., et al., *Coupling thermodynamics and digital image models to simulate hydration and microstructure development of portland cement pastes.* Journal of Materials Research, 2011. **26**(4): p. 609-622.

45. Lothenbach, B. and F. Winnefeld, *Thermodynamic modelling of the hydration of portland cement.* Cement and Concrete Research, 2006. **36**(2): p. 209-226.

46. Kulik, D.A., *Gibbs energy minimization approach to modeling sorption equilibria at the mineral-water interface: Thermodynamic relations for multi-site-surface complexation.* American Journal of Science, 2002. **302**(3): p. 227-279.

47. Kulik, D.A., *Dual-thermodynamic estimation of stoichiometry and stability of solid solution end members in aqueous–solid solution systems.* Chemical Geology, 2006. **225**(3–4): p. 189-212.

48. Zohdi, T.I., *Homogenization methods and multiscale modeling*, in *Encyclopedia of Computational Mechanics*. 2004, John Wiley & Sons, Ltd.

49. Watt, J.P. and L. Peselnick, *Clarification of the Hashin-Shtrikman bounds on the effective elastic moduli of polycrystals with hexagonal, trigonal, and tetragonal symmetries.* Journal of Applied Physics, 1980. **51**(3): p. 1525 - 1531.

50. Kamali, S., et al., *Influence of hydrate dissolution by water on the young's modulus of cement-based materials*, in *FRAMCOS Conference*. 2003.

51. Bower, A.F., *Applied mechanics of solids*. 2009, Brown University, Providence, Rhode Island, USA CRC Press; 1 edition

52. Zienkiewicz, O.C. and R.L. Taylor, *Finite element method (5th edition) Volume 2 - solid mechanics*. Vol. 2. 2000: Butterworth-Heinemann 2000.

53. Lubliner, J., *Plasticity theory (revised edition)*. 2008, University of California at Berkeley: Pearson Education, Inc.

54. Fung, Y. and P. Tong, *Classical and computational solid mechanics. Volume 1 of advanced series in engineering science*. 2001: World Scientific Publishing Company.

55. Wineman, A.S. and K.R. Rajagopal, *Mechanical response of polymers: an introduction*. 2000: Cambridge University Press.

56. Christensen, R., *Theory of viscoelasticity: an introduction*. 2012: Elsevier.

57. Timnoshenko, S.P. and J.N. Goodier, *Theory of elasticity*. 1970, New York,: McGraw-Hill.

58. Landau, L.D. and E.M. Lifshitz, *Theory of elasticity*. 3rd ed. 1986, Oxford: Pergamon.

59. Jones, C.A. and Z.C. Grasley, *Short-term creep of cement paste during nanoindentation. Cement and Concrete Composites.* Cement and Concrete Composites, 2011. **33**(1): p. 12-18.

60. Haupt, R.K., *Explanation of final report on results of tests for portland cement proficiency samples No.167 and No.168*. 2008, Cement and Concrete Reference Laboratory: Gaithersburg, Maryland.

61. Vichit-Vadakan, W. and G.W. Scherer, *Measuring permeability and stress relaxation of young cement paste by beam bending.* Cement and Concrete Research, 2003. **33**(12): p. 1925-1932.

62. Pane, I. and W. Hansen, *Early age creep and stress relaxation of concrete containing blended cements.* Materials and Structures, 2002. **35**(2): p. 92-96.

63. Thomas, J.J. and H.M. Jennings, *A colloidal interpretation of chemical aging of the C-S-H gel and its effects on the properties of cement paste.* Cement and Concrete Research, 2006. **36**(1): p. 30-38.

64. Jennings, H.M., *Colloid model of C−S−H and implications to the problem of creep and shrinkage.* Materials and Structures, 2004. **37**(1): p. 59-70.

65. Bazant, Z.P. and S. Prasannan, *Solidification theory for concrete creep. I: Formulation.* Journal of Engineering Mechanics, 1989. **115**(8): p. 1691-1703.

66. Bazant, Z.P. and S. Prasannan, *Solidification theory for concrete creep. II: Verification and application.* Journal of Engineering Mechanics, 1989. **115**(8): p. 1704-1725.

67. Li, X., et al., *Computing the time evolution of the apparent viscoelastic/viscoplastic poisson's ratio of hydrating cement paste.* Cement and Concrete Composites, 2015. **56**: p. 121-133.

68. Li, X. and Z. Grasley. *Shrinkage and creep caused by dissolution*. in *ConCreep-10: Mechanics and Physics of Creep, Shrinkage, and Durability of Concrete and Concrete Structures*. 2015. Vienna, Austria.

69. Morland, L.W. and E.H. Lee, *Stress analysis for linear viscoelastic materials with temperature variation.* Transactions of The Society of Rheology (1957-1977), 1960. **4**(1): p. 233-263.

70. Carol, I. and Z.P. Bazant, *Viscoelasticity with aging caused by solidification of nonaging constituent.* Journal of Engineering Mechanics, ASCE, 1993. **119**(11): p. 2252-2269.

71. Bazant, Z.P., et al., *Microprestress–solidification theory for concrete creep: I. Aging and drying effects.* Journal of Engineering Mechanics, ASCE, 1997. **123**(11): p. 1188-1194.

72. Poisson, S.D., *Mémoire sur l'équilibre et le mouvement des corps élastiques.* Mémoires del'Académie Royal des Sciences de l'Institut de France, 1829. **8**: p. 357-571.

73. Poisson, S.D., *Addition au mémoire sur l'équilibre et le mouvement des corps élastiques.* Mémoires del'Académie Royal des Sciences de l'Institut de France, 1829. **8**: p. 623-627.

74. Hilton, H.H., *Comments regarding "viscoelastic properties of an epoxy resin during cure" by D. J. O'Brien, P. T. Mather and S. R. White.* Journal of Composite Materials, 2003. **37**(1): p. 89-94.

75. Lakes, R.S. and A. Wineman, *On poisson's ratio in linearly viscoelastic solids.* Journal of Elasticity, 2006. **85**(1): p. 45-63.

76. Kassem, E., Z. Grasley, and E. Masad, *Viscoelastic poisson's ratio of asphalt mixtures.* International Journal of Geomechanics, 2013. **13**(2): p. 162-169.

77. Read, W.T., *Stress Analysis for Compressible Viscoelastic Materials.* Journal of Applied Physics, 1950. **21**(7): p. 671-674.

78. Bernard, O., F.-J. Ulm, and E. Lemarchand, *A multiscale micromechanics-hydration model for the early-age elastic properties of cement-based materials.* Cement and Concrete Research, 2003. **33**(9): p. 1293-1309.

79. Gopalakrishnan, K.S., A.M. Neville, and A. Ghali, *Creep Poisson's ratio of concrete under multiaxial compression.* American Concrete Institute, 1969. **66**(12): p. 1008-1019.

80. Roberts, A.P. and E.J. Garboczi, *Computation of the linear elastic properties of random porous materials with a wide variety of microstructure.* Proceedings of the Royal Society of London Series a-Mathematical Physical and Engineering Sciences, 2002. **458**(2021): p. 1033-1054.

81. Ferry, J.D., *Viscoelastic properties of polymers*. 1980, United States of America: Wiley; 3 edition

82. Grasley, Z.C., K.R. Rajagopal, and X. Li, *Theoretical basis for apparent viscoelastic and viscoplastic behavior of cementitious materials* in *International US-Poland Workshop on Multiscale Computational Modeling of Cementitious Materials*. 2012: Cracow, Poland.

83. Li, X., et al., *Irreversible desiccation shrinkage of cement paste caused by cement grain dissolution and hydrate precipitation.* Materials and Structures, 2016. **50**(2): p. 104.

84. Hansen, W., *Drying shrinkage mechanisms in Portland cement paste.* Journal of the American Ceramic society, 1987. **70**(5): p. 323-328.

85. Powers, T.C., *Mechanisms of shrinkage and reversible creep of hardened cement paste.* The Structure of Concrete and Its Behaviour under Load, 1965: p. 319-344.

86. Powers, T.C., *The thermodynamics of volume change and creep.* Materials and Structures, 1968. **1**(6): p. 487-507.

87. Feldman, R. and P. Sereda, *A new model for hydrated Portland cement and its practical implications.* Engineering Journal, 1970. **53**(8/9): p. 53-59.

88. Young, J., R. Berger, and A. Bentur, *Shrinkage of Tricalcium silicate pastes: Superposition of several mechanisms.* Il Cemento, 1978. **75**(3): p. 391-398.

89. Feldman, R.F. and P.J. Sereda, *A model for hydrated Portland cement paste as deduced from sorption-length change and mechanical properties.* Materials and Structures, 1968. **1**(6): p. 509-520.

90. Lura, P., O.M. Jensen, and K. van Breugel, *Autogenous shrinkage in high-performance cement paste: An evaluation of basic mechanisms.* Cement and Concrete Research, 2003. **33**(2): p. 223-232.

91. Meyers, B.L. and F.O. Slate, *Creep and creep recovery of plain concrete as influenced by moisture conditions and associated variables.* Magazine of Concrete Research, 1970. **22**(70): p. 37-41.

92. Bažant, Z.P., *Thermodynamics of hindered adsorption and its implications for hardened cement paste and concrete.* Cement and Concrete Research, 1972. **2**(1): p. 1-16.

93. Bentur, A., et al., *Creep and drying shrinkage of calcium silicate pastes III. A hypothesis of irreversible strains.* Cement and Concrete Research, 1979. **9**(1): p. 83-95.

94. Bentur, A., N. Milestone, and J. Young, *Creep and drying shrinkage of calcium silicate pastes II. induced microstructural and chemical changes.* Cement and Concrete Research, 1978. **8**(6): p. 721-732.

95. Helmuth, R.A. and D.H. Turk, *Reversible and irreversible drying shrinkage of hardened portland cement and tricalcium silicate pastes.* Portland Cement Association, Research and Development Laboratories, 1967. **9**(2): p. 8-21.

96. Defay, R., A. Bellemans, and I. Prigogine, *Surface tension and adsorption*. 1966: Longmans London.

97. Grasley, Z.C. and K.R. Rajagopal, *Revisiting total, matric, and osmotic suction in partially saturated geomaterials.* Zeitschrift für angewandte Mathematik und Physik, 2011. **63**(2): p. 373-394.

98. Grasley, Z.C., *Measuring and modeling the time-dependent response of cementitious materials to internal stresses*. 2006, University of Illinois at Urbana-Champaign: Urbana, IL.

99. Jensen, O.M., et al., *Clinker mineral hydration at reduced relative humidities.* Cement and Concrete Research, 1999. **29**(9): p. 1505-1512.

100. Tanabe, T.-a., et al., *Creep, shrinkage and durability mechanics of concrete and concrete structures, two volume set: Proceedings of the concreep 8 conference held in ise-shima, japan, 30 september-2 october 2008*. 2008: CRC Press.

101. Bentz, D.P., E.J. Garboczi, and D.A. Quenard, *Modelling drying shrinkage in reconstructed porous materials: application to porous Vycor glass.* Modelling and Simulation in Materials Science and Engineering, 1998. **6**(3): p. 211.

102. Hajibabaee, A., Z. Grasley, and M.T. Ley, *Mechanisms of dimensional instability caused by differential drying in wet cured cement paste.* Cement and Concrete Research, 2016. **79**: p. 151-158.

103. Pinson, M.B., et al., *Hysteresis from multiscale porosity: Modeling water sorption and shrinkage in cement paste.* Physical Review Applied, 2015. **3**(6): p. 064009.

104. Neville, A.M., *Properties of concrete*. 1995: Pearson Education Ltd.

105. Grasley, Z., et al., *Model of infinitesimal, nonlinear elastic response of concrete subjected to uniaxial compression.* Journal of Engineering Mechanics, 2015. **141**(7): p. 04015008.

106. Galitz, C. and Z. Grasley, *Effects of strain reversal on elastic and viscoelastic properties of early age cement paste beams.* Materials and Structures, 2015: p. 1-13.

107. Pachon-Rodriguez, E.A., et al., *Pressure solution as origin of the humid creep of a mineral material.* Physical Review E, 2011. **84**(6): p. 066121.

108. Green, H., *"Pressure solution" creep: some causes and mechanisms.* Journal of Geophysical Research: Solid Earth, 1984. **89**(B6): p. 4313-4318.

109. Rutter, E. and D. Elliott, *The kinetics of rock deformation by pressure solution [and discussion].* Philosophical Transactions of the Royal Society of London A: Mathematical, Physical and Engineering Sciences, 1976. **283**(1312): p. 203-219.

110. Rutter, E., *Pressure solution in nature, theory and experiment.* Journal of the Geological Society, 1983. **140**(5): p. 725-740.

111. Weyl, P.K., *Pressure solution and the force of crystallization: a phenomenological theory.* Journal of Geophysical Research, 1959. **64**(11): p. 2001-2025.

112. Bons, P.D. and B. den Brok, *Crystallographic preferred orientation development by dissolution–precipitation creep.* Journal of Structural Geology, 2000. **22**(11–12): p. 1713-1722.

113. de Meer, S. and C.J. Spiers, *Uniaxial compaction creep of wet gypsum aggregates.* Journal of Geophysical Research: Solid Earth, 1997. **102**(B1): p. 875-891.

114. Le Guen, Y., et al., *Enhanced deformation of limestone and sandstone in the presence of high pCO2 fluids.* Journal of Geophysical Research : Solid Earth, 2007. **112**: p. B05421.

115. Renard, F., et al., *Simulation numérique de l'effet du stockage souterrain de dioxyde de carbone sur la déformation des calcaires par dissolution sous contrainte : résultats préliminaires.* Oil & Gas Science and Technology - Rev. IFP, 2005. **60**(2): p. 381-399.

116. Niemeijer, A.R., C.J. Spiers, and B. Bos, *Compaction creep of quartz sand at 400-600C: experimental evidence for dissolution-controlled pressure solution.* Earth and Planetary Science Letters, 2002. **195**(3-4): p. 261-75.

117. Shimizu, I., *Kinetics of pressure solution creep in quartz; theoretical considerations.* Tectonophysics, 1995. **245**(3-4): p. 121-134.

118. Condo, P.D., D.R. Paul, and K.P. Johnston, *Glass transitions of polymers with compressed fluid diluents: type II and III behavior.* Macromolecules, 1994. **27**(2): p. 365-371.

119. Mills, N. and A. Gilcrist, *Creep and recovery of polyolefin foams—deformation mechanisms.* Journal of cellular plastics, 1997. **33**(3): p. 264-292.

120. Karato, S.-I. and H. Jung, *Effects of pressure on high-temperature dislocation creep in olivine.* Philosophical Magazine, 2003. **83**(3): p. 401-414.

121. Bresson, B., et al., *Hydration of tricalcium silicate (C3S) at high temperature and high pressure.* Journal of Materials Science. **37**(24): p. 5355-5365.

122. Scherer, G.W., G.P. Funkhouser, and S. Peethamparan, *Effect of pressure on early hydration of class H and white cement.* Cement and Concrete Research, 2010. **40**(6): p. 845-850.

123. Zhou, Q. and J.J. Beaudoin, *Effect of applied hydrostatic stress on the hydration of Portland cement and C3S.* Advances in cement research, 2003. **15**(1): p. 9-16.

124. Rajagopal, K.R. and L. Tao, *Mechanics of mixtures*. Vol. 35. 1995: World scientific.

125. Grasley, Z.C., K.R. Rajagopal, and C.K. Leung, *Equilibrium of partially dried porous media influenced by dissolved species and the development of new interfaces.* International Journal of Engineering Science, 2011. **49**(7): p. 711-725.

126. Hill, T.L., *An introduction to statistical thermodynamics*. 2012: Courier Corporation.

127. Gyftopoulos, E.P. and G.P. Beretta, *Thermodynamics: foundations and applications*. 2005: Courier Corporation.

128. Lasaga, A.C., *Rate laws of chemical reactions.* Rev. Mineral.; (United States), 1981: p. Medium: X; Size: Pages: 1-68.

129. Nielsen, A.E., *Electrolyte crystal growth mechanisms.* Journal of Crystal Growth, 1984. **67**(2): p. 289-310.

130. Li, X., S. Rahman, and Z.C. Grasley, *Computationally implemented modeling of creep of composite materials caused by phase dissolution.* Computational Materials Science, 2016. **125**: p. 61-71.

131. Karpov, I., et al., *Minimization of Gibbs free energy in geochemical systems by convex programming.* Geochemistry International, 2001. **39**(11): p. 1108-1119.

132. Feng, P., C. Miao, and J.W. Bullard, *A model of phase stability, microstructure and properties during leaching of portland cement binders.* Cement and Concrete Composites, 2014. **49**: p. 9-19.